Squeezed light in a refractive index enhancement setup and detection of axions in guided structures

by

Shay Inbar

A dissertation submitted in partial fulfillment of
the requirements for the degree of

Doctor of Philosophy

(Physics)

at the

UNIVERSITY OF WISCONSIN-MADISON

2023

Date of final oral examination: November 9, 2023

The dissertation is approved by the following members of the Final Oral Committee:

Deniz D. Yavuz, Professor, Physics

Mark Saffman, Professor, Physics

Thad G. Walker, Professor, Physics

Micheline B. Soley, Professor, Chemistry

Acknowledgments

First, I would like to thank my advisor, Deniz Yavuz. He came up with many of the original ideas in the projects described here. With his enthusiasm for physics, broad knowledge of the field and patience to answer all of my questions, he had been a tremendous mentor, and I learned a lot from him.

I would like to thank my group peers - Josh Karpel, Zack Buckholtz, Dipto Das, David Gold and Utku Saglam for many helpful discussions, in physics and otherwise, and for the fun meetings at lunch times.

I am grateful for my committee for taking the time and effort to read through my work and bringing their expertise in evaluating it.

A special thanks to the UW Center for High Throughput Computing for helping me set up and run some of those long and resource-hungry simulations and tackling problems.

And finally, I would like to thank my family for all their support and encouragement and especially my wife, Jen; my parents, Malki and Yehuda; and my brother and sister-in-law, Ran and Yael. I would like to thank my mother-in-law, Shauna, for the huge help with the baby while I was working, and for my daughter, Liron, for bringing me joy and giving me the energy to work.

Contents

Abstract

This thesis consists of two separate parts. In the first part, we investigate a system for refractive index enhancement. Such a system is useful for example in imaging science, where a large refractive index reduces the wavelength of light hence improving the achievable resolution. Systems exhibiting electromagnetically induced transparency (EIT) are known to produce such an enhancement. However, the effect is not significant and it changes only the slope of the refractive index as a function of frequency. A system developed in Yavuz lab demonstrated an increase in the refractive index while maintaining zero absorption, controlling the refraction index directly. In this thesis, we make further quantum investigations on this system using numerical simulations, and find that under certain conditions of the system parameters, it exhibits quadrature squeezing or photon-number squeezing. This is remarkable, since traditionally squeezed states are generated by an explicit nonlinearity in the system, while here it is the result of a quantum interference of linear laser-atom interactions in the system.

In the second part of the thesis, we propose a scheme for the detection of axions. The axion is a hypothetical particle originally postulated to solve the strong CP problem in particle physics. It is also a promising candidate to be dark matter, which had been a long-standing problem in physics and cosmology: the evidence for its existence is abundant, yet no direct measurement has confirmed it as of yet, and its nature is unknown. The speculated role of the axion in both these puzzles had motivated experimental searches for it. We propose an experimental scheme for the detection of axions using four-wave mixing in optical fibers. An advantage of this scheme is our control of the operating lasers, which allows for the scanning of a range of axion masses.

Chapter 1

Introduction

Four-wave mixing, the nonlinear process in which two light beams at different frequencies interact through a $\chi^{(3)}$ nonlinearity to produce two new frequencies, has applications in multiple fields, for example: phase conjugation, real-time holographic imaging and photon-pair generation in quantum communication. In Yavuz lab it was used in former projects of the group, including molecular modulation [1] and refractive index enhancement [2]. This thesis consists of two parts connected by the common theme of implementing four-wave mixing at the core of the systems. Another common theme is the use of squeezed light. The first part of the thesis investigates the quantum properties of a system for increasing the index of refraction. This has applications in imaging science: The imaging resolution is limited by the wavelength of light, as we are able to resolve objects which are no smaller than about the wavelength of light. This is known as the diffraction limit, and a way to improve this is to increase the index of refraction of the medium. Such an increase would decrease the wavelength λ to $\sim \lambda/n$ hence improving the resolution. Motivated by this, systems for "engineering" the index of refraction had been investigated for a while. It is known that near an atomic resonance, the index of refraction can be high. However, the accompanied absorption is high as well and the effect is not useful. Setups implementing "Electromagnetically Induced Transparency" (EIT) are capable of achieving increased refractive index with vanishing absorption. EIT is a technique that can render a medium transparent to near-resonant light. The technique relies on quantum interference associated with an established dark-state of an atomic system, which is achieved by dressing the atoms using an intense control laser (also frequently referred as the coupling laser). Over the last two decades it had been used in a wide range of nonlinear and quantum optics effects, including slow-light, stopped light, and enhanced optical nonlinearities that can be effective even at the single photon level. This is another area of active research. Here we focus on the index enhancement property. In order to improve and complement the EIT method, Yavuz lab had developed a system [2][3] for increasing the index of refraction while experiencing zero absorption. Unlike EIT which changes the slope of the index of refraction as a function of frequency, the developed system controls the value of the refraction index directly. Such a system is interesting and the goal of this part of the thesis is to make further quantum investigations and determine the conditions under which squeezed states arise. In my investigations, I used numerical simulations written in Python using the QuTiP package, and found that the system exhibits quadrature squeezing or photon-number squeezing under certain conditions of the system parameters. This is interesting, since quadrature squeezing typically requires explicitly nonlinear Hamiltonian terms. Here, this is the result of a quantum interference between two linear parts of the system, and could have future applications. The simulations were run with the help of the Center for High-Throughput Computing (CHTC) at UW-Madison.

The structure of this part of the thesis is as follows: Chapter 2 develops a theoretical description of squeezed light and the squeezing operator, and reviews experimental progress in the field. Chapter 3 reviews refractive index enhancement setups, including the one which is the basis for our investigations. It reviews the susceptibility behavior near atomic resonance, the refractive index enhancement achieved using EIT setups, and finally the system developed by our lab for refractive index enhancement with zero absorption. Chapter 4 then describes our photon statistics investigation of the index enhancement setup. We provide two analytical analyses: One solving exactly for the quadrature squeezing in terms of the system parameters, but under a specific initial condition and a slow variation assumption, and a second one solving the corresponding

Schrodinger equations, allowing for the calculation of probability amplitudes and photon statistics, iteratively. We then show the results of numerical simulations and their dependence on the system parameters, and find the conditions under which quadrature squeezing or photon-number squeezing arises.

In the second part of the thesis I describe a system for the generation and detection of axions. The axion is a hypothetical particle, motivated to exist in order to solve a known problem in particle physics: the strong CP-problem. Looking at the strong-interaction sector of the Standard Model Lagrangian, there is a term which is not invariant under CP (charge conjugation + parity) transformations. However, experiments indicate such an invariance exists to a high degree. Experiments measuring the contribution of this term to the electric dipole moment, which should be nonzero in the case of CP-violation, found it to be smaller than one part in 10^{15}. A proposed solution was to assume the existence of a field which experiences spontaneous symmetry breaking under some energy scale, acquiring a nonzero quantum expectation value. This nonzero value cancels out that term in the Lagrangian and explains why the symmetry holds. The Goldstone boson associated with the excitations of this field is the axion. The existence of the axion also provides a good candidate for solving another big problem: the nature of dark matter. As a particle interacting very weakly with electromagnetic radiation, it is a natural candidate to be dark matter. This had motivated experimental searches for the axion, which have so far came short of finding it. We propose a system for generating and detecting axions using lasers in optical fibers. This type of a system which both generates and detects axions (as opposed to detecting existing axions from astrophysical sources) belong in a category of experiments known as “light shining through a wall” where photons are converted into axions under the influence of a strong magnetic field, pass through an optical barrier, and reconvert back into photons, which are measured. A great advantage of our scheme is the very large interaction length for the generation and the detection of axions, using kilometers of optical fibers (see the length parameter of phases 1-4 of our setup) which increases the achievable sensitivity. Another important advantage is the control of the laser frequencies producing the axion, allowing for the scanning of different axion masses, as well as flexibility in the central frequencies of the chosen lasers.

The structure of this part of the thesis is as follows: In chapter 5 we describe evidence for the existence of dark matter, and potential particle candidates. The axion makes a good candidate which motivates its existence. In chapter 6 we describe current and planned axion detection experiments, and their corresponding measured and projected sensitivity limits. Then in chapter 7 we describe our axion generation and detection setup: The experimental scheme, examples of possible axion solutions, and a calculation of the coupling constant sensitivity that this experiment would produce, for 4 phases of experimental parameters, taking into account potential noise sources.

Part I

Squeezed light in a refractive index enhancement setup

Chapter 2

Quantization of light and squeezed light

2.1 Quantization of light

In this chapter we review the quantization of light (also typically referred to as second quantization of Maxwell's equations) and also discuss various statistical properties of quantum states of light. In particular, we review coherent states, which have equal amounts of quantum fluctuations in both quadratures, quadrature-squeezed states, and photon-number squeezed states, showing sub-Poissonian statistics. To a large extent we will follow the description by [4]. In order to describe quantized light we consider for simplicity a cavity with conducting walls on both sides. Assuming no electric charges or currents inside, the electromagnetic field in the cavity is described by Maxwell's equations without sources:

$$\nabla \times \mathbf{E} = -\frac{\partial \mathbf{B}}{\partial t} \tag{2.1}$$

$$\nabla \times \mathbf{B} = \mu_0 \varepsilon_0 \frac{\partial \mathbf{E}}{\partial t} \tag{2.2}$$

$$\nabla \cdot \mathbf{E} = 0 \tag{2.3}$$

$$\nabla \cdot \mathbf{B} = 0 \tag{2.4}$$

We consider a sinusoidal standing wave in the cavity. Because of the boundary conditions, the electric field vanishes at both ends of the cavity and would be described by a standing wave that has a sinusoidal dependence on position. Letting the cavity axis to be in the z-direction (the wave propagation direction), and the transverse electric and magnetic fields be in the x- and y-directions, we have

$$E_x = G(t)\sin(kz) \tag{2.5}$$

where $G(t)$ is some function of time and $\sin(kz)$ satisfies the boundary conditions. The quantity k is the magnitude of the optical k-vector, $k = |\vec{k}|$. Given the above expression for the electric field, Maxwell's equations constrain the form of the magnetic field. Using Eq. (2.2) we have

$$\begin{aligned} -\frac{\partial B_y}{\partial z} &= \mu_0\varepsilon_0\,\dot{G}(t)\sin(kz) \\ \because \quad B_y(z,t) &= \frac{\mu_o\varepsilon_0}{k}\,\dot{G}(t)\cos(kz) \end{aligned} \tag{2.6}$$

The total stored energy of the electromagnetic field, integrated over the whole volume of the cavity, is then

$$\begin{aligned} H &= \frac{1}{2}\int dV \left(\varepsilon_0\mathbf{E}^2(\mathbf{r},t) + \frac{1}{\mu_0}\mathbf{B}^2(\mathbf{r},t)\right) \\ &= \frac{1}{2}\int dV \left(\varepsilon_0 E_x^2 + \frac{1}{\mu_0}B_y^2\right) \\ &= \frac{1}{2}\int dV \left[\varepsilon_0 G^2(t)\sin^2(kz) + \frac{\mu_0\varepsilon_0^2}{k^2}\dot{G}^2(t)\cos^2(kz)\right] \end{aligned} \tag{2.7}$$

We now let the cavity length be L. Noticing that $\int_0^L \sin^2(kz)dz = \int_0^L \cos^2(kz)dz = L/2$ where $k = n\pi/L$ gives

$$H = \frac{V}{4}\varepsilon_0\left(G^2(t) + \frac{\dot{G}^2(t)}{\omega^2}\right) \tag{2.8}$$

where we have used $\omega^2/k^2 = c^2 = 1/(\varepsilon_0\mu_0)$. We can write this as

$$H = \frac{V\varepsilon_0}{4\omega^2}\left(\dot{G}^2 + \omega^2 G^2\right) \tag{2.9}$$

which has the form of the Hamiltonian of a harmonic oscillator

$$H = \frac{1}{2}(p^2 + \omega^2 q^2) \tag{2.10}$$

if we identify the canonical coordinates

$$q \equiv \sqrt{\frac{V\varepsilon_0}{2\omega^2}}G \tag{2.11}$$

$$p \equiv \dot{G} \tag{2.12}$$

Now, to quantize this field, we will replace these classical canonical coordinates with corresponding operators. For this purpose, we set the commutator between the position and momentum operators to a non-vanishing value:

$$[\hat{q}, \hat{p}] = i\hbar \tag{2.13}$$

which quantizes phase-space. We next define the following creation and annihilation operators, which are linear superpositions of the canonical coordinates:

$$\hat{a} = \sqrt{\frac{\omega}{2\hbar}}\left(\hat{q} + \frac{i\hat{p}}{\omega}\right) \tag{2.14}$$

$$\hat{a}^\dagger = \sqrt{\frac{\omega}{2\hbar}}\left(\hat{q} - \frac{i\hat{p}}{\omega}\right) \tag{2.15}$$

Using the commutation relation between the position and momentum operators, the commutation relation between the creation and annihilation operators can immediately be shown to be:

$$[\hat{a}, \hat{a}^\dagger] = 1 \tag{2.16}$$

As is the case for any harmonic oscillator, the Hamiltonian for the system can now be expressed as:

$$\hat{H} = \hbar\omega \left(\hat{a}^\dagger \hat{a} + \frac{1}{2} \right) \tag{2.17}$$

which leads to quantized energy levels. If we define the number operator, $\hat{n} = \hat{a}^\dagger \hat{a}$, we have

$$\hat{H} |n\rangle = \hbar\omega \left(\hat{n} + \frac{1}{2} \right) |n\rangle = \hbar\omega \left(n + \frac{1}{2} \right) \equiv E_n |n\rangle \tag{2.18}$$

which is the energy of an n-photon Fock state. Now, to find the full spectrum of energy eigenvalues, we apply:

$$\hat{n}(\hat{a}^\dagger |n\rangle) = \hat{a}^\dagger \hat{a} \hat{a}^\dagger |n\rangle = \hat{a}^\dagger (\hat{a}^\dagger \hat{a} + 1) |n\rangle = (\hat{a}^\dagger \hat{n} + \hat{a}^\dagger) |n\rangle = (n+1) \hat{a}^\dagger |n\rangle \tag{2.19}$$

which then gives

$$\begin{aligned} \hat{H}(\hat{a}^\dagger |n\rangle) &= \hbar\omega \left(\hat{n} + \frac{1}{2} \right) (\hat{a}^\dagger |n\rangle) = \hbar\omega \left[(n+1) + \frac{1}{2} \right] (\hat{a}^\dagger |n\rangle) \\ &= \left[\hbar\omega \left(n + \frac{1}{2} \right) + \hbar\omega \right] (\hat{a}^\dagger |n\rangle) = (E_n + \hbar\omega)(\hat{a}^\dagger |n\rangle) \end{aligned} \tag{2.20}$$

and so we see that $\hat{a}^\dagger |n\rangle$ is a state with energy $E_n + \hbar\omega$, consisting of $n+1$ photons. Therefore we can write

$$\hat{a}^\dagger |n\rangle = B_n |n+1\rangle \tag{2.21}$$

where B_n is a constant to be determined using the normalization condition of eigenstates. Similarly we can show that $\hat{a} |n\rangle$ is a state with energy $E_n - \hbar\omega$ consisting of $n-1$ photons.

We can therefore write

$$\hat{a}\,|n\rangle = C_n\,|n-1\rangle \tag{2.22}$$

To find the constants, B_n and C_n, we note that

$$\begin{aligned}\langle n|\,\hat{a}^\dagger\hat{a}\,|n\rangle &= \langle n|\,\hat{n}\,|n\rangle = n\\ &= \langle n-1|\,C_n^* C_n\,|n-1\rangle = |C_n|^2\end{aligned} \tag{2.23}$$

therefore we can choose $C_n = \sqrt{n}$ and

$$\hat{a}\,|n\rangle = \sqrt{n}\,|n-1\rangle \tag{2.24}$$

similarly

$$\begin{aligned}\langle n|\,\hat{a}\hat{a}^\dagger\,|n\rangle = \langle n|\,(\hat{a}^\dagger\hat{a}+1)\,|n\rangle &= \langle n|\,\hat{n}+1\,|n\rangle = n+1\\ &= \langle n+1|\,B_n^* B_n\,|n+1\rangle = |B_n|^2\end{aligned} \tag{2.25}$$

and we can choose $B_n = \sqrt{n+1} = C_{n+1}$. Since the energy of the harmonic oscillator must be positive the ladder at the bottom has to stop at a finite state, call it $|0\rangle$. So we must have $\hat{a}\,|0\rangle = 0$. This ground state has zero photons $n = 0$ and has the well-known energy of vacuum which equals half quanta, i.e., $E_0 = \hbar\omega/2$.

2.2 Quadrature operators

Using the expressions for the creation and annihilation operators of eqs. (2.14), (2.15) we can write

$$\hat{q}(t) = \sqrt{\frac{\hbar}{2\omega}}\left(\hat{a}(t) + \hat{a}^\dagger(t)\right) \tag{2.26}$$

then from Eqs. (2.5), (2.11) , (2.26) we get

$$\hat{E}(z,t) = E_0 \left(\hat{a}(t) + \hat{a}^\dagger(t)\right) \sin(kz) \tag{2.27}$$

where the quantity $E_0 = \sqrt{\frac{\hbar\omega}{V\varepsilon_0}}$ is the electric field amplitude corresponding to a single photon in the cavity mode. We note that using the Hamiltonian of the system, we can write the Heisenberg equation of motion to calculate the time evolution of any operator. Specifically, to calculate the time evolution of the annihilation operator $\hat{a}(t)$, we use:

$$\begin{aligned}
\frac{d\hat{a}(t)}{dt} &= \frac{i}{\hbar}[\hat{H}, \hat{a}] = \frac{i}{\hbar}\left[\hbar\omega\left(\hat{a}^\dagger\hat{a} + \frac{1}{2}\right), \hat{a}\right] \\
&= i\omega[\hat{a}^\dagger\hat{a}, \hat{a}] \\
&= i\omega(\hat{a}^\dagger\hat{a}\hat{a} - \hat{a}\hat{a}^\dagger\hat{a}) \\
&= -i\omega(\hat{a}\hat{a}^\dagger - \hat{a}^\dagger\hat{a})\hat{a} \\
&= -i\omega[\hat{a}, \hat{a}^\dagger]\hat{a} \\
&= -i\omega\hat{a}(t)
\end{aligned} \tag{2.28}$$

where we used Eq. (2.16) in the last line. The differential equation for the time evolution of the annihilation operator of above then implies:

$$\hat{a}(t) = \hat{a}\exp(-i\omega t) \tag{2.29}$$

and therefore

$$\hat{a}^\dagger(t) = \hat{a}^\dagger \exp(i\omega t) \tag{2.30}$$

where $\hat{a} \equiv \hat{a}(0)$ and $\hat{a}^\dagger \equiv \hat{a}^\dagger(0)$. We can then write the electric field as

$$\hat{E}_x(z,t) = E_0 \left(\hat{a}\exp(-i\omega t) + \hat{a}^\dagger \exp(i\omega t)\right) \sin(kz) \tag{2.31}$$

Note that in the above equation, we express the electric field as a superposition of creation and annihilation operators, each multiplying a complex exponential, $\exp(-i\omega t)$ and $\exp(i\omega t)$, respectively. The main idea behind the quadrature operators is that the above superposition for the electric field can instead be written as a sum of two time-domain functions, a sine and a cosine. For this purpose, we define the following two operators (the quadratures):

$$\begin{aligned} \hat{X}_1 &= (\hat{a}^\dagger + \hat{a}) \\ \hat{X}_2 &= i(\hat{a}^\dagger - \hat{a}) \end{aligned} \tag{2.32}$$

Using the above definitions, we can express the electric field as the following superposition:

$$\hat{E}_x(t) = E_0 \sin(kz) \left[\hat{X}_1 \cos(\omega t) + \hat{X}_2 \sin(\omega t) \right] \tag{2.33}$$

The quantities $\hat{X}_1$ and $\hat{X}_2$ represent two field components oscillating in time at a phase difference of $\pi/2$ and are hence called the field quadratures. They play the same role of position and momentum in phase space, but are dimensionless. Using $[\hat{a}, \hat{a}^\dagger] = 1$, we have the following commutation relation between the quadrature operators:

$$[\hat{X}_1, \hat{X}_2] = 2i \tag{2.34}$$

then using the uncertainty relation

$$\Delta\hat{A}\,\Delta\hat{B} \geq \frac{1}{2} \left| \langle [\hat{A}, \hat{B}] \rangle \right| \tag{2.35}$$

we can derive the following inequality for the product of the variances (the fluctuations) of the uncertainty operators.

$$\Delta\hat{X}_1\,\Delta\hat{X}_2 \geq 1 \tag{2.36}$$

Let us now calculate the variances $\Delta\hat{X}_1$, $\Delta\hat{X}_2$ for the photon-number eigenstates. We have

$$\begin{aligned} \langle n|\hat{X}_1|n\rangle &= \langle n|(\hat{a}+\hat{a}^\dagger)|n\rangle = 0 \\ \langle n|\hat{X}_2|n\rangle &= i\,\langle n|(\hat{a}^\dagger-\hat{a})|n\rangle = 0 \end{aligned} \tag{2.37}$$

and

$$\begin{aligned} \langle n|\hat{X}_1^2|n\rangle &= \langle n|(\hat{a}^2+\hat{a}^{\dagger 2}+\hat{a}^\dagger\hat{a}+\hat{a}\hat{a}^\dagger)|n\rangle \\ &= (0+0+n+(n+1)) \\ &= 2n+1 \end{aligned} \tag{2.38}$$

and similarly $\langle n|\hat{X}_2^2|n\rangle = 2n+1$. Therefore

$$\begin{aligned} \langle(\Delta\hat{X}_1)^2\rangle &= \langle\hat{X}_1^2\rangle - \langle\hat{X}_1\rangle^2 = 2n+1 \\ \langle(\Delta\hat{X}_2)^2\rangle &= \langle\hat{X}_2^2\rangle - \langle\hat{X}_2\rangle^2 = 2n+1 \end{aligned} \tag{2.39}$$

specifically for the vacuum state $n=0$ we get

$$\langle(\Delta\hat{X}_1)^2\rangle_{\text{vac}} = \langle(\Delta\hat{X}_2)^2\rangle_{\text{vac}} = 1 \tag{2.40}$$

This is the case where both quadratures have the same uncertainty and their uncertainty relation has the minimum value:

$$\langle\Delta\hat{X}_1\rangle_{\text{vac}} = \langle\Delta\hat{X}_2\rangle_{\text{vac}} = 1 \tag{2.41}$$

so $\hat{X}_1$ and $\hat{X}_2$ describe a circle in phase space for the vacuum state.

2.3 Coherent states

We can define a coherent state of parameter α (a complex number) as being an eigenstate of the annihilation operator:

$$\hat{a}\,|\alpha\rangle = \alpha\,|\alpha\rangle \tag{2.42}$$

Coherent states have a close analogy with classical field states of definite amplitude since from the expression above, interactions with another system that cause absorption of photons ($\hat{a}$ operator) leave the field in a coherent state. For this reason it is called the "most classical" state. Let's calculate the uncertainty of the quadratures associated with a coherent state.

$$\begin{aligned}\langle\alpha|\hat{X}_1|\alpha\rangle &= \langle\alpha|(\hat{a}+\hat{a}^\dagger)|\alpha\rangle \\ &= \langle\alpha|\hat{a}|\alpha\rangle + \langle\alpha|\hat{a}^\dagger|\alpha\rangle \\ &= \alpha+\alpha^*\end{aligned} \tag{2.43}$$

and

$$\begin{aligned}\langle\alpha|\hat{X}_1^2|\alpha\rangle &= \langle\alpha|(\hat{a}^2+\hat{a}^{\dagger 2}+\hat{a}^\dagger\hat{a}+\hat{a}\hat{a}^\dagger)|\alpha\rangle \\ &= \langle\alpha|(\hat{a}^2+\hat{a}^{\dagger 2}+2\hat{a}^\dagger\hat{a}+1)|\alpha\rangle \\ &= \alpha^2+\alpha^{*2}+2|\alpha|^2+1 \\ &= (\alpha+\alpha^*)^2+1\end{aligned} \tag{2.44}$$

then the uncertainty is:

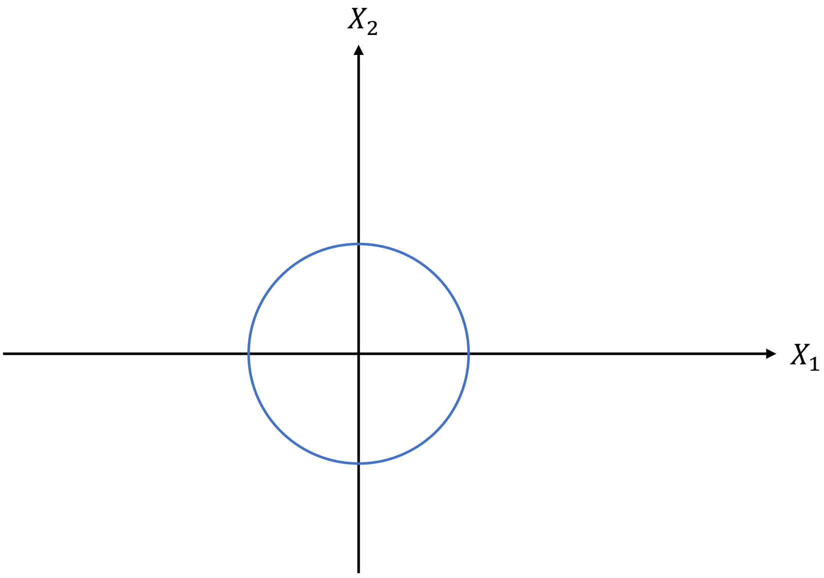

Figure 2.1: Phase space of a coherent state with parameter $\alpha = 0$, or a vacuum state.

$$\begin{aligned}\langle(\Delta\hat{X}_1)^2\rangle_{\text{coherent}} &= \langle\alpha|\hat{X}_1^2|\alpha\rangle - \langle\alpha|\hat{X}_1|\alpha\rangle^2 \\ &= (\alpha+\alpha^*)^2 + 1 - (\alpha+\alpha^*)^2 \\ &= 1\end{aligned} \tag{2.45}$$

We can similarly show that $\langle(\Delta\hat{X}_2)^2\rangle_{\text{coherent}} = 1$. Therefore it is evident that coherent states are minimum uncertainty states with equal uncertainty in both quadratures, which describes a circle in phase space (just like the vacuum state), see Figure 2.1.

For many calculations, it is useful to express the coherent state in the basis of photon-number eigenstates. Since photon-number eigenstates form a complete basis set, we can write any coherent state $|\alpha\rangle$ as the following superposition:

$$|\alpha\rangle = \sum_{n=0}^{\infty} C_n |n\rangle \tag{2.46}$$

Using the above superposition, the eigenvalue equation for the annihilation operator can be expressed as:

$$\begin{aligned}
\hat{a}\,|\alpha\rangle &= \alpha\,|\alpha\rangle \\
\hat{a}\sum_{n=0}^{\infty} C_n\,|n\rangle &= \alpha\sum_{n=0}^{\infty} C_n\,|n\rangle \\
\sum_{n=1}^{\infty} C_n\sqrt{n}\,|n-1\rangle &= \sum_{n=1}^{\infty}\alpha\,C_{n-1}\,|n-1\rangle
\end{aligned} \tag{2.47}$$

We can then equate the coefficients of $|n-1\rangle$ in the above two summations, which gives:

$$C_n\sqrt{n} = \alpha\,C_{n-1} \tag{2.48}$$

or

$$C_n = \frac{\alpha}{\sqrt{n}}C_{n-1} = \frac{\alpha^2}{\sqrt{n(n-1)}}C_{n-2} = \ldots = \frac{\alpha^n}{\sqrt{n!}}C_0 \tag{2.49}$$

so we have

$$|\alpha\rangle = C_0\sum_{n=0}^{\infty}\frac{\alpha^n}{\sqrt{n!}}\,|n\rangle \tag{2.50}$$

C_0 can be found from normalization:

$$\begin{aligned}
\langle\alpha|\alpha\rangle &= |C_0|^2\sum_{n=0}^{\infty}\sum_{n'=0}^{\infty}\frac{\alpha^{*n}\alpha^{n'}}{\sqrt{n!n'!}}\,\langle n|n'\rangle \\
&= |C_0|^2\sum_{n=0}^{\infty}\frac{|\alpha|^{2n}}{n!} \\
&= |C_0|^2\exp(|\alpha|^2) \equiv 1
\end{aligned} \tag{2.51}$$

from this

$$C_0 = \exp\left(-\frac{1}{2}|\alpha|^2\right) \tag{2.52}$$

and therefore the normalized coherent state is

$$|\alpha\rangle = \exp\left(-\frac{1}{2}|\alpha|^2\right)\sum_{n=0}^{\infty}\frac{\alpha^n}{\sqrt{n!}}|n\rangle \tag{2.53}$$

2.4 The displacement operator

The fact that both the vacuum state and the coherent state are described by a circle of minimum uncertainty in phase space suggests that there is a displacement operator that can map the vacuum state into a coherent state of a given parameter α by "displacing" the circle in phase space (see Figure 2.2). We derive the expression for such an operator below. Writing the number state as photon excitations of the vacuum:

$$|n\rangle = \frac{(\hat{a}^\dagger)^n}{\sqrt{n!}}|0\rangle \tag{2.54}$$

we can write the coherent state $|\alpha\rangle$ as

$$\begin{aligned}|\alpha\rangle &= \exp\left(-\frac{1}{2}|\alpha|^2\right)\sum_{n=0}^{\infty}\frac{\alpha^n}{\sqrt{n!}}\frac{(\hat{a}^\dagger)^n}{\sqrt{n!}}|0\rangle \\ &= \exp\left(-\frac{1}{2}|\alpha|^2\right)\sum_{n=0}^{\infty}\frac{(\alpha\hat{a}^\dagger)^n}{n!}|0\rangle \\ &= \exp\left(-\frac{1}{2}|\alpha|^2\right)\exp\left(\alpha\hat{a}^\dagger\right)|0\rangle\end{aligned} \tag{2.55}$$

We note that since $\exp(-\alpha^*\hat{a})|0\rangle = |0\rangle$ we can write the coherent state as

$$|\alpha\rangle = \exp\left(-\frac{1}{2}|\alpha|^2\right)\exp\left(\alpha\hat{a}^\dagger\right)\exp(-\alpha^*\hat{a})|0\rangle \tag{2.56}$$

then applying the Campbell-Baker-Hausdorff formula

$$\exp(\hat{A}+\hat{B}) = \exp(\hat{A})\exp(\hat{B})\exp\left(-\frac{1}{2}[\hat{A},\hat{B}]\right) \tag{2.57}$$

with $\hat{A} = \alpha\hat{a}^\dagger$ and $\hat{B} = -\alpha^*\hat{a}$ we get

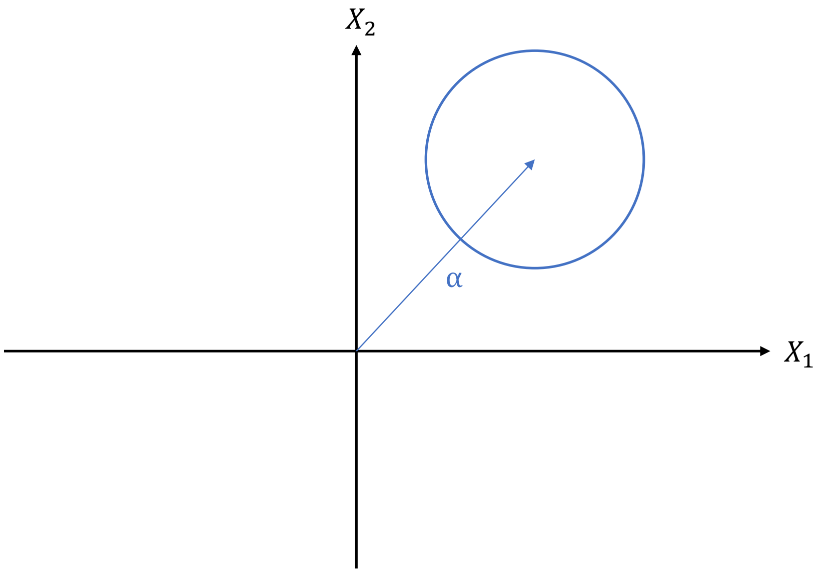

Figure 2.2: Coherent state of parameter α is described as a circle in phase space which is displaced by α from the origin.

$$|\alpha\rangle = \exp(\alpha\hat{a}^{\dagger} - \alpha^{*}\hat{a})\,|0\rangle \equiv \hat{D}(\alpha)\,|0\rangle \tag{2.58}$$

the operator $\hat{D}(\alpha) = \exp(\alpha\hat{a}^{\dagger} - \alpha^{*}\hat{a})\,|0\rangle$ is the *displacement operator*.

2.5 Quadrature squeezing

Quadrature squeezing is described as a state where a quadrature (can also have a general phase angle θ, not necessarily parallel to our $\hat{X}_1$ or $\hat{X}_2$ directions) has a smaller uncertainty $\langle(\Delta\hat{X})^2\rangle$ than that of a coherent state (of course, by the uncertainty relation, the other quadrature would have a bigger uncertainty than the coherent state). As we shall see below, a squeezing operator which can achieve such quadrature squeezing is defined by

$$\hat{S}(\xi) = \exp\left[\frac{1}{2}(\xi^{*}\hat{a}^{2} - \xi\hat{a}^{\dagger 2})\right] \tag{2.59}$$

where $\xi = re^{i\theta}$ is a complex parameter, r represents the amount of squeezing, and θ is the angle of the squeezed quadrature relative to $\hat{X}_1$. Consider the state resulting from the action of the squeezing operator:

$$|\psi_s\rangle = \hat{S}(\xi)\,|\psi\rangle \tag{2.60}$$

We want to evaluate the variance of the quadratures for this state. To do so, we shall first evaluate the expectation values of $\hat{a}$ and $\hat{a}^\dagger$ operators. We have

$$\langle\psi_s|\hat{a}|\psi_s\rangle = \langle\psi|\hat{S}^\dagger(\xi)\hat{a}\hat{S}(\xi)|\psi\rangle \tag{2.61}$$

Let us consider the transformation $\hat{S}^\dagger(\xi)\hat{a}\hat{S}(\xi)$. Using the identity

$$\exp(\lambda\hat{A})\cdot\hat{B}\cdot\exp(-\lambda\hat{A}) = \hat{B} + \frac{\lambda}{1!}[\hat{A},\hat{B}] + \frac{\lambda^2}{2!}[\hat{A},[\hat{A},\hat{B}]] + \ldots \tag{2.62}$$

with $\hat{A} \equiv -(\xi^*\hat{a}^2 - \xi\hat{a}^{\dagger 2})/2$, $\hat{B} \equiv \hat{a}$ and $\lambda \equiv 1$ we have

$$\hat{S}^\dagger(\xi)\hat{a}\hat{S}(\xi) = \exp(\hat{A})\cdot\hat{a}\cdot\exp(-\hat{A}) = \hat{a} + [\hat{A},\hat{a}] + \frac{1}{2!}[\hat{A},[\hat{A},\hat{a}]] + \ldots \tag{2.63}$$

using the relations

$$\begin{aligned} [\hat{a},(\hat{a}^\dagger)^n] &= n(\hat{a}^\dagger)^{n-1} \\ [\hat{a}^n,\hat{a}^\dagger] &= n\hat{a}^{n-1} \end{aligned} \tag{2.64}$$

we get

$$\begin{aligned} [\hat{A},\hat{a}] &= [-\frac{1}{2}\xi^*\hat{a}^2 + \frac{1}{2}\xi\hat{a}^{\dagger 2},\hat{a}] = -\xi\hat{a}^\dagger \\ [\hat{A},\hat{a}^\dagger] &= [-\frac{1}{2}\xi^*\hat{a}^2 + \frac{1}{2}\xi\hat{a}^{\dagger 2},\hat{a}] = -\xi^*\hat{a} \end{aligned} \tag{2.65}$$

and therefore

$$\begin{aligned}
\hat{S}^{\dagger}(\xi)\hat{a}\hat{S}(\xi) &= \hat{a} - \xi\hat{a}^{\dagger} + \frac{1}{2!}|\xi|^2\hat{a} - \frac{1}{3!}\xi|\xi|^2\hat{a}^{\dagger} + \frac{1}{4!}|\xi|^4\hat{a} - \frac{1}{5!}\xi|\xi|^4\hat{a}^{\dagger} + \dots \\
&= \hat{a}\left(1 + \frac{1}{2!}|\xi|^2 + \frac{1}{4!}|\xi|^4 + \dots\right) - \hat{a}^{\dagger}\left(\xi + \frac{1}{3!}\xi|\xi|^2 + \frac{1}{5!}\xi|\xi|^4 + \dots\right) \\
&= \hat{a}\left(1 + \frac{1}{2!}r^2 + \frac{1}{4!}r^4 + \dots\right) - \hat{a}^{\dagger}e^{i\theta}\left(r + \frac{1}{3!}r^3 + \frac{1}{5!}r^5 + \dots\right) \\
&= \hat{a}\cosh(r) - \hat{a}^{\dagger}e^{i\theta}\sinh(r)
\end{aligned} \tag{2.66}$$

in a similar manner

$$\hat{S}^{\dagger}(\xi)\hat{a}^{\dagger}\hat{S}(\xi) = \hat{a}^{\dagger}\cosh(r) - \hat{a}e^{-i\theta}\sinh(r) \tag{2.67}$$

Now let's calculate the variance of the quadratures under the vacuum squeezed state $|\psi_{\mathrm{s}}\rangle \equiv \hat{S}(\xi)|0\rangle$. To do so, we first evaluate

$$\begin{aligned}
\langle\psi_{\mathrm{s}}|\hat{a}|\psi_{\mathrm{s}}\rangle &= \langle 0|\hat{S}^{\dagger}(\xi)\hat{a}\hat{S}(\xi)|0\rangle = \langle 0|\left(\hat{a}\cosh(r) - \hat{a}^{\dagger}e^{i\theta}\sinh(r)\right)|0\rangle = 0 \\
\langle\psi_{\mathrm{s}}|\hat{a}^{\dagger}|\psi_{\mathrm{s}}\rangle &= \langle 0|\hat{S}^{\dagger}(\xi)\hat{a}^{\dagger}\hat{S}(\xi)|0\rangle = \langle 0|\left(\hat{a}^{\dagger}\cosh(r) - \hat{a}e^{-i\theta}\sinh(r)\right)|0\rangle = 0
\end{aligned} \tag{2.68}$$

and

$$\begin{aligned}
\langle\psi_{\mathrm{s}}|\hat{a}^2|\psi_{\mathrm{s}}\rangle &= \langle 0|\hat{S}^{\dagger}(\xi)\hat{a}^2\hat{S}(\xi)|0\rangle \\
&= \langle 0|\hat{S}^{\dagger}(\xi)\hat{a}\hat{S}(\xi)\hat{S}^{\dagger}(\xi)\hat{a}\hat{S}(\xi)|0\rangle \\
&\langle 0|\left(\hat{a}\cosh(r) - \hat{a}^{\dagger}e^{i\theta}\sinh(r)\right)^2|0\rangle \\
&= \langle 0|\hat{a}^2\cosh^2(r) + \hat{a}^{\dagger 2}e^{2i\theta}\sinh^2(r) - (\hat{a}\hat{a}^{\dagger} + \hat{a}^{\dagger}\hat{a})e^{i\theta}\sinh(r)\cosh(r)|0\rangle \\
&= -e^{i\theta}\sinh(r)\cosh(r)
\end{aligned} \tag{2.69}$$

where I used the fact that the squeezing operator is unitary, i.e., $\hat{S}(\xi)\hat{S}^{\dagger}(\xi) = \hat{S}(\xi)\hat{S}^{-1}(\xi) = I$. Similarly,

$$
\begin{aligned}
\langle\psi_{\rm s}|\hat{a}^{\dagger 2}|\psi_{\rm s}\rangle &= \langle 0|\hat{S}^\dagger(\xi)\hat{a}^\dagger\hat{S}(\xi)\hat{S}^\dagger(\xi)\hat{a}^\dagger\hat{S}(\xi)|0\rangle \\
&= \langle 0|\left(\hat{a}^\dagger\cosh(r) - \hat{a}e^{-i\theta}\sinh(r)\right)^2|0\rangle \\
&= \langle 0|\hat{a}^{\dagger 2}\cosh^2(r) + \hat{a}^2e^{-2i\theta}\sinh^2(r) - (\hat{a}\hat{a}^\dagger + \hat{a}^\dagger\hat{a})e^{-i\theta}\sinh(r)\cosh(r)|0\rangle \\
&= -e^{-i\theta}\sinh(r)\cosh(r)
\end{aligned}
\tag{2.70}
$$

also

$$
\begin{aligned}
\langle\psi_{\rm s}|\hat{a}^\dagger\hat{a}|\psi_{\rm s}\rangle &= \langle 0|\hat{S}^\dagger(\xi)\hat{a}^\dagger\hat{S}(\xi)\hat{S}^\dagger(\xi)\hat{a}\hat{S}(\xi)|0\rangle \\
&= \langle 0|\left(\hat{a}^\dagger\cosh(r) - \hat{a}e^{-i\theta}\sinh(r)\right)\left(\hat{a}\cosh(r) - \hat{a}^\dagger e^{i\theta}\sinh(r)\right)|0\rangle \\
&= \langle 0|\,\hat{a}^\dagger\hat{a}\cosh^2(r) - \hat{a}^{\dagger 2}e^{i\theta}\sinh(r)\cosh(r) \\
&- \hat{a}^2e^{-i\theta}\sinh(r)\cosh(r) + \hat{a}\hat{a}^\dagger\sinh^2(r)\,|0\rangle \\
&= \sinh^2(r)
\end{aligned}
\tag{2.71}
$$

and

$$
\begin{aligned}
\langle\psi_{\rm s}|\hat{a}\hat{a}^\dagger|\psi_{\rm s}\rangle &= \langle 0|\hat{S}^\dagger(\xi)\hat{a}\hat{S}(\xi)\hat{S}^\dagger(\xi)\hat{a}^\dagger\hat{S}(\xi)|0\rangle \\
&= \langle 0|\left(\hat{a}\cosh(r) - \hat{a}^\dagger e^{i\theta}\sinh(r)\right)\left(\hat{a}^\dagger\cosh(r) - \hat{a}e^{-i\theta}\sinh(r)\right)|0\rangle \\
&= \langle 0|\,\hat{a}\hat{a}^\dagger\cosh^2(r) - \hat{a}^2e^{-i\theta}\cosh(r)\sinh(r) \\
&- \hat{a}^{\dagger 2}e^{i\theta}\sinh(r)\cosh(r) + \hat{a}^\dagger\hat{a}\sinh^2(r)\,|0\rangle \\
&= \cosh^2(r)
\end{aligned}
\tag{2.72}
$$

Using the expression we have derived above, we get

$$
\begin{aligned}
\langle \hat{X}_1 \rangle &= \langle \psi_{\mathrm{s}} | \hat{X}_1 | \psi_{\mathrm{s}} \rangle = \langle \psi_{\mathrm{s}} | (\hat{a} + \hat{a}^\dagger) | \psi_{\mathrm{s}} \rangle = 0 \\
\langle \hat{X}_2 \rangle &= \langle \psi_{\mathrm{s}} | \hat{X}_2 | \psi_{\mathrm{s}} \rangle = i \, \langle \psi_{\mathrm{s}} | (\hat{a}^\dagger - \hat{a}) | \psi_{\mathrm{s}} \rangle = 0
\end{aligned}
\tag{2.73}
$$

and

$$
\begin{aligned}
\langle \hat{X}_1^2 \rangle &= \langle \psi_{\mathrm{s}} | \hat{X}_1^2 | \psi_{\mathrm{s}} \rangle \\
&= \langle \psi_{\mathrm{s}} | \left(\hat{a}^{\dagger 2} + \hat{a}^\dagger \hat{a} + \hat{a} \hat{a}^\dagger + \hat{a}^2 \right) | \psi_{\mathrm{s}} \rangle \\
&= \cosh^2(r) + \sinh^2(r) - 2 \sinh(r) \cosh(r) \cos(\theta)
\end{aligned}
\tag{2.74}
$$

and

$$
\begin{aligned}
\langle \hat{X}_2^2 \rangle &= \langle \psi_{\mathrm{s}} | \hat{X}_2^2 | \psi_{\mathrm{s}} \rangle \\
&= - \langle \psi_{\mathrm{s}} | \left(\hat{a}^{\dagger 2} - \hat{a}^\dagger \hat{a} - \hat{a} \hat{a}^\dagger + \hat{a}^2 \right) | \psi_{\mathrm{s}} \rangle \\
&= \cosh^2(r) + \sinh^2(r) + 2 \sinh(r) \cosh(r) \cos(\theta)
\end{aligned}
\tag{2.75}
$$

therefore, using the definitions

$$
\begin{aligned}
\langle (\Delta \hat{X}_1)^2 \rangle &= \langle \hat{X}_1^2 \rangle - \langle \hat{X}_1 \rangle^2 \\
\langle (\Delta \hat{X}_2)^2 \rangle &= \langle \hat{X}_2^2 \rangle - \langle \hat{X}_2 \rangle^2
\end{aligned}
\tag{2.76}
$$

we get

$$
\begin{aligned}
\langle (\Delta \hat{X}_1)^2 \rangle &= \cosh^2(r) + \sinh^2(r) - 2 \sinh(r) \cosh(r) \cos(\theta) \\
\langle (\Delta \hat{X}_2)^2 \rangle &= \cosh^2(r) + \sinh^2(r) + 2 \sinh(r) \cosh(r) \cos(\theta)
\end{aligned}
\tag{2.77}
$$

The above expressions correspond to quadrature squeezing when the squeezed quadrature is at an angle θ relative to the $\hat{X}_1$ axis in phase space. For the special case where

$\theta = 0$, these expressions simplify considerably and we get:

$$\begin{aligned}\langle(\Delta\hat{X}_1)^2\rangle &= e^{-2r} \\ \langle(\Delta\hat{X}_2)^2\rangle &= e^{2r}\end{aligned} \tag{2.78}$$

The amount of squeezing is controlled by the parameter r. θ controls the angle of the squeezed quadrature. Setting $\theta = \pi$, we would get

$$\begin{aligned}\langle(\Delta\hat{X}_1)^2\rangle &= e^{2r} \\ \langle(\Delta\hat{X}_2)^2\rangle &= e^{-2r}\end{aligned} \tag{2.79}$$

For an arbitrary angle θ, it is convenient to make a coordinate transformation such that one quadrature is along the squeezed direction and the other is perpendicular to it. Using the following transformation:

$$\hat{Y}_1 + i\hat{Y}_2 = (\hat{X}_1 + i\hat{X}_2)e^{-i\theta/2} \tag{2.80}$$

the squeezed quadrature will be $\hat{Y}_1$ (see Figure 2.3) and we would have

$$\begin{aligned}\langle(\Delta\hat{Y}_1)^2\rangle &= e^{-2r} \\ \langle(\Delta\hat{Y}_2)^2\rangle &= e^{2r}\end{aligned} \tag{2.81}$$

Finally, note that we considered the squeezed vacuum state (i.e., the state obtained by applying the squeezing operator to the vacuum state). As we have seen in Eq. (2.58), the displacement operator creates a coherent state from a vacuum state by shifting the uncertainty circle from the origin to a distance α in phase space, where α is the coherent state parameter. In the same manner, acting on a squeezed state by the displacement operator, or alternatively acting on the vacuum state by the displacement operator and then acting with the squeezing operator, creates the squeezed coherent state $|\alpha, \xi\rangle =$

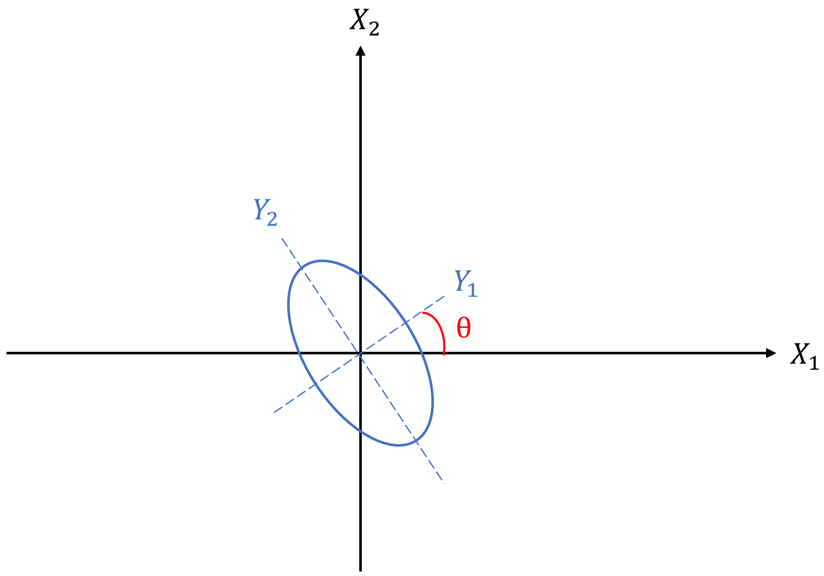

Figure 2.3: Phase space of a quadrature squeezed vacuum state along an axis Y_1. This axis creates an angle θ relative to the X_1 axis.

$\hat{D}(\alpha)\hat{S}(\xi)|0\rangle$, squeezed by the parameter $\xi = re^{i\theta}$ and shifted by α from the origin, with the same squeezing expressions as in Eq. (2.81) along the squeezing axis $\hat{Y}_1$ and the axis perpendicular to it $\hat{Y}_2$ (see Figure 2.4). Finally note that this description using the squeezing operator holds for any squeezed state of *minimum uncertainty*, as can be seen from the fact that

$$\langle(\Delta\hat{Y}_1)^2\rangle\,\langle(\Delta\hat{Y}_2)^2\rangle = 1 \tag{2.82}$$

which is the minimum value of the uncertainty product. In general, if the quadrature $\hat{Y}_1$ is squeezed, the variance in $\hat{Y}_2$ will be large, with the uncertainity product larger than the minimum uncertainty value. We also note that all squeezed states achieved by the application of the squeezing operator are Gaussian. Non-Gaussian states are also possible to achieve by the superpositions of number states [5]. For example, a non-Gaussian state which is the superposition of a vacuum state and a single photon state: $|\Phi\rangle = a|0\rangle + b|1\rangle$. In this thesis I will often quote experimental results or simulations results of quadrature squeezing in dB. In quoting simulation results, the two quadratures are named $\hat{Q}$ and $\hat{P}$. The definition used for squeezing of a quadrature e.g. $\hat{Q}$ is

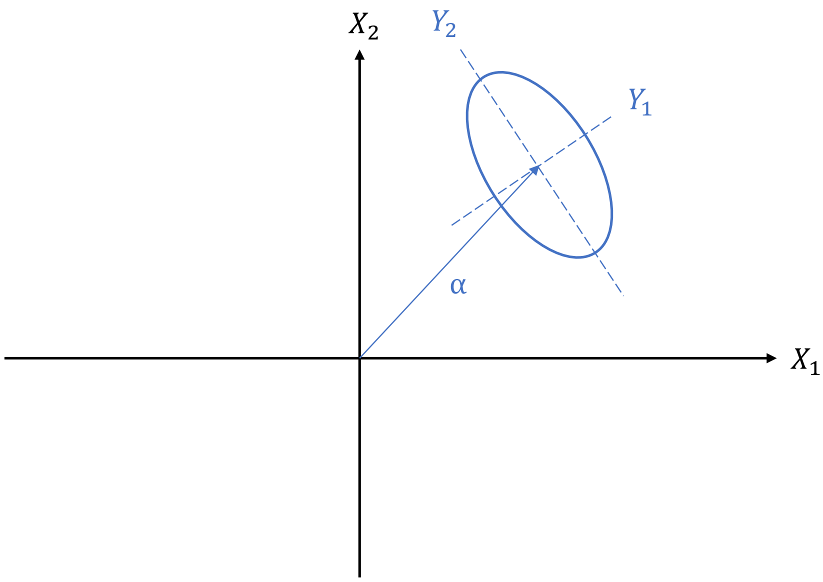

Figure 2.4: Phase space of a quadrature squeezed coherent state where the squeezing happens along the Y_1 axis. The ellipse is displaced by α from the origin.

$$\Delta\hat{Q}^2_{\text{dB}} = 10\log_{10}\left(\frac{\Delta\hat{Q}^2}{\Delta\hat{Q}^2_{\text{vac}}}\right) \tag{2.83}$$

where in our conventions $\Delta\hat{Q}^2_{\text{vac}} = 1$.

2.6 Photon-number squeezing

Let us consider the coherent state, as defined by Eq. (2.42), and look at the photon statistics of it. Using $\bar{n} \equiv \hat{a}^\dagger\hat{a}$ we have

$$\bar{n} = \langle\alpha|\hat{n}|\alpha\rangle = \langle\alpha|\hat{a}^\dagger\hat{a}|\alpha\rangle = \alpha^*\alpha = |\alpha|^2 \tag{2.84}$$

so $|\alpha|^2$ is the average photon number. The fluctuations in the photon number are

$$\begin{aligned}\langle\alpha|\hat{n}^2|\alpha\rangle &= \langle\alpha|\hat{a}^\dagger\hat{a}\hat{a}^\dagger\hat{a}|\alpha\rangle \\ &= \langle\alpha|\hat{a}^\dagger(\hat{a}^\dagger\hat{a}+1)\hat{a}|\alpha\rangle \\ &= \langle\alpha|\hat{a}^\dagger\hat{a}^\dagger\hat{a}\hat{a}|\alpha\rangle + \langle\alpha|\hat{a}^\dagger\hat{a}|\alpha\rangle \\ &= |\alpha|^4 + |\alpha|^2 = \bar{n}^2 + \bar{n}\end{aligned} \tag{2.85}$$

therefore

$$\Delta n = \sqrt{\langle\hat{n}^2\rangle - \langle\hat{n}\rangle^2} = \sqrt{(\bar{n}^2+\bar{n}) - \bar{n}^2} = \sqrt{\bar{n}} \tag{2.86}$$

we see that the standard deviation is the square root of the mean, which is a feature of Poissonian statistics. To see the Poissonian distribution we use Eq. (2.53) to get

$$\begin{aligned}P_n &= |\langle n|\alpha\rangle|^2 \\ &= \exp\left(-|\alpha|^2\right)\left|\sum_{k=0}^{\infty}\frac{\alpha^k}{\sqrt{k!}}\langle n|k\rangle\right|^2 \\ &= \exp\left(-|\alpha|^2\right)\left|\sum_{k=0}^{\infty}\frac{\alpha^k}{\sqrt{k!}}\delta_{nk}\right|^2 \\ &= \exp\left(-|\alpha|^2\right)\left|\frac{\alpha^n}{\sqrt{n!}}\right|^2 \\ &= \exp\left(-|\alpha|^2\right)\frac{|\alpha|^{2n}}{n!} \\ &= \exp(-\bar{n})\frac{\bar{n}^n}{n!}\end{aligned} \tag{2.87}$$

statistical distributions having $\Delta n > \sqrt{\bar{n}}$ are called *super-Poissonian.* Examples are thermal light and light from a discharge lamp. Distributions having $\Delta n < \sqrt{\bar{n}}$ are called *sub-Poissonian* and are a clear signature of non-classical light. A well-known parameter describing this is the Mandel-Q parameter, defined as

$$Q_M = \frac{\langle(\Delta n)^2\rangle - \langle n\rangle}{\langle n\rangle} \tag{2.88}$$

It is clear that $Q_M = 0$ corresponds to Poissonian statistics, $Q_M > 0$ corresponds to super-Poissonian statistics, and $Q_M < 0$ corresponds to sub-Poissonian statistics.

2.7 Experimental progress and applications of squeezed light

Quadrature squeezing of light, the variance of one quadrature being smaller than that of a coherent state (at the expense of the other quadrature being bigger, in accordance with the uncertainty principle) had been experimentally demonstrated during the last 30 years. This section is partly based on the excellent review [5]. Here we describe a couple of different methods that had been implemented experimentally in order to create squeezed light, based on inherent nonlinearities of the corresponding systems.

2.7.1 Parametric down conversion

A common method for generation of squeezed states of light is based on parametric down conversion. It uses a $\chi^{(2)}$ nonlinear susceptibility inherent to certain crystals. In this setup, a pump beam is down-converted into signal and idler beams, with $\omega_p = \omega_s + \omega_i$. Since the $\chi^{(2)}$ nonlinearity is small, high power pulsed lasers are typically required for the pump beam (the opposite process, sum-frequency generation, can also be used to produce squeezed light). The first experiment implementing this method was performed by Wu et al in 1986 [6]. It used a sub-threshold optical parametric oscillator. A laser beam at 532 nm which was frequency doubled was used as the pump, and created a squeezed light in the down-converted beam at 1064 nm. The squeezed vacuum state was analyzed by a homodyne detector. This experiment achieved squeezing of 3.5 dB which was high relative to other methods at the time. With some technical advances, later experiments were able to improve this to $\sim 6\,\text{dB}$. The situation then remained stale for several years. This was eventually surpassed only in 2006, when technological advances were able to overcome the main limitations caused by intra-cavity losses, detector noise and phase noise. Since then, experiments reached higher degrees of squeezing, the highest to date of which was achieved by Vahlbruch et al in 2016 [7] and was able to reach 15 dB.

2.7.2 Atomic vapor

Atomic vapor systems can be used to create squeezed states by exploiting the intrinsic nonlinearity in light-atom interactions of certain systems. The squeezing setup is based on atomic levels arranged in a Λ-configuration where two lower states are coupled to a single excited state (see Figure 3.2). The two transitions from one lower state through the excited state and to the other lower state are known as the Stokes and the anti-Stokes modes. The earliest experiment of this type, and in fact the first experiment to demonstrate squeezed light, was made by Slusher et al in 1985 [8]. In that experiment, a four-wave-mixing (FWM) process occured in an atomic vapor of sodium atoms. Cavities resonating the Stokes and anti-Stokes frequencies increased the interaction, and a local oscillator (LO) at a mid-frequency between the modes was used to detect the squeezing. In that experiment, squeezing of 0.3 dB was measured. This relatively small amount was caused by undesired nonlinear processes such as Raman scattering and fluorescence occuring in addition to the FWM. Later experiments used double-Λ setups which were able to cancel most of the undesired effects, and achieved much higher squeezing of about 9 dB [9].

2.7.3 Optical fibers

Another way to generate squeezed light relies on third-order nonlinearities. Third order processes are much weaker than second order, therefore a practical solution had been the use of optical fibers, where the interaction happens over a long distance. Squeezing in optical fibers relies on four-wave mixing and the third-order Kerr effect. This third-order nonlinearity leads to a change in the index of refraction as a function of the light intensity as [5]: $n = n_0 + n_2 \cdot I$. This creates a situation where higher intensity phase space regions acquire larger phase shifts than lower intensity phase space regions, which transforms a circular coherent state into an elliptical squeezed state in phase space. The first experiment of this type was performed by Shelby et al in 1986 [10] and used a continuous-wave pump to generate the squeezing. Since third-order effects are weak, high powered lasers are required, which also results in some undesired nonlinear effects acting to weaken the amount of squeezing, the most important of which is the Brillouin scattering due to the coupling between photons and phonons in the fiber. To stay below the Brillouin threshold, a phase modulation scheme generating several different wavelengths was used in some experiments, and short pulses which reduce the average power to a level less sensitive to this effect were used in others. Photonic crystal fibers are also able to generate squeezed states [11]. These fibers are attractive because of their higher nonlinearities and flexibility in dispersion management. However, they require careful balancing and so far they had not surpassed the squeezing performance of standard fibers.

2.7.4 Semiconductor devices

A simple method to produce squeezed light is the use of semiconductor devices. Light emitting laser diodes are able to directly emit photons with better than shot-noise statistics. This was first demonstrated in 1987 by Machida et al [12] and the sensitivity was later improved by setting the detector face to face with the laser.

2.7.5 Applications

Squeezed light had been used in multiple fields. Most famously it had been employed in the gravitational waves detectors GEO600 and LIGO [13]. The LIGO detector consists of two 4 km wide arms, forming a Michelson interferometer with the two beams set on a dark fringe. The tiny spacetime fluctuations that gravitational waves create, change the arm length and create a phase shift between the beams as a periodic signal, which can be detected. The current improvements to the system include squeezed light for the detector beam, enabling it to reach sub shot-noise sensitivity. The vacuum squeezed state is created by second harmonic generation. Other applications of squeezed light include quantum error correction [14], sensing and tracking [15], and quantum enhanced imaging resolution of biological samples [16]. Recently, squeezed states had also been successfully implemented in miniaturized systems. Using the intrinsic nonlinear interactions between light and two-level systems, single emitters such as a single semiconductor dot or a single ion in a high finesse cavity had been used. Kerr nonlinearity in CMOS-compatible materials had also been employed [5]. This may hint at the future implementation of squeezed light where such micro components would be put inside bigger systems.

Chapter 3

Refractive index enhancement

In this chapter we look at the behavior of laser light near atomic resonance, and the absorption and refractive index as a function of frequency for different systems. This will be relevant for the next chapter, where we take an index enhancing system and further examine its quantum properties, i.e. the squeezed states and photon statistics it forms under certain conditions. We first consider a two-level atom, and look at the behavior of the susceptibility (classical and quantum mechanical) near resonance. We then turn to a 3-level system implementing electromagnetically induced transparency (EIT). While this system achieves transparency (zero absorption), the refractive index stays close to 1. Motivated by EIT and related approaches, we look at a system that our group theoretically proposed and experimentally demonstrated to achieve enhanced index of refraction while maintaining zero absorption. The original contribution of this thesis part is the quantum optics investigation of squeezed light states in such a refractive index enhancement setup with vanishing absorption, through numerical simulations, discussed in the next chapter.

3.1 Susceptibility of a two-level atom, classical derivation

Here we derive the classical result for the frequency-dependence of the susceptibility, and check how the absorption and index of refraction behave near resonance. A good review of this appears in [17]. To start, we model the electrons in a transparent media as being bounded to the atom by a spring-like potential. The electron's classical equation of motion is

$$m\frac{d^2x}{dt^2} + m\gamma\frac{dx}{dt} + m\omega_0^2 x = eE_0 e^{-i\omega t} \tag{3.1}$$

Here the second term represents decay, the third term represents a spring-like binding force, where ω_0 is a natural frequency of the atom, and the term on the RHS represents an applied electric field of a laser with frequency ω. Looking for steady state solutions $x(t) = x_0 e^{-i\omega t}$ we get

$$x_0 = \frac{e/m}{\omega_0^2 - \omega^2 - i\gamma\omega} E_0 \tag{3.2}$$

the dipole moment is

$$P(t) = ex(t) = \frac{e^2/m}{\omega_0^2 - \omega^2 - i\gamma\omega} E_0 e^{-i\omega t} \tag{3.3}$$

therefore, assuming N atoms per unit volume,

$$\mathbf{P} = \left(\frac{Ne^2/m}{\omega_0^2 - \omega^2 - i\gamma\omega}\right)\mathbf{E} \tag{3.4}$$

comparing this with the expression (for a linear polarization) $\mathbf{P} = \epsilon_0\chi\mathbf{E}$ we get an expression for the complex electric susceptibility:

$$\chi = \frac{Ne^2}{\epsilon_0 m}\left(\frac{1}{\omega_0^2 - \omega^2 - i\gamma\omega}\right) \tag{3.5}$$

the real and imaginary parts of the susceptibility are:

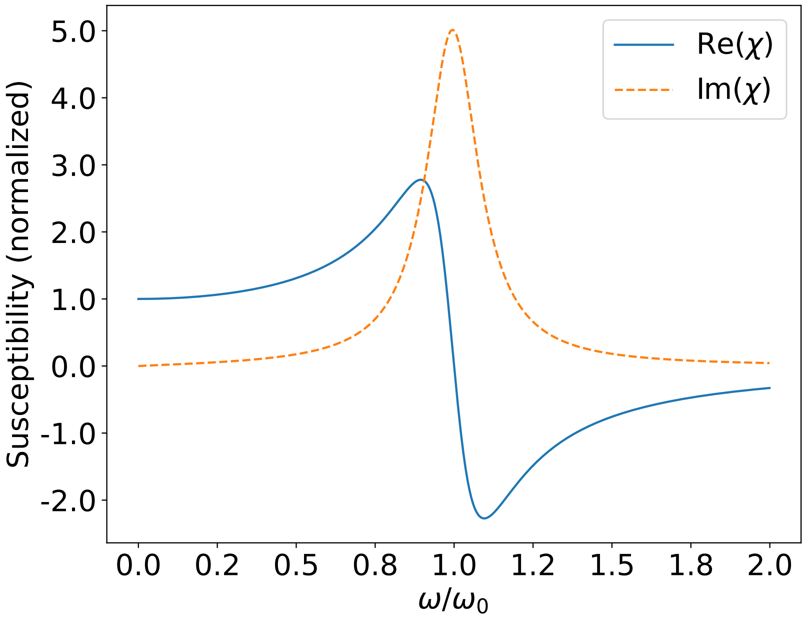

Figure 3.1: The behavior of the classical susceptibility near an atomic resonance. At the resonance $\omega = \omega_0$, Im(χ) spikes which indicates absorption, while Re(χ) vanishes, which leads to a unity refractive index.

$$\chi' = \frac{Ne^2}{\epsilon_0 m} \frac{\omega_0^2 - \omega^2}{(\omega_0^2 - \omega^2)^2 + \gamma^2\omega^2} \tag{3.6}$$

$$\chi'' = \frac{Ne^2}{\epsilon_0 m} \frac{\gamma\omega}{(\omega_0^2 - \omega^2)^2 + \gamma^2\omega^2} \tag{3.7}$$

where $\chi' \equiv \mathrm{Re}(\chi)$ and $\chi'' \equiv \mathrm{Im}(\chi)$. These are sketched in Figure 3.1. Let us look at the meaning of χ' and χ''. We can write the light wave as

$$\mathbf{E} = \mathbf{E}_0 e^{i(\tilde{k}z - \omega t)} \tag{3.8}$$

where $\tilde{k}$ is the complex wave number. Now, the refractive index is

$$\tilde{n} = \frac{c}{v} = \frac{c}{\omega/\tilde{k}} = \frac{c\tilde{k}}{\omega} \tag{3.9}$$

where $\tilde{n}$ is the complex refractive index. Therefore

$$\tilde{k} = \frac{\omega \tilde{n}}{c} = \frac{\omega}{c}\sqrt{1+\chi} \tag{3.10}$$

and since for the rubidium gas in the index enhancement system we will consider later $\chi \ll 1$, we can write

$$\tilde{k} \approx \frac{\omega}{c}\left(1 + \frac{1}{2}\chi\right) = \frac{\omega}{c}\left(1 + \frac{1}{2}\chi' + \frac{i}{2}\chi''\right) \tag{3.11}$$

we therefore have

$$\mathbf{E} = \mathbf{E}_0 e^{-\alpha z} e^{i(kz-\omega t)} \tag{3.12}$$

with α and k real, defined by

$$\alpha = \frac{\omega \chi''}{2c} \tag{3.13}$$

$$k = \frac{\omega n}{c} = \frac{\omega}{c}\left(1 + \frac{1}{2}\chi'\right) \tag{3.14}$$

and n the real refractive index. We see that χ'' is related to the absorption and χ' is related to the real index of refraction. This means that in Figure 3.1 there is a big absorption at resonance while, since $\chi' \approx 0$, the index of refraction is $n \approx (1+\chi'/2) \approx 1$.

3.2 Susceptibility of a two-level atom, quantum-mechanical derivation

Here we derive the behavior of the susceptibility near atomic resonance treating the atomic levels quantum mechanically, while still treating the light classically. Consider a two-level system consisting of energy levels $|1\rangle$ and $|2\rangle$. Denote the electric field by $\vec{E}$. The Hamiltonian of an electron inside the electric field is

$$\hat{H}_{int} = eE\hat{x} = -\hat{\mu}E \tag{3.15}$$

where the dipole moment operator is $\hat{\mu} = -e\hat{x}$. Therefore for a two-level atom

$$\hat{H} = H_0 + H_{int} = \hbar\omega_1 |1\rangle \langle 1| + \hbar\omega_2 |2\rangle \langle 2| - \hat{\mu}E \tag{3.16}$$

the wave function of the electron in the atom can be written:

$$|\psi\rangle = c_1(t)e^{-i\omega_1 t} |1\rangle + c_2(t)e^{-i\omega_2 t} |2\rangle \tag{3.17}$$

where c_1 and c_2 are the probability amplitudes to be in states $|1\rangle$ and $|2\rangle$, respectively. putting this in the Schrodinger equation:

$$i\hbar \frac{d |\psi\rangle}{dt} = \hat{H} |\psi\rangle \tag{3.18}$$

and defining $\omega_0 \equiv \omega_2 - \omega_1$ as the atomic resonance frequency and $\mu_{12} = \langle 2|\hat{\mu}|1\rangle$ we get

$$\frac{dc_1}{dt} = \frac{i}{\hbar} E(t) e^{-i\omega_0 t} \mu_{12} c_2 \tag{3.19}$$

$$\frac{dc_2}{dt} = \frac{\gamma}{2} c_2 + \frac{i}{\hbar} E(t) e^{i\omega_0 t} \mu_{12}^* c_1 \tag{3.20}$$

where we added the loss term $(\gamma/2)c_2$ by hand. Now, let us define $\rho_{12} \equiv c_1 c_2^*$ as the coherence of the transition. From the above equations we get

$$\begin{aligned}
\frac{d\rho_{12}}{dt} &= \frac{d}{dt}(c_1 c_2^*) \\
&= \frac{dc_1}{dt} c_2^* + c_1 \frac{dc_2^*}{dt} \\
&= \frac{i}{\hbar} E(t) e^{-i\omega_0 t} \mu_{12} c_2 c_2^* - \frac{i}{\hbar} E(t) e^{-i\omega_0 t} \mu_{12} c_1 c_1^* - (\gamma/2) c_1 c_2^* \\
&= -\frac{\gamma}{2} \rho_{12} + \frac{i}{\hbar} E(t) e^{-i\omega_0 t} \mu_{12} (|c_2|^2 - |c_1|^2)
\end{aligned} \tag{3.21}$$

where $|c_1|^2$ and $|c_2|^2$ are the probabilities that the atom is in state $|1\rangle$ or $|2\rangle$, respectively. Let us take the electric field as

$$E(t) = \Re(E_0 e^{i\omega t}) = \frac{1}{2}E_0 e^{i\omega t} + \frac{1}{2}E_0^* e^{-i\omega t} \tag{3.22}$$

the coherence equation becomes

$$\begin{aligned}\frac{d\rho_{12}}{dt} + \frac{\gamma}{2}\rho_{12} = \frac{i}{2\hbar}E_0 e^{i(\omega-\omega_0)t}\mu_{12}(|c_2|^2 - |c_1|^2) \\ + \frac{i}{2\hbar}E_0^* e^{-i(\omega+\omega_0)t}\mu_{12}(|c_2|^2 - |c_1|^2)\end{aligned} \tag{3.23}$$

consider the system close to a resonance. Then the second term contributes $\int e^{-i(\omega+\omega_0)} \sim 1/(\omega+\omega_0)$ which is much smaller than first term $\int e^{i(\omega-\omega_0)} \sim 1/(\omega-\omega_0)$. Neglecting the second term, we get

$$\frac{d\rho_{12}}{dt} + \frac{\gamma}{2}\rho_{12} = \frac{i}{2\hbar}E_0 e^{i(\omega-\omega_0)t}\mu_{12}(|c_2|^2 - |c_1|^2) \tag{3.24}$$

and near a steady state where c_1 and c_2 are time independent, we get the solution

$$\rho_{12} = \frac{E_0\,\mu_{12}\,e^{i(\omega-\omega_0)}}{\hbar[2(\omega-\omega_0) - i\gamma]}(|c_2|^2 - |c_1|^2) \tag{3.25}$$

The average dipole is

$$\begin{aligned}\langle\hat{\mu}\rangle &= \langle\psi|\hat{\mu}|\psi\rangle \\ &= (c_1^* e^{i\omega_1 t}\langle 1| + c_2^* e^{i\omega_2 t}\langle 2|)\hat{\mu}(c_1 e^{-i\omega_1 t}|1\rangle + c_2 e^{-i\omega_2 t}|2\rangle) \\ &= c_1^* c_2 e^{-i\omega_0 t}\mu_{12} + c_1 c_2^* e^{i\omega_0 t}\mu_{12}^* \\ &= \rho_{12}^* e^{-i\omega_0 t}\mu_{12} + \rho_{12} e^{i\omega_0 t}\mu_{12}\end{aligned} \tag{3.26}$$

and substituting the ρ_{12} solution from Eq. (3.25), we get

$$\langle\hat{\mu}\rangle = \frac{E_0|\mu_{12}|^2}{\hbar[2(\omega-\omega_0) - i\gamma]}(|c_2|^2 - |c_1|^2)e^{i\omega t} + \text{c.c} \tag{3.27}$$

Suppose that the total number of atoms is N. The polarization is defined as $P = N\langle\hat{\mu}\rangle$. Let the number of atoms in states $|1\rangle$ and $|2\rangle$ be $N_1 = N|c_1|^2$ and $N_2 = N|c_2|^2$. Then, defining $P = \Re(P_0 e^{i\omega t})$, we have

$$\mathbf{P} = \frac{2|\mu_{12}|^2}{\hbar[2(\omega-\omega_0)-i\gamma]}(N_2 - N_1)\mathbf{E} \tag{3.28}$$

Now, from the relation of the linear polarization being proportional to the electric field

$$\mathbf{P} = \epsilon_0 \chi \mathbf{E} \tag{3.29}$$

we read off the susceptibility:

$$\chi_{\text{quantum}} = \frac{2|\mu_{12}|^2}{\hbar\epsilon_0}(N_1 - N_2)\frac{1}{2(\omega_0-\omega)-i\gamma} \tag{3.30}$$

This has the same lineshape (up to a constant) as the classical result in Eq. (3.5). To see this, we can take the Lorentzian of the classical lineshape:

$$\chi_{\text{classical}} = \frac{Ne^2}{\epsilon_0 m}\left(\frac{1}{\omega_0^2-\omega^2-i\gamma\omega}\right) \tag{3.31}$$

and using the fact that close to the resonance, $\omega \approx \omega_0$, we get

$$\begin{aligned}
\chi_{\text{classical}} &= \frac{Ne^2}{\epsilon_0 m}\left(\frac{1}{(\omega_0+\omega)(\omega_0-\omega)-i\gamma\omega}\right) \\
&\approx \frac{Ne^2}{\epsilon_0 m}\left(\frac{1}{2\omega_0(\omega_0-\omega)-i\gamma\omega_0}\right) \\
&= \frac{Ne^2}{\epsilon_0 m\omega_0}\,\frac{1}{2(\omega_0-\omega)-i\gamma}
\end{aligned} \tag{3.32}$$

in the classical limit, the quantum result becomes $(N_1 - N_2) \to N$ and the results are similar (up to different constants, since they are expressed using different quantities).

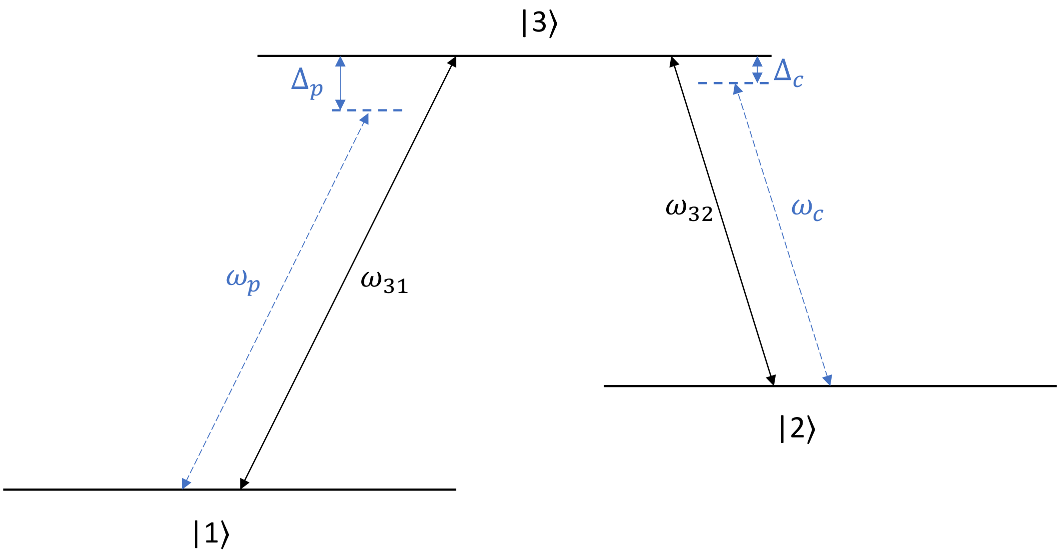

Figure 3.2: The Λ-configuration of EIT setup. The energy differences (in frequency units) between levels $|1\rangle$ and $|3\rangle$ and between levels $|2\rangle$ and $|3\rangle$ are indicated as ω_{31} and ω_{32}. A probe beam excites atoms from level $|1\rangle$ to level $|3\rangle$ with detuning Δ_p while the control beam excites the transition from $|2\rangle$ to $|3\rangle$ with detuning Δ_c. The $|2\rangle$ to $|1\rangle$ transition is dipole forbidden. If the control beam is much more intense than the probe, the resonances interfere destructively and create vanishing absorption.

3.3 Electromagnetically Induced Transparency (EIT)

Electromagnetically Induced Transparency (EIT) is an optical process in which probe laser photons that correspond to a resonance of the atom are made transparent at that frequency, through quantum interference with another transition. The quantum interference is achieved by driving the atoms to a dark state, which is a properly phased superposition of two lower metastable levels. EIT is typically implemented in a Λ configuration: a three level atomic system interacting with two lasers, a probe and a control laser. To be concrete, let us consider the following Λ-configuration, which is shown in Figure 3.2. This configuration has a ground state $|1\rangle$, a metastable state $|2\rangle$, and an excited radiating state $|3\rangle$.

In this configuration a probe beam at frequency ω_p is near-resonant with the $|1\rangle \rightarrow |3\rangle$ transition, with detuning Δ_p. Let $\omega_{31} = \omega_3 - \omega_1$ be the frequency difference between levels $|1\rangle$ and $|3\rangle$. Then $\Delta_p = |\omega_p - \omega_{31}|$. A second, control laser with frequency ω_c is near-resonant with the $|2\rangle \rightarrow |3\rangle$ transition with detuning Δ_c. Let $\omega_{32} = \omega_3 - \omega_2$ be the frequency difference of these levels. Then $\Delta_c = |\omega_c - \omega_{32}|$. The transition $|1\rangle \leftrightarrow |2\rangle$ is dipole forbidden. In this system, because the $|2\rangle \leftrightarrow |1\rangle$ transition is dipole forbidden, $|3\rangle$ is the only state capable of incoherent absorption. There are two pathways for $|3\rangle$ to absorb photons, $|1\rangle \rightarrow |3\rangle$ and $|1\rangle \rightarrow |3\rangle \rightarrow |2\rangle \rightarrow |3\rangle$ (or higher order transitions). Since the control laser is much more intense than the probe, these two pathways have effectively equal probability amplitudes while interfering with opposite relative signs, which results in zero total amplitude.

Calculating the susceptibility, which is the response of the atoms to the applied electric fields of the lasers, will allow us to calculate the refractive index and the absorption, and see the behavior near a resonance. The susceptibility can be derived using the density matrix formalism. A detailed analysis appears in [18]. Relying on this and quoting the analysis results, we assume for simplicity that $\Delta_c = 0$ (the control laser is exactly at resonance) and also $\Gamma_{21} = 0$ (the decay between levels $|2\rangle \rightarrow |1\rangle$, which is dipole forbidden, is negligible) the susceptibility is

$$\chi = \frac{N\mu_{3,1}^2}{\epsilon_0 \hbar} \frac{2\Delta_p}{4\Delta_p^2 + 2i\Gamma\Delta_p - \Omega_c^2} \tag{3.33}$$

where $\Gamma \equiv \Gamma_{31} + \Gamma_{32}$ is the total decay rate from level $|3\rangle$ into levels $|2\rangle$ and $|1\rangle$. This gives

$$\chi' = \frac{N\mu_{3,1}^2}{\epsilon_0 \hbar} \frac{8\Delta_p^3 - 2\Delta_p\Omega_c^2}{(4\Delta_p^2 - \Omega_c^2)^2 + 4\Gamma^2\Delta_p^2} \tag{3.34}$$

$$\chi'' = \frac{N\mu_{3,1}^2}{\epsilon_0 \hbar} \frac{-4\Gamma\Delta_p^2}{(4\Delta_p^2 - \Omega_c^2)^2 + 4\Gamma^2\Delta_p^2} \tag{3.35}$$

These susceptibilities are plotted in Figure 3.3 for $\Omega_c = 1\Gamma$ and for $\Omega_c = 4\Gamma$. We see that for $\Delta_p = 0$ there is zero absorption. For $\Omega_c = 4\Gamma$ the "window of transparency" is larger than for $\Omega_c = 1\Gamma$ and there is some index of enhancement, but it is not significant. In the scheme that we describe in the next section, the index enhancement is significant in the region of zero absorption. Other applications of EIT include, for example, reduced group velocity:

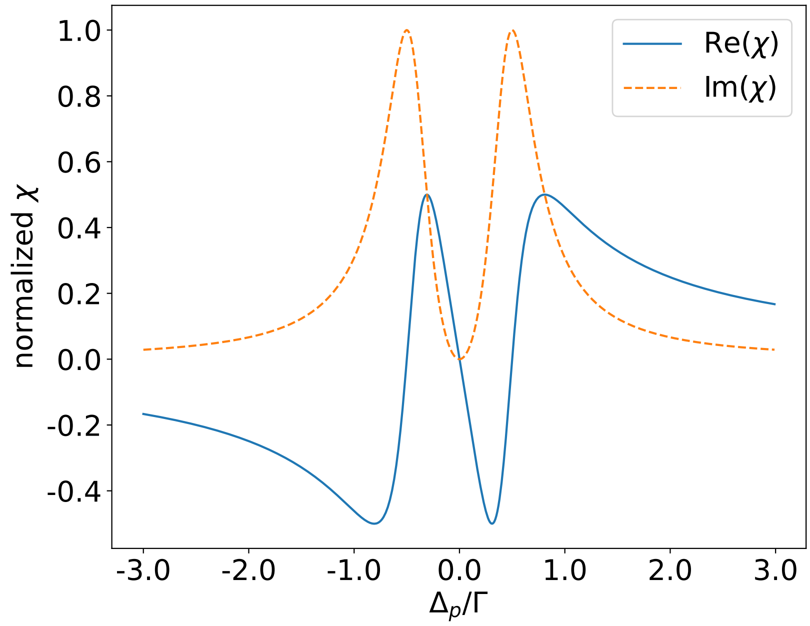

(a) Electric susceptibility as a function of the detuning of the probe beam from resonance, for $\Omega_c = 1\Gamma$

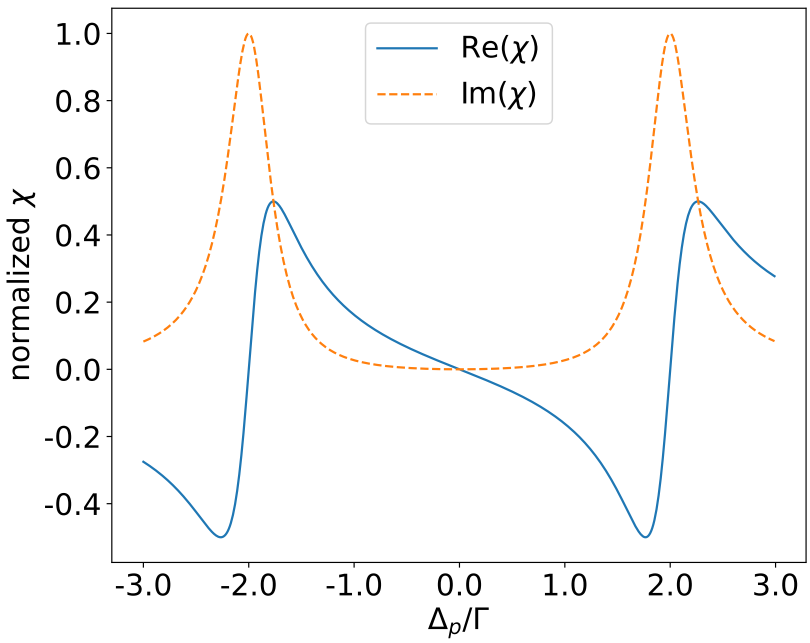

(b) Electric susceptibility as a function of the detuning of the probe beam from resonance, for $\Omega_c = 4\Gamma$

Figure 3.3: Real and imaginary parts of the susceptibility in the Λ configuration of EIT. The imaginary part vanishes between the resonances, while in the same region the real part is mildly enhanced. In part (a) taking the control laser Rabi frequency $\Omega_c = 1\Gamma$. In part (b) the frequency is increased to $\Omega_c = 4\Gamma$, this extends the zero absorption region while allowing the refraction index to slightly increase, but the effect is not significant.

$$v_g = \frac{c}{n(\omega) + \omega \frac{dn}{d\omega}} \tag{3.36}$$

since the slope $dn/d\omega$ can be engineered to change fast near a resonance, as in Figure 3.3a (in general this depends on the parameters), the group velocity of light through the atoms can be made very slow. EIT has a wide variety of applications. A detailed review of EIT, including applications such as dark states, stopped and slow light and EIT with few photons is provided by Fleischhauer [19].

3.4 Index enhancement setup

In the previous section we discussed how two pathways interfere destructively to create zero absorption in an EIT setup. However, the index of refraction was low as well, making this property not very useful. Here we review a setup that was developed by our group in the recent years, which allows for enhancement of the refractive index while maintaining zero absorption. The theoretical analysis is described in [20] and we discuss the result here. Figure 3.4 describes the energy level situation. It consists of two resonance transitions, one between the ground level and level 1, and the other between the ground level and level 2. Each of these implements a combination of a probe laser beam and a control laser beam, by first exciting a photon into a virtual state. We let $\delta\omega_1$ be the detuning of the laser transition from the ground level to level $|1\rangle$, that is, $\delta\omega_1 = (\omega_1 - \omega_g) - (\omega_{c1} - \omega_p)$, and $\delta\omega_2$ be the detuning of the transition to level $|2\rangle$, $\delta\omega_2 = (\omega_2 - \omega_g) - (\omega_p - \omega_{c2})$. The excited state $|e\rangle$ is far detuned from the transitions. We also let Γ_e, γ_1 and γ_2 be the decay rates of levels $|e\rangle$, $|2\rangle$ and $|1\rangle$, and assume for simplicity that the decays are all out of the system, which allows the use of Schrodinger approach for solving the equations rather than using the density matrix formalism. The probe beam is much weaker than the two control lasers. Treating the equations perturbatively and assuming that most of the atomic population remains in the ground state, the resulting susceptibility is

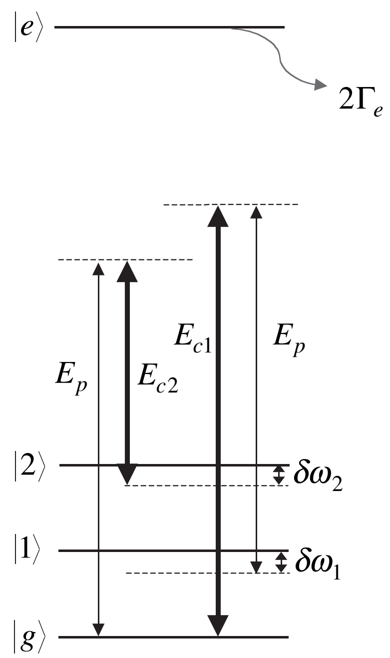

Figure 3.4: The refractive index enhancement setup, involving two resonant Raman transitions, each with a probe laser and a control laser. One of them is absorptive in the probe beam and the other is amplifying. The quantum interference of these transitions results in zero absorption and an enhanced refractive index. Adapted from [20]

$$\chi = \frac{2\hbar N}{\epsilon_0}\left(a_p + \frac{|b_1|^2}{2\delta\omega_1 - i[\gamma_1 + \Im(D_1)/2]}|E_{c1}|^2 + \frac{|b_2|^2}{2\delta\omega_2 + i[\gamma_1 + \Im(D_2)]/2}|E_{c2}|^2\right)E_p \tag{3.37}$$

where N is the atom density, a_p, b_1 and b_2 are Lorentzian-shaped expressions involving the dipole matrix element, frequencies and the decay rate. D_1 and D_2 are related to the field intensities and terms similar to a_p. For the choice $\delta\omega_1 = \delta\omega_2 = \Delta/2$ where Δ is the frequency separation between the resonances, this expression predicts an increased value of the real part of the susceptibility, corresponding to enhancement of the refractive index, while resulting in a zero value of the imaginary part of the susceptibility, resulting in vanishing absorption. Choosing the control lasers frequencies determines the frequency separation of the resonances. When the frequency separation is too large (compared with the linewidth) the resonances are separate and barely affect each other, resulting in low susceptibility. When the separation is too small, the resonances cancel each other out. The maximum index enhancement therefore occurs for a finite frequency separation, depending on the linewidth and the transition detunings. From simulations based on this calculation, it turns out that the maximum index enhancement occurs for $\Delta = 2\gamma_1$, where γ_1 is the decay rate from level $|1\rangle$. Following this, Yavuz group had implemented this setup experimentally. In the initial experiment [2] two separate isotopes of Rb had been used, ^{85}Rb and ^{87}Rb. The situation is show in Figure 3.5. The combination of a probe laser beam exciting photons to a virtual level, and a control laser beam (starting from a pumped $F = 2$ hyperfine level of ^{87}Rb) corresponded to an amplifying resonance of the probe beam, from the $F = 1$ to the $F = 2$ hyperfine levels of ^{87}Rb. At the same time, the combination of the probe beam, in an absorption resonance this time, with another control beam, corresponded to another Raman resonance transition, from the $F = 2$ to the $F = 3$ hyperfine levels in ^{85}Rb. Scanning the probe laser frequency (and setting the the control laser frequencies accordingly to match atomic resonance), it is possible to plot graphs of the real and imaginary parts of the susceptibility, or equivalently the index of refraction and the absorption, as a function of the probe laser frequency. The theoretical prediction line along with the experimental results for resonance separation of 0.2MHz corresponding to the maximum index enhancement, are shown in Figure 3.6 [2]. In the experiment, the amount of absorption was determined by measuring the probe beam intensity, and the index of refraction was determined by measuring the transmission of the beam through a pinhole and the amount of spreading of the beam. This experiment had achieved an index of refraction enhancement of $\Delta n \approx 2 \times 10^{-7}$. The main limitation in this experiment had been the cross-coupling of the two optical pumping processes for the two isotopes of Rubidium. In a later experiment [3] a single isotope of ^{85}Rb had been used. The Raman transitions had been between the F=2 and F=3 hyperfine levels, as shown in Figure 3.7. The results for the intensity as a function of the probe frequency (for different powers of one of the control laser frequencies) are shown in Figure 3.8 and indicate the increased intensity. Figure 3.9 shows the real and imaginary parts of the index of refraction. It is apparent that while the absorption (dashed line) is zero, the real part of the refractive index is enhanced. This experiment was able to achieve $|\Delta n| = |n - 1| \approx 0.4 \times 10^{-4}$.

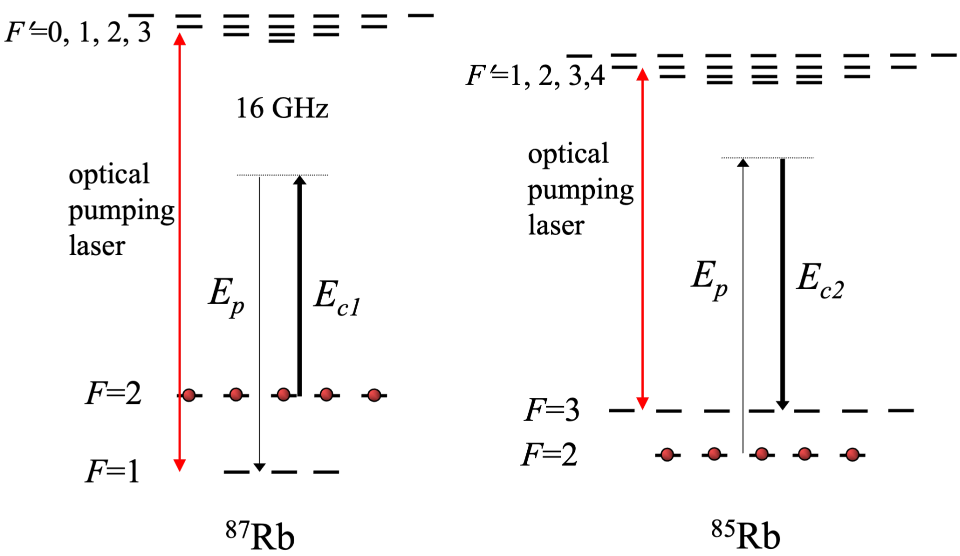

Figure 3.5: The energy diagram for the refractive index enhancement experiment. Two resonant Raman transitions are interfering to create zero absorption and an enhanced refractive index, just like in the theoretical calculation in Figure 3.4. The experimental system used hyperfine transitions in two different Rubidium isotopes. Adapted from [2].

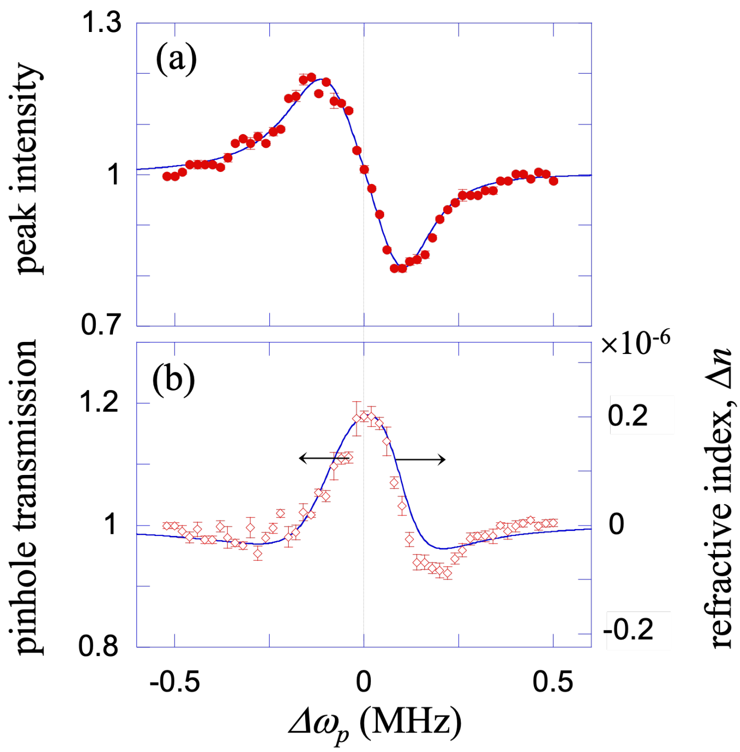

Figure 3.6: The index enhancement experimental results, along with the theoretical prediction (solid line) assuming a Lorentzian line shape, for a resonance separation of 0.2MHz corresponding to maximum index enhancement. The intensity pattern (top image) shows zero absorption between the resonances, while the pinhole transition (bottom image) measures the refractive index and shows an enhancement of the refractive index at that point. Adapted from [2].

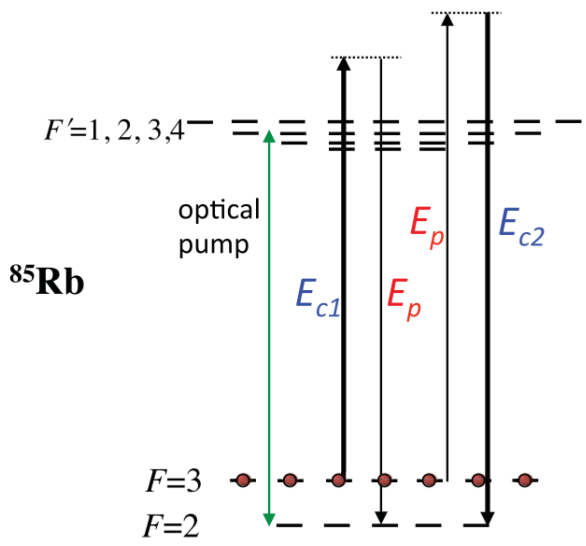

Figure 3.7: The energy diagram of the later experiment for achieving index of refraction enhancement, involving single ^{85}Rb species. A pump to hyperfine level $F = 3$ is required. This setup eliminates the cross coupling problem. Adapted from [3].

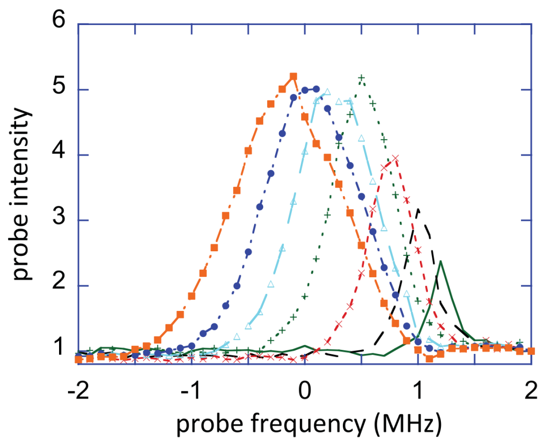

Figure 3.8: The normalized transmitted intensity $I_{\mathrm{out}}/I_{\mathrm{in}}$, as a function of the probe laser frequency, for different input control laser 1 powers. This demontrates the nonzero intensity between the resonance frequencies. Adapted from [3].

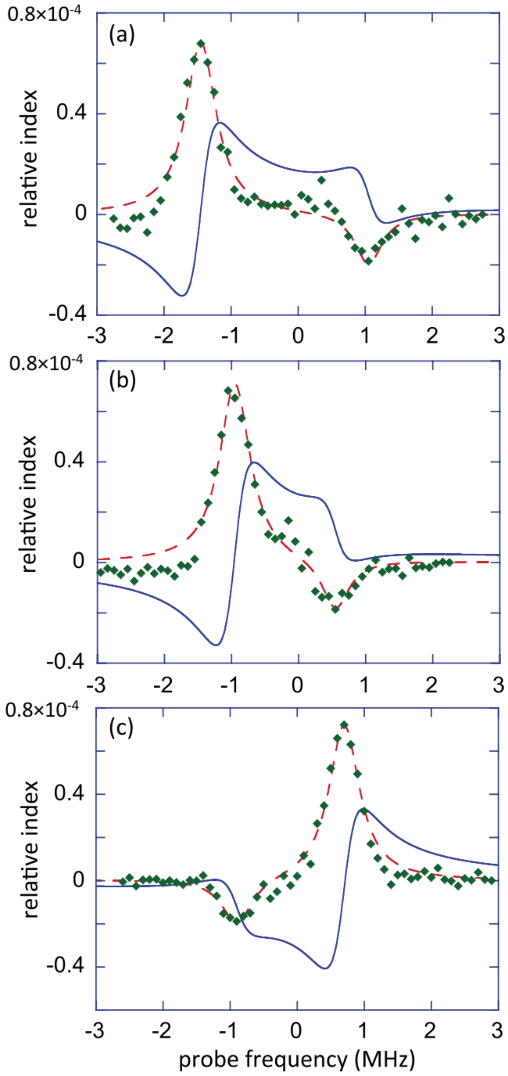

Figure 3.9: The real and imaginary parts of the susceptibility for the index enhancement setup involving single ^{85}Rb species. The imaginary part (dashed line) represents absorption, which is approximately zero between the resonances, while the real part represents the index of refraction. In the top two plots the gain resonance occurs before the absorption, while in the bottom one the situation in reversed. This setup achieved $|\Delta n| \approx 0.4 \times 10^{-4}$. Adapted from [3].

Chapter 4

Squeezed states in a refractive index enhancement setup

4.1 Introduction

The system discussed in the previous section allows for index of refraction enhancement while maintaining zero absorption. This is achieved by using the interference of two Raman transitions: one absorptive and one amplifying in the probe beam. The enhancement is due to the constructive interference of the real parts of the susceptibility, while destructive interference of the imaginary parts leads to vanishing absorption. We consider this type of system, and for simplicity assume that both transitions occur between the same atomic levels, as shown in Figure 4.1. As we will discuss below, it turns out that this type of system also exhibits quadrature squeezing or photon-number squeezing (sub-Poissonian light) of the probe laser photons, for appropriate choice of the system parameters. This is remarkable, since it happens without an explicit nonlinearity in the system. The squeezing obtained here is also a result of the interference between the two resonances in the system. Recently, a linear system of two qubits coupled to a cavity was shown to create squeezed light with hyperradiance [21], giving another example of linear system components resulting in squeezed states. In this chapter we investigate these squeezed light properties. Since the control lasers are much more intense than the

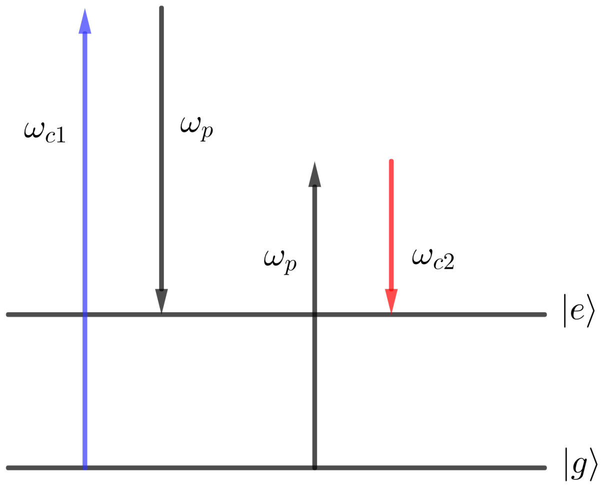

Figure 4.1: Energy level diagram of our setup. Two resonance transitions, each with a probe beam and a control laser beam, one absorptive and one amplifying in the probe beam. This is similar to the index enhancement setup discussed the previous section, but for simplicity the two transitions occur between the same two levels.

probe, they will be treated classically, while the probe beam will be treated quantum mechanically using creation and annihilation operators.

4.2 Formalism and notation

We describe the system by a Hamiltonian of the form, $\hat{H} = \hat{H}_0 + \hat{H}_I$, where the non-interacting part of the Hamiltonian, due to the probe laser and the two-level atom, is

$$\hat{H}_0 = \hbar\omega_p \hat{a}^\dagger \hat{a} + \hbar\omega_a \hat{\sigma}^\dagger \hat{\sigma} \tag{4.1}$$

and the interaction Hamiltonian is

$$\hat{H}_I = i\hbar g_1 \exp\left[-i\left(\omega_{c2} + \Delta_2\right)t\right]\hat{a}^\dagger \hat{\sigma}^- + i\hbar g_2 \exp\left[i\left(\omega_{c1} + \Delta_1\right)t\right]\hat{a}\hat{\sigma}^- + \text{c.c} \tag{4.2}$$

Here, the quantities ω_p, ω_{c1} and ω_{c2} are the angular frequencies of the the probe and the two control lasers, g_1 and g_2 are the strengths of the two Raman resonances, which depend on the electric dipole matrix element of the transition, the atomic energy level and the probe beam frequency [22]. For a specific atomic or molecular system, the interaction strengths can be calculated by using couplings to the excited upper levels (not shown in Figure 4.1), and the frequency (energy) detunings of the interacting lasers from these levels. $\hat{a}$ and $\hat{a}^\dagger$ are the photon annihilation and creation operators for the probe laser. $\hat{\sigma}^- = |g\rangle\langle e|$ and $\hat{\sigma}^+ = |e\rangle\langle g|$ are the lowering and raising operators for the atomic system. Δ_1 and Δ_2 are the two-photon detunings from the Raman transition, and are defined as $\Delta_1 = (\omega_{c1} - \omega_p) - (\omega_e - \omega_g)$ and $\Delta_2 = (\omega_p - \omega_{c2}) - (\omega_e - \omega_g)$, respectively. In Eq. (4.2), we have considered the interaction of the lasers only with a single atom, for simplicity. This can be straightforwardly extended to multiple atoms by using summation over the different atoms in the Hamiltonian. We will consider this case in some of the numerical simulations later in this chapter.

4.3 Analytical analysis

Although it is not possible to fully solve this Hamiltonian analytically, it is possible to obtain analytical solutions for some specific conditions. In this section we examine the solutions in two cases: In a vacuum while the operators $\hat{a}$ and $\hat{a}^\dagger$ vary slowly, and a perturbative solution to Schrodinger's equation. Numerical results for more general cases are discussed in the later sections of this chapter.

4.3.1 Exact calculation with a vacuum state

Here we illustrate the main steps and the results of the calculation. The full calculation is included in Appendix A.1. Based on Eqs. (4.1), (4.2) the full Hamiltonian of the system is:

$$\begin{aligned}\hat{H} = \hbar\omega_p\hat{a}^\dagger\hat{a} + \hbar\omega_a\hat{\sigma}^+\hat{\sigma}^- + i\hbar g_1 \exp\left[-i\left(\omega_{c2} + \Delta_2\right)t\right]\hat{a}^\dagger\hat{\sigma}^- + i\hbar g_2 \exp\left[i\left(\omega_{c1} + \Delta_1\right)t\right]\hat{a}\hat{\sigma}^- \\ - i\hbar g_1^* \exp\left[i\left(\omega_{c2} + \Delta_2\right)t\right]\hat{a}\hat{\sigma}^+ - i\hbar g_2^* \exp\left[-i\left(\omega_{c1} + \Delta_1\right)t\right]\hat{a}^\dagger\hat{\sigma}^+\end{aligned} \tag{4.3}$$

we work in the Heisenberg picture here. The Heisenberg equations for $\hat{a}$ and $\hat{\sigma}$ are:

$$\frac{d\hat{a}}{dt} = \frac{1}{i\hbar}\left[\hat{a}, \hat{H}\right], \qquad \frac{d\hat{\sigma}}{dt} = \frac{1}{i\hbar}\left[\hat{\sigma}, \hat{H}\right] \tag{4.4}$$

these yield the equations of motion:

$$\begin{aligned}\frac{d\hat{a}}{dt} &= -i\omega_p\hat{a} + g_1\exp\left[-i\left(\omega_{c2}+\Delta_2\right)t\right]\hat{\sigma}^- - g_2^*\exp\left[-i\left(\omega_{c1}+\Delta_1\right)t\right]\hat{\sigma}^+\\ \frac{d\hat{\sigma}}{dt} &= -i\omega_a\hat{\sigma}_z\hat{\sigma}^- + g_1^*\exp\left[i\left(\omega_{c2}+\Delta_2\right)t\right]\hat{a}\hat{\sigma}_z + g_2^*\exp\left[-i\left(\omega_{c1}+\Delta_1\right)t\right]\hat{a}^\dagger\hat{\sigma}_z\end{aligned} \tag{4.5}$$

now, to get rid of the first term on the RHS of these equations, we define

$$\begin{aligned}\hat{a} &\equiv \tilde{\hat{a}}\exp\left(-i\omega_p t\right)\\ \hat{\sigma} &\equiv \hat{\sigma}_z\tilde{\hat{\sigma}}\exp\left(-i\omega_a t\right)\end{aligned} \tag{4.6}$$

substitution into the equations and also using the definitions

$$\begin{aligned}\omega_{c1}+\Delta_1-\omega_p-\omega_a &\equiv \delta\omega_1\\ \omega_{c2}+\Delta_2-\omega_p+\omega_a &\equiv \delta\omega_2\end{aligned} \tag{4.7}$$

we get the equations for $\tilde{\hat{a}}$ and $\tilde{\hat{\sigma}}$:

$$\begin{aligned}\frac{d\tilde{\hat{a}}}{dt} &= g_1\exp\left(-i\delta\omega_2 t\right)\tilde{\hat{\sigma}}^- - g_2^*\exp\left(-i\delta\omega_1 t\right)\tilde{\hat{\sigma}}^+\\ \frac{d\tilde{\hat{\sigma}}}{dt} &= g_1^*\exp\left(i\delta\omega_2 t\right)\tilde{\hat{a}} + g_2^*\exp\left(-i\delta\omega_1 t\right)\tilde{\hat{a}}^\dagger\end{aligned} \tag{4.8}$$

to proceed, we make the simplifying assumption that $\tilde{\hat{a}}$, $\tilde{\hat{a}}^+$ vary much slower than $\exp(i\delta\omega_1 t)$ and $\exp(i\delta\omega_2 t)$. Then from the second equation:

$$\tilde{\hat{\sigma}}\left(t\right) = \frac{g_1^*}{i\delta\omega_2}\exp\left(i\delta\omega_2 t\right)\tilde{\hat{a}} - \frac{g_2^*}{i\delta\omega_1}\exp\left(-i\delta\omega_1 t\right)\tilde{\hat{a}}^\dagger \tag{4.9}$$

substituting this in the first equation, we get

$$\frac{d\tilde{\hat{a}}}{dt} = -i\left(\frac{|g_1|^2}{\delta\omega_2} - \frac{|g_2|^2}{\delta\omega_1}\right)\tilde{\hat{a}} + ig_1g_2^*\left(\frac{1}{\delta\omega_1} - \frac{1}{\delta\omega_2}\right)\exp\left[-i\left(\delta\omega_1 + \delta\omega_2\right)t\right]\,\tilde{\hat{a}}^\dagger \tag{4.10}$$

Now we calculate the quadratures. Defining $\hat{Q} = \hat{a} + \hat{a}^\dagger$, we have

$$\frac{d\hat{Q}}{dt} = \frac{d\hat{a}}{dt} + \frac{d\hat{a}^\dagger}{dt} \tag{4.11}$$

expressing this using $\tilde{\hat{a}}$ and $\tilde{\hat{a}}^\dagger$ and using Eq. (4.10) we can write this in terms of $\tilde{\hat{a}}$ and $\tilde{\hat{a}}^\dagger$ (see Appendix A.1 for full details):

$$\begin{aligned}\frac{d\hat{Q}}{dt} = &\left\{-i\left(\frac{|g_1|^2}{\delta\omega_2} - \frac{|g_2|^2}{\delta\omega_1} + \omega_p\right)\exp\left(-i\omega_p t\right)\right.\\ &\left.-ig_1^*g_2\left(\frac{1}{\delta\omega_1} - \frac{1}{\delta\omega_2}\right)\exp\left[i\left(\delta\omega_1 + \delta\omega_2\right)t\right]\exp\left(i\omega_p t\right)\right\}\tilde{\hat{a}}\\ &+\left\{i\left(\frac{|g_1|^2}{\delta\omega_2} - \frac{|g_2|^2}{\delta\omega_1} + \omega_p\right)\exp\left(i\omega_p t\right)\right.\\ &\left.+ig_1g_2^*\left(\frac{1}{\delta\omega_1} - \frac{1}{\delta\omega_2}\right)\exp\left[-i\left(\delta\omega_1 + \delta\omega_2\right)t\right]\exp\left(-i\omega_p t\right)\right\}\tilde{\hat{a}}^\dagger\end{aligned} \tag{4.12}$$

Then, using $\hat{Q}^2 = \left(\hat{a} + \hat{a}^\dagger\right)^2 = \hat{a}^2 + \hat{a}\hat{a}^\dagger + \hat{a}^\dagger\hat{a} + \hat{a}^{\dagger 2}$, we can similarly express $d(\hat{Q}^2)/dt$ in terms of $\tilde{\hat{a}}$ and $\tilde{\hat{a}}^\dagger$. The result is (see Appendix A.1):

$$
\begin{aligned}
\frac{d\left(\hat{Q}^2\right)}{dt} =& \left\{-2i\left(\frac{|g_1|^2}{\delta\omega_2}-\frac{|g_2|^2}{\delta\omega_1}\right)\exp\left(-2i\omega_p t\right)\right.\\
&\left.-2i\,g_1^*g_2\left(\frac{1}{\delta\omega_1}-\frac{1}{\delta\omega_2}\right)\exp\left[i\left(\delta\omega_1+\delta\omega_2\right)t\right]\right\}\tilde{\hat{a}}^2\\
&+\left\{2ig_1g_2^*\left(\frac{1}{\delta\omega_1}-\frac{1}{\delta\omega_2}\right)\exp\left[-i\left(\delta\omega_1+\delta\omega_2\right)t\right]\right.\\
&\left.+2i\left(\frac{|g_1|^2}{\delta\omega_2}-\frac{|g_2|^2}{\delta\omega_1}\right)\exp\left(2i\omega_p t\right)\right\}\tilde{\hat{a}}^{\dagger 2}\\
&+\left\{ig_1g_2^*\left(\frac{1}{\delta\omega_1}-\frac{1}{\delta\omega_2}\right)\exp\left(-2i\omega_p t\right)\exp\left[-i\left(\delta\omega_1+\delta\omega_2\right)t\right]\right.\\
&\left.-ig_1^*g_2\left(\frac{1}{\delta\omega_1}-\frac{1}{\delta\omega_2}\right)\exp\left(2i\omega_p t\right)\exp\left[i\left(\delta\omega_1+\delta\omega_2\right)t\right]\right\}\tilde{\hat{a}}^\dagger\tilde{\hat{a}}\\
&+\left\{ig_1g_2^*\left(\frac{1}{\delta\omega_1}-\frac{1}{\delta\omega_2}\right)\exp\left(-2i\omega_p t\right)\exp\left[-i\left(\delta\omega_1+\delta\omega_2\right)t\right]\right.\\
&\left.-ig_1^*g_2\left(\frac{1}{\delta\omega_1}-\frac{1}{\delta\omega_2}\right)\exp\left(2i\omega_p t\right)\exp\left[i\left(\delta\omega_1+\delta\omega_2\right)t\right]\right\}\tilde{\hat{a}}\tilde{\hat{a}}^\dagger
\end{aligned}
\tag{4.13}
$$

These calculations are useful because they will enable us to calculate (the time derivative of) the variance. Consider the variance in the quadrature we are looking for:

$$
\begin{aligned}
\frac{d}{dt}\langle\Delta\hat{Q}^2\rangle &= \frac{d}{dt}\left(\langle\hat{Q}^2\rangle-\langle\hat{Q}\rangle^2\right)\\
&= \frac{d}{dt}\langle\hat{Q}^2\rangle-\frac{d}{dt}\left(\langle\hat{Q}\rangle^2\right)\\
&= \frac{d}{dt}\langle\hat{Q}^2\rangle-2\langle\hat{Q}\rangle\frac{d\langle\hat{Q}\rangle}{dt}\\
&= \left\langle\frac{d\left(\hat{Q}^2\right)}{dt}\right\rangle-2\langle\hat{Q}\rangle\left\langle\frac{d\hat{Q}}{dt}\right\rangle
\end{aligned}
\tag{4.14}
$$

We now consider a vacuum state. In such a state,

$$
\langle\hat{Q}\rangle=\langle 0|\hat{Q}|0\rangle=\langle 0|\left(\hat{a}+\hat{a}^\dagger\right)|0\rangle=0 \tag{4.15}
$$

therefore the second term in the $d\langle\Delta\hat{Q}^2\rangle/dt$ expression above vanishes, and we have

$$\frac{d}{dt}\left\langle \Delta\hat{Q}^2\right\rangle = \left\langle \frac{d\left(\hat{Q}^2\right)}{dt}\right\rangle \tag{4.16}$$

Using our expression in Eq. (4.13) and considering that, since this is a vacuum expectation value, only the term proportional to $\tilde{\hat{a}}\,\tilde{\hat{a}}^{\dagger}$ will contribute, we get

$$\begin{aligned}\frac{d}{dt}\left\langle \Delta\hat{Q}^2\right\rangle = ig_1g_2^*\left(\frac{1}{\delta\omega_1}-\frac{1}{\delta\omega_2}\right)\exp\left[-i\left(\omega_{c1}+\omega_{c2}+\Delta_1+\Delta_2\right)t\right]\\ -ig_1^*g_2\left(\frac{1}{\delta\omega_1}-\frac{1}{\delta\omega_2}\right)\exp\left[i\left(\omega_{c1}+\omega_{c2}+\Delta_1+\Delta_2\right)t\right]\end{aligned} \tag{4.17}$$

this is easily integrated to give

$$\begin{aligned}\left\langle \Delta\hat{Q}^2\right\rangle = -\frac{1}{\left(\omega_{c1}+\omega_{c2}+\Delta_1+\Delta_2\right)}\left(\frac{1}{\delta\omega_1}-\frac{1}{\delta\omega_2}\right)\left(g_1^*g_2\exp\left[i\left(\omega_{c1}+\omega_{c2}+\Delta_1+\Delta_2\right)t\right]\right.\\ \left.+g_1g_2^*\exp\left[-i\left(\omega_{c1}+\omega_{c2}+\Delta_1+\Delta_2\right)t\right]\right)\end{aligned} \tag{4.18}$$

and this is our final result for the quadrature squeezing in the $\hat{Q}$ coordinate. This was done under the assumption of slowly varying $\hat{a}$ and $\hat{a}^{\dagger}$. Note that for real g_1 and g_2, this looks like a cosine. A similar calculation can be done for the $\hat{P}$ quadrature.

4.3.2 Perturbative approach

Here we present a perturbative approach from which we can solve for the wave functions of the system (which are the tensor product of photon number states and atomic states). We first derive the Schrodinger eqautions for this case. The Hamiltonian is given by Eq. (4.3) where $\hat{\sigma}^- = |g\rangle\langle e|$. To solve for the wave functions, choose the "bare-state" basis:

$$|\psi\rangle = \sum_{n=0}^{\infty}\left(c_{g,n}|g,n\rangle + c_{e,n}|e,n\rangle\right) \tag{4.19}$$

the Schrodinger equation is:

$$\partial_t |\psi\rangle = -\frac{i}{\hbar} H |\psi\rangle \tag{4.20}$$

yielding:

$$\begin{aligned}
\sum_{n=0}^{\infty} \left(\partial_t c_{g,n} |g,n\rangle + \partial_t c_{e,n} |e,n\rangle\right) = &-\frac{i}{\hbar} \sum_{n=0}^{\infty} \hbar\omega_p n \left(c_{g,n} |g,n\rangle + c_{e,n} |e,n\rangle\right) \\
&- \frac{i}{\hbar} \hbar\omega_a \sum_{n=0}^{\infty} c_{e,n} |e,n\rangle \\
&+ g_1 \exp\left[-i\left(\omega_{c2} + \Delta_2\right) t\right] \hat{a}^\dagger \hat{\sigma}^- \sum_{n=0}^{\infty} c_{e,n} |e,n\rangle \\
&+ g_2 \exp\left[i\left(\omega_{c1} + \Delta_1\right) t\right] \hat{a} \hat{\sigma}^- \sum_{n=0}^{\infty} c_{e,n} |e,n\rangle \\
&- g_1^* \exp\left[i\left(\omega_{c2} + \Delta_2\right) t\right] \hat{a} \hat{\sigma}^+ \sum_{n=0}^{\infty} c_{g,n} |g,n\rangle \\
&- g_2^* \exp\left[-i\left(\omega_{c1} + \Delta_1\right) t\right] \hat{a}^\dagger \hat{\sigma}^+ \sum_{n=0}^{\infty} c_{g,n} |g,n\rangle
\end{aligned} \tag{4.21}$$

now, notice that:

$$\begin{aligned}
\hat{a}^\dagger \hat{\sigma}^- \left(\sum_{n=0}^{\infty} c_{e,n} |e,n\rangle\right) &= \sum_{n=0}^{\infty} c_{e,n} \sqrt{n+1}\, |g,n+1\rangle \\
&= \sum_{k=1}^{\infty} c_{e,k-1} \sqrt{k}\, |g,k\rangle \\
&= \sum_{n=1}^{\infty} c_{e,n-1} \sqrt{n}\, |g,n\rangle \\
&= \sum_{n=0}^{\infty} c_{e,n-1} \sqrt{n}\, |g,n\rangle
\end{aligned} \tag{4.22}$$

where to get to the last line we added a zero term because of the $\sqrt{n}$ factor. In a similar manner one gets

$$\hat{a} \hat{\sigma}^- \left(\sum_{n=0}^{\infty} c_{e,n} |e,n\rangle\right) = \sum_{n=0}^{\infty} c_{e,n+1} \sqrt{n+1}\, |g,n\rangle \tag{4.23}$$

$$\hat{a}\hat{\sigma}^{+}\left(\sum_{n=0}^{\infty} c_{g,n}\left|g,n\right\rangle\right) = \sum_{n=0}^{\infty} c_{g,n+1}\sqrt{n+1}\left|e,n\right\rangle \tag{4.24}$$

$$\hat{a}^{\dagger}\hat{\sigma}^{+}\left(\sum_{n=0}^{\infty} c_{g,n}\left|g,n\right\rangle\right) = \sum_{n=0}^{\infty} c_{g,n-1}\sqrt{n}\left|e,n\right\rangle \tag{4.25}$$

Therefore we have

$$\begin{aligned}
\sum_{n=0}^{\infty}\left(\partial_t c_{g,n}\left|g,n\right\rangle + \partial_t c_{e,n}\left|e,n\right\rangle\right) = &-i\omega_p \sum_{n=0}^{\infty} n\left(c_{g,n}\left|g,n\right\rangle + c_{e,n}\left|e,n\right\rangle\right) \\
&- i\omega_a \sum_{n=0}^{\infty} c_{e,n}\left|e,n\right\rangle \\
&+ g_1 \exp\left[-i\left(\omega_{c2}+\Delta_2\right)t\right]\sum_{n=0}^{\infty} c_{e,n-1}\sqrt{n}\left|g,n\right\rangle \\
&+ g_2 \exp\left[i\left(\omega_{c1}+\Delta_1\right)t\right]\sum_{n=0}^{\infty} c_{e,n+1}\sqrt{n+1}\left|g,n\right\rangle \\
&- g_1^{*} \exp\left[i\left(\omega_{c2}+\Delta_2\right)t\right]\sum_{n=0}^{\infty} c_{g,n+1}\sqrt{n+1}\left|e,n\right\rangle \\
&- g_2^{*} \exp\left[-i\left(\omega_{c1}+\Delta_1\right)t\right]\sum_{n=0}^{\infty} c_{g,n-1}\sqrt{n}\left|e,n\right\rangle
\end{aligned} \tag{4.26}$$

multiplying this equation by $\langle g,n|$ and then by $\langle e,n|$ (for a specific n), we get the equations for the coefficients:

$$\begin{aligned}
\partial_t c_{g,n} &= -in\omega_p c_{g,n} + g_1 \exp\left[-i\left(\omega_{c2}+\Delta_2\right)t\right]\sqrt{n}c_{e,n-1} \\
&\quad + g_2 \exp\left[i\left(\omega_{c1}+\Delta_1\right)t\right]\sqrt{n+1}c_{e,n+1} \\
\partial_t c_{e,n} &= -in\omega_p c_{e,n} - i\omega_a c_{e,n} - g_1^{*} \exp\left[i\left(\omega_{c2}+\Delta_2\right)t\right]\sqrt{n+1}c_{g,n+1} \\
&\quad - g_2^{*} \exp\left[-i\left(\omega_{c1}+\Delta_1\right)t\right]\sqrt{n}c_{g,n-1}
\end{aligned} \tag{4.27}$$

these can be solved perturbatively by substituting the initial states and getting the next order solutions iteratively by substituting the previous step solutions. An advantage of this method is that we can see the behavior of individual wave-function solutions $c_{g,n}(t)$

and $c_{e,n}(t)$, besides calculating the overall photon statistics. An example code for the case $n = 7$ is shown in Appendix A.2.

4.4 Computer simulations

To evaluate a more general behavior of the system, we ran computer simulations written in Python using the QuTiP package. We used the Hamiltonian in Eqs. (4.1), (4.2). We took the initial wave function of the system to be the tensor product of the atomic state with the photon states, $|\psi\rangle = |\psi_{\text{atom}}\rangle \otimes |\psi_{\text{photon}}\rangle$ (i.e., an initial non-entangled state). For the atomic state, our basis consisted of only two states, $|\psi_{\text{atom}}\rangle = |g\rangle$ or $|e\rangle$, while for the photonic states we work in the photon number basis (Fock states), and keep up to $n = 500$ photons: i.e., $|\psi_{\text{photon}}\rangle = |0\rangle, |1\rangle, \cdots |n = 500\rangle$. We have numerically found this size of Fock space to be large enough in order to accurately show the physical features of the system, while still small enough for the simulation run-time to be feasible. In the simulations we took the atoms to start in the ground state and the photons in a Fock state of zero photons (vacuum). Since the control lasers are much more intense than the probe, the control beams were treated classically, their amplitudes indicate the strength of each resonance (denoted by g_1 and g_2) while the probe beam was treated quantum mechanically using $\hat{a}$ and $\hat{a}^\dagger$ operators. The probe laser frequency ω_p was taken to be an order of magnitude larger than g_1 and g_2. The Hamiltonian and the initial state of the system give all the necessary information in order to evaluate any desired quantum expectation values (QEV). With the definitions $\hat{Q} = \hat{a} + \hat{a}^\dagger$ and $\hat{P} = i(\hat{a}^\dagger - \hat{a})$, we evaluated the statistical quantities representing quadrature squeezed states $\langle \Delta\hat{Q}^2\rangle$ and $\langle \Delta\hat{P}^2\rangle$ and photon-number squeezed states based on the quantities $\langle \hat{n}\rangle$ and $\langle(\Delta\hat{n})^2\rangle$ where $\hat{n} = a^\dagger\hat{a}$, as well as the atomic excitation probability based on the operators $\hat{\sigma}$ and $\hat{\sigma}^\dagger$. We looked at two types of simulations: For the ideal case where loss of photons or decay of atoms, denoted by γ and κ, were negligible $(\gamma, \kappa \ll g_1^2, g_2^2)$ we solved the Schrodinger equation numerically:

$$i\hbar\frac{d|\psi\rangle}{dt} = \hat{H}|\psi\rangle \quad . \tag{4.28}$$

to then calculate the relevant QEV. For the case taking into account atomic or photonic decay processes, we calculated the density matrix of the system, solved the master equation (see Eq. 4.31) for the density matrix numerically, and evaluated the relevant QEV $\langle A(t)\rangle$ using

$$\frac{d}{dt}\langle A(t)\rangle = \mathrm{Tr}\left(\frac{d}{dt}\rho(t)A(t)\right) \tag{4.29}$$

The numerical evaluation of the time-dependent QEV using the master equation required a lot of resources (unlike the Schrodinger equation). To run time-intensive simulations we used the computing cluster at the Center for High Throughput Computing (CHTC) at UW-Madison.

4.4.1 Single atom simulations, photon-number statistics

In these simulations, we consider a single atom initially in the ground state, subject to the strong control lasers and the weak probe laser. The initial conditions for the probe laser were set to a zero photon Fock state (vacuum). We looked at the dynamics as a function of time. Here we discuss a couple of representative examples. In Figure 4.2a, the left image shows the photon statistics with the chosen parameters $g_1 = 0.25$, $g_2 = 1.0$ (arbitrary units), where the resonances are far enough apart. Here, the resonance involving control laser 1 and the probe beam is stronger than the resonance with control beam 2 and the probe beam. The plot is semi-periodic, and remarkably, shows finite time intervals where the probe photons have sub-Poissonian statistics ($\Delta\hat{n}^2 < \bar{\hat{n}}$), as the result of the two-resonance interference. The right image shows the excitation probability of the atom, which looks like Jaynes-Cummings oscillations of a single resonance. This makes sense as in this case one of the resonances dominates the other. The numerical simulations reveal that the photon-number squeezing effect is strongest in this type of a system where one resonance is stronger than the other, but the weaker resonance is not negligible. In the next figures we consider the behavior when the resonances are closer together. In Figure 4.2b, the pattern of atomic probability oscillations is somewhat distorted relative to those in Figure 4.2a as both resonances contribute. The photon statistics in this case show an oscillatory behavior with an increase in the average number of photons as a function of time. This is because when the two resonances become comparable in strength, the usual oscillatory dynamic is perturbed, with the photon field finding additional pathways for amplification. In addition, compared with the case of far separated resonances, here the interference increases the noise Δn^2 to be large compared with the average photon number $\bar{n}$, resulting in super-Poissonian statistics. Finally, Figure 4.2c shows the situation when the two resonances are of equal strength: $g_1 = g_2 = 1.0$. There is large amplification of the photon field resulting in an increased average number of photons, while the light maintains a nearly Poissonian statistics. The atomic transition probabilities change from the initial state and stabilize at nearly 0.5 in this case of equal-strength resonances.

We therefore conclude that photon-number squeezed states appear (for finite times) in the case where one resonance is stronger than the other, but are ruined as the interference of the two resonances increases. The full set of results for a single and for multiple atoms without decay, as we discussed here, as well as the cases including decay, appear in Appendix B.

4.4.2 Single atom simulations, quadrature squeezing

In this section we look at quadrature squeezing in the system from the interference of the two resonances. As representative examples, we look at Figure 4.3. We denote the two quadratures as $\hat{Q} = \hat{a} + \hat{a}^\dagger$ and $\hat{P} = i(\hat{a}^\dagger - \hat{a})$, which imply that a squeezed quadrature has a variance less than 1. In these plots, the fast oscillations are apparent. From the definitions, since $\Delta\hat{Q}^2$ (and also $\Delta\hat{P}^2$) are proportional to the squares of $\hat{a}$ and $\hat{a}^\dagger$, the oscillations are at twice the probe frequency. Figure 4.3a shows the quadrature oscillations for the parameters $g_1 = 1.0$ and $g_2 = 2.0$ (arbitrary units) while Figure 4.3b shows the quadrature oscillations for $g_1 = 2.0$ and $g_1 = 1.0$. the maximum squeezing of

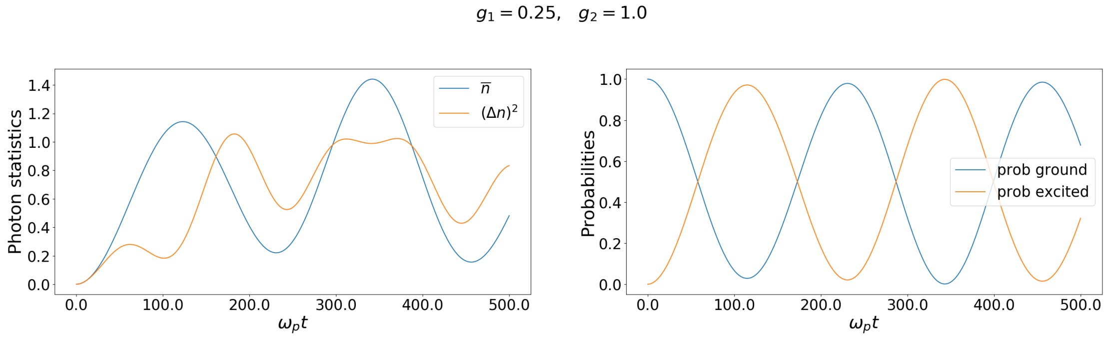

(a)

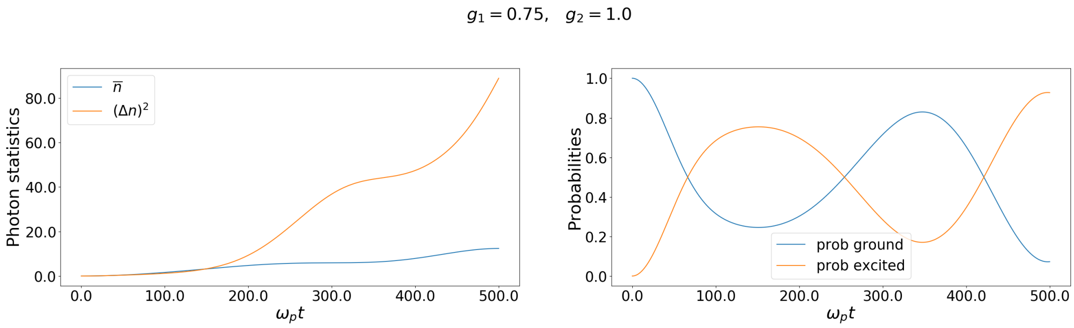

(b)

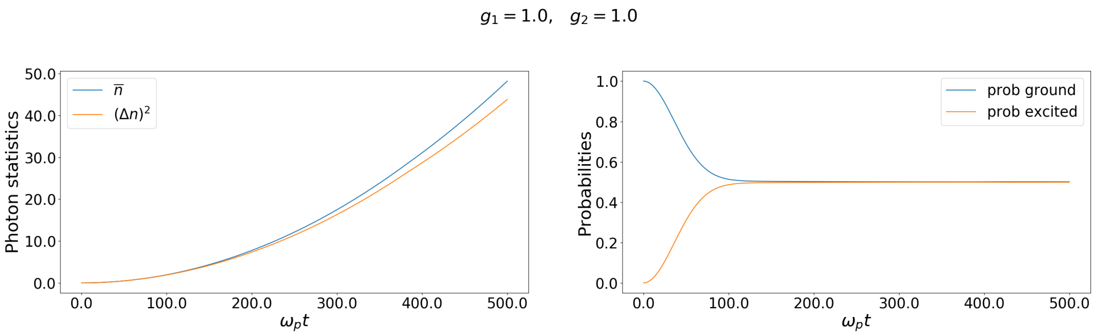

(c)

Figure 4.2: Photon statistics of a probe beam in a system with two interfering resonances, for the case of a single atom. The parameters g_1 and g_2 represent the strength of each resonance. Photon number squeezing occurs when $(\Delta n)^2 < \bar{n}$. In Figure 4.2a the resonances are far apart and are dominated by g_2. The atomic level transitions show Jaynes-Cummings oscillations due to g_2 resonance, while the photon number oscillations result in photon-number squeezing. In Figure 4.2b the coupling strengths are closer together. While the number of photons increases, the variance Δn^2 increases faster and no photon-number squeezing is observed. In Figure 4.2c the photon statistics is almost Poissonian, while the transition probability flattens quickly to 0.5.

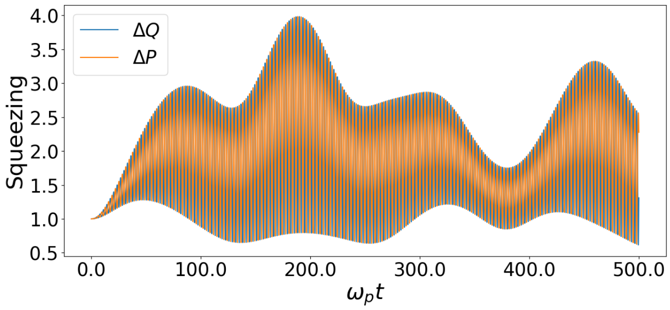

(a)

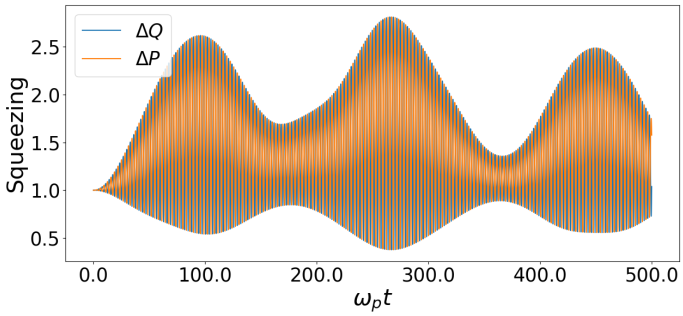

(b)

Figure 4.3: Quadrature oscillations for a refractive index enhancing two-resonance system. The amount of quadrature squeezing achieved depends on the resonance strengths as well as on the initial conditions. The top figure corresponds to the resonance strengths $g_1 = 1.0$ and $g_2 = 2.0$ (arbitrary units), while the bottom figure corresponds to $g_1 = 2.0$ and $g_1 = 1.0$. These two cases correspond to an optimal choice of parameters, and achieve a maximum squeezing of $\sim 6\,\mathrm{dB}$.

each quadrature is almost 0.5 ($-6\,\mathrm{dB}$) which is significant. The maximum amount of squeezing depends on both the strength of the resonances and the initial conditions. A full list of results corresponding to different system parameters appears in Appendix B. It turns out that maximum squeezing appears for g_1 and g_2 being close enough. If they are too far apart, not much interference happens, which is responsible for the nonlinear effect which creates the quadrature squeezed state. If $g_1 \approx g_2$, the two resonances interfere destructively and appear to weaken one another, and quadrature squeezing is not observed.

4.4.3 Multiple Atoms

Here we look at simulation results with up to 10 atoms and see which features of a single atom remain in this case. The Hamiltonian of a system of n atoms is:

$$\begin{aligned}\hat{H} = \hbar\omega_p \hat{a}^\dagger \hat{a} + \hbar\omega_a \sum_{i=0}^{n} \hat{\sigma}_i^\dagger \hat{\sigma}_i \\ + i\hbar g_1 \exp\left[-i\left(\omega_{c2} + \Delta_2\right)t\right] \hat{a}^\dagger \sum_{i=0}^{n} \hat{\sigma}_i^- + i\hbar g_2 \exp\left[i\left(\omega_{c1} + \Delta_1\right)t\right] \hat{a} \sum_{i=0}^{n} \hat{\sigma_i}^- + \text{c.c}\end{aligned} \tag{4.30}$$

We ran the simulations for different parameters and compared the result to the single-atom case. The full results appear in Appendix B. Here we examine one example, for $g_1 = 0.5$ and $g_2 = 1.0$. It is apparent that a single atom has both photon-number squeezing and quadrature squeezing for these parameters. Unfortunately, this squeezing is destroyed in the case of more than a single atom. This is the case for other resonance parameters as well. The noise Δn increases relative to $\bar{n}$ when the number of atoms is increased, which makes sense. The transition probability oscillations get distorted due to the effect of multiple atoms. The quadratures, having been close to 0.5 for optimal parameters in a single atom, do shift to values larger than 1 as a function of time for multiple atoms, showing that there is more "noise". This shows that this experiment should be ideally done using a single atom. Simulating up to 10 atoms, all interacting with a Fock space of up to 500 photons, had been a demanding task that required the use of a computer cluster at UW-Madison for multi-atom systems.

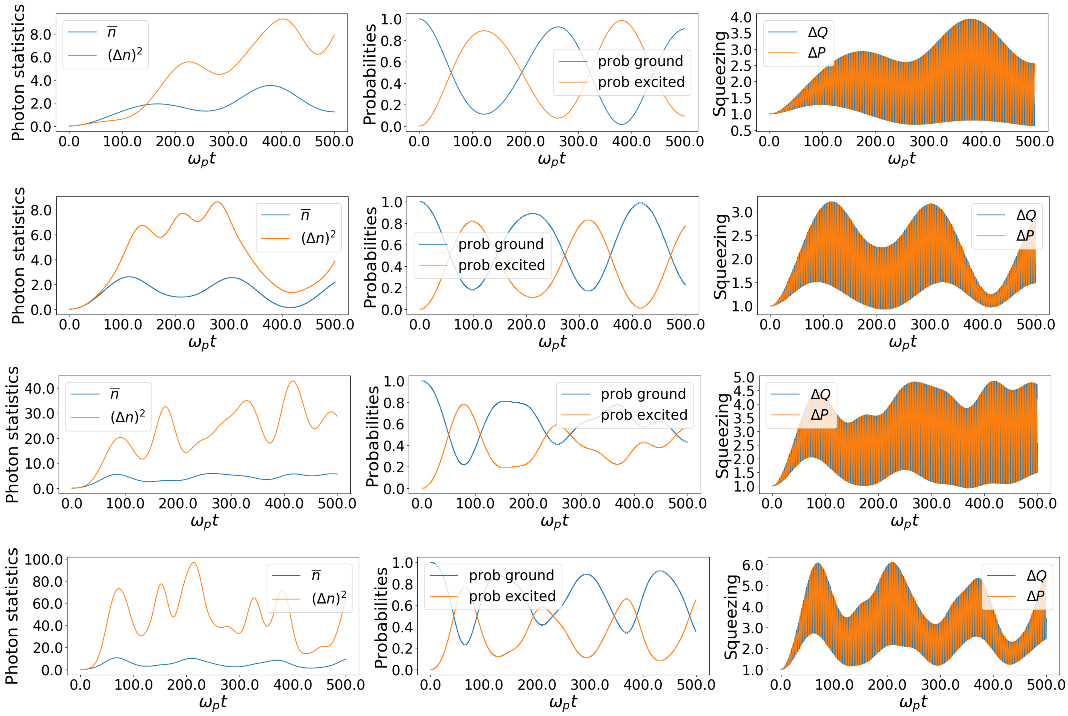

Figure 4.4: Quadrature and photon-number squeezing in the case of multiple atoms, for $g_1 = 0.5$, $g_2 = 1.0$. The top figures show the results for a single atom, the second line figures show for $N = 2$ atoms, the third line figures show the $N = 5$ atoms case, and the bottom figures are for $N = 10$ atoms. The squeezing that appears for a single atom is destroyed, although the general time dependence behavior doesn't change dramatically.

4.5 Detuning

Here we look at the effect of the detuning of each transition from resonance, on the amount of quadrature squeezing. We denote by Δ_1 and Δ_2 the detunings for transitions involving control laser c_1 and c_2, respectively. We varied Δ_1 and Δ_2 between -4.0 and 4.0 (in the arbitrary units of the simulations. This is up to about 10% of the energy transition frequencies of the order of ω_{c1}, ω_{c2} and ω_p). For each choice of (Δ_1, Δ_2) we ran the simulation for a time $t = 500/\omega_p$ and recorded the minimum value of $\langle \Delta \hat{Q}^2 \rangle$ and $\langle \Delta \hat{P}^2 \rangle$ (which corresponds to the maximum amount of quadrature squeezing). The results are reported in dB. Figure 4.5 shows an example plot for $g_1 = 1.0$ and $g_3 = 3.0$. It is apparent that the maximum squeezing is obtained not right at $\Delta_1 = \Delta_2 = 0$ but at a finite detuning, which is nontrivial and interesting. Results for different choices of resonance strengths g_1 and g_2 gave different optimal (Δ_1, Δ_2), and unfortunately we

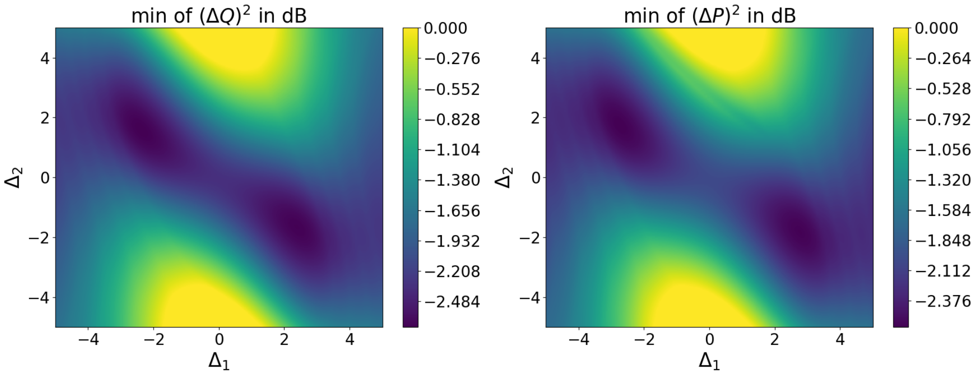

Figure 4.5: Contour plot of the minimum of ΔQ^2 quadrant (measured from a simulation running up to $t = 500/\omega_p$) as a function of the detuning of the control lasers from resonance. The maximum amount of squeezing does not occur for $\Delta_1 = \Delta_2 = 0$.

have not determined a definite pattern. Remarkably, even though the time-dependance of each quadrature (for a specific choice of Δ_1 and Δ_2) is different, the minimum values as a function of detuning are very similar between the $\hat{Q}$ and $\hat{P}$ quadratures, and the two contour plots resemble one another.

4.6 Decay

Here we take into account decay of atoms and photons, which was neglected in the previous simulations. To represent them, we include the collapse operator $\sqrt{\kappa}\hat{a}$ for photonic decay and $\sqrt{\gamma}\hat{\sigma}$ for atomic decay, where the decay coefficients κ and γ range from 0.0 to 1.0, of the order of the resonance strength parameters (g_1, g_2), and observe the effects on the quadrature squeezing. We chose a couple of parameter values of (g_1, g_2) that corresponded to strong quadrature squeezing in single atom simulations before decay was considered. To correctly take into account the interaction with the environment present in the system through the decay terms, a master equation should be considered rather than the Schrodinger equation. The master equation for our system is:

$$\begin{aligned}\dot{\rho}(t) = -\frac{i}{\hbar}[H(t), \rho(t)] + \frac{1}{2}\kappa \left(2a\rho(t)a^\dagger - \rho(t)a^\dagger a - a^\dagger a\rho(t)\right) \\ + \frac{1}{2}\gamma \left(2\sigma\rho(t)\sigma^\dagger - \rho(t)\sigma^\dagger\sigma - \sigma\sigma^\dagger\rho(t)\right)\end{aligned} \tag{4.31}$$

where $\rho(t)$ is the density matrix, $H(t)$ is the Hamiltonian of the system, the second term is due to the photons loss in the cavity, and the third term is due to atomic decay. This master equation can be solved for $\rho(t)$. Then, using this solution, different expectation values can be found, i.e. the expectation value of a quantum operator A can be calculated from:

$$\frac{d}{dt}\langle A(t)\rangle = \mathrm{Tr}\left(\frac{d}{dt}\rho(t)A(t)\right) \tag{4.32}$$

The computer simulations solved this equation numerically using the QuTiP package. Using this enabled us to find the expectation values of the quadratures as a function of time, $\langle\Delta\hat{Q}\rangle$ and $\langle\Delta\hat{P}\rangle$. We are interested in the maximum amount of squeezing achievable under these conditions. The results in Figure 4.6 show the minimum value of the quadratures as a function of the decay parameters.

We see that loss of photons according to the $\sqrt{\kappa}\hat{a}$ model does not ruin the squeezing in the case of $(g_1, g_2) = (1.0, 2.0)$ and $(g_1, g_2) = (1.0, 5.0)$, while atomic decay does ruin it when it is too strong. The case $(g_1, g_2) = (2.0, 1.0)$ is interesting, since the effect of photon losses seems stronger in this case than atomic decay. Also, the overall squeezing amount is higher than in the other two cases (with a minimum of ΔQ being 8 dB) such that the squeezing is not ruined even for κ and γ being 1.0. This shows that the decay effect on the amount of squeezing depends strongly on the resonance parameters.

4.7 Conclusions

We have analyzed a system for refraction index enhancement, and found, using numerical simulations, that under certain choices of the system parameters (such as the resonance strength, the detuning from resonance and the decay parameters) squeezed states were created. This suggests a new and interesting way to produce quadrature squeezed or photon-number squeezed light as the case may be, without including an explicit nonlinearity in the system. Besides the interesting physics, this might have potential applications as a refractive-index enhancement setup having lower noise in a

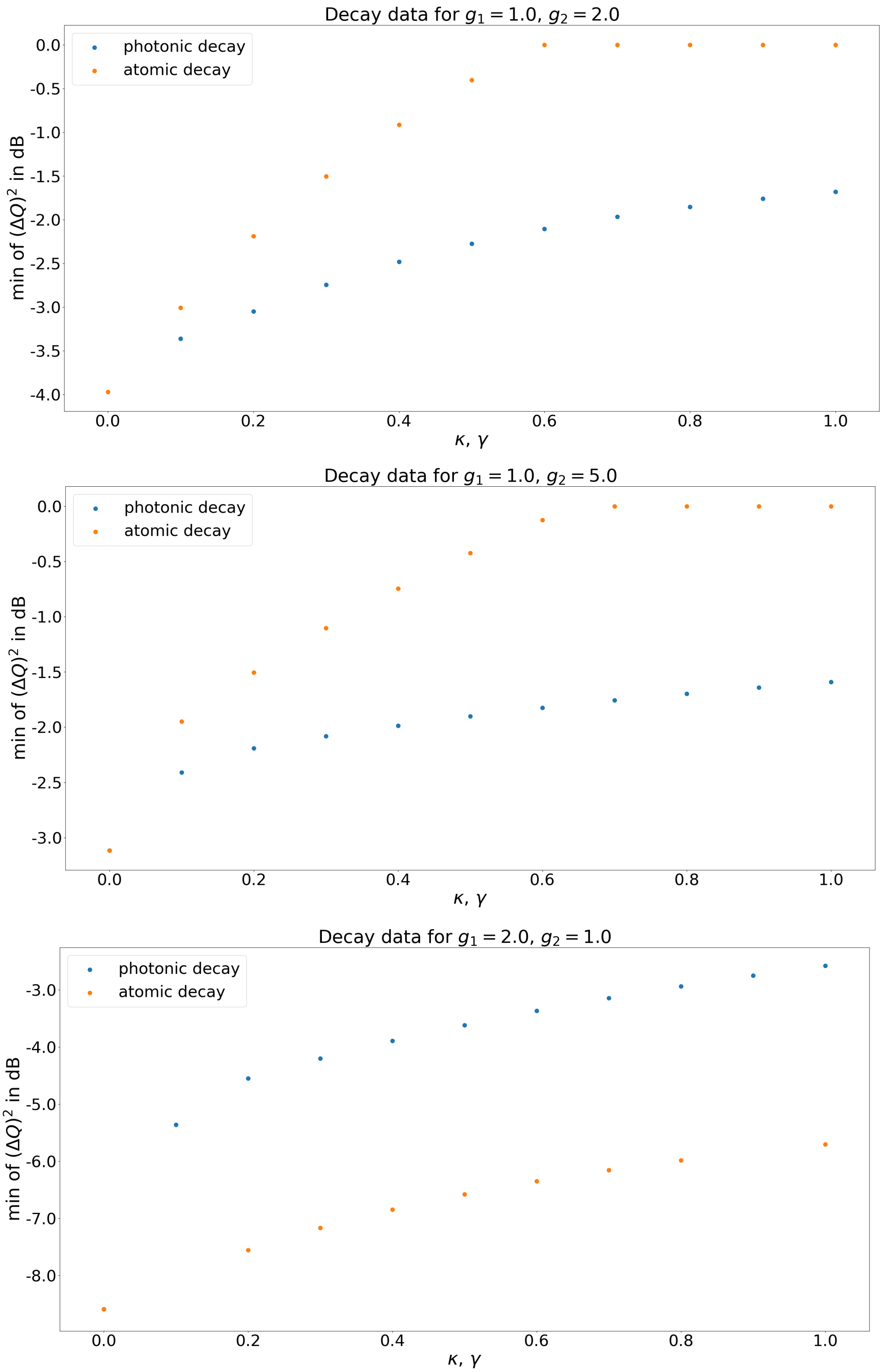

Figure 4.6: Minimum quadrature squeezing as a function of decay coefficients. In the top two figures the atomic decays have a larger effect than photon losses, and become strong enough for large decays to destroy the squeezing. In the last figure, photon losses have a stronger effect but the squeezing is larger and is not destroyed.

specific quadrature of the probe laser.

Part II

Detection of axions in guided structures

Chapter 5

Motivation - dark matter and axions

According to the current standard model of cosmology, the “concordance cosmological model”, the energy density in the universe today is composed of roughly 68% dark energy, 32% matter, and a negligible amount of radiation (initially the radiation density dominated, but decreased quickly as the universe expanded). In the matter sector, about 27% is dark matter, while only 5% is ordinary (baryonic) matter, see Figure 5.1. So in a sense, we are familiar with only 5% of the universe!

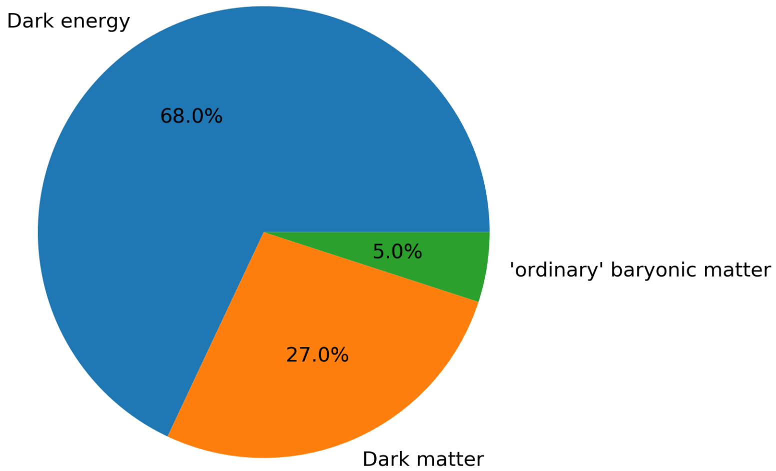

Figure 5.1: Energy density components of the universe today, according to the ΛCDM (“concordance”) model.

To understand the effect of dark energy, let us look at Einstein’s general theory of relativity (GR). According to it, energy sources curve spacetime and particles move through this curved spacetime. The second Friedmann equation, which is based on

Einstein's GR equation in a homogeneous and isotropic universe, reads

$$\frac{\ddot{a}}{a} = -\frac{4\pi G}{3}\left(\rho + \frac{3P}{c^2}\right) \tag{5.1}$$

where a is the cosmological scale factor, ρ is the energy density and P is the pressure. The different components in the Universe (nonrelativistic matter, radiation, dark energy) have equations of state $P = w\rho c^2$ where w characterizes that component. For matter $w = 0$ and for radiation $w = 1/3$. In both cases the term in parentheses is positive, making objects attract each other. For dark energy, however, $w < -1/3$ which makes the parentheses negative, and results in a repulsion "force". Therefore dark energy repels, and is in fact responsible for the current accelerating expansion rate of the universe. The nature of dark energy and dark matter is both unknown. Dark energy behaves like vacuum energy under cosmological expansion. However, calculations from quantum field theory show a discrepancy of 60 orders of magnitude between the two! [23]. In the next sections we will focus on dark matter. We will explore observations that give evidence of dark matter and suggest possible candidates to what dark matter actually is. We will then review the axion as a prominent dark matter candidate, and as the solution to the strong CP problem in particle physics.

5.1 Evidence of dark matter

Dark matter, as its name implies, cannot be "seen" directly through observations of radiation from stellar sources. Its existence is, however, confirmed by its gravitational effects on matter and radiation. In the next sections we will explore different evidence for the existence of dark matter.

5.1.1 Galaxy clusters

If one examines all the observed radiating matter in a galaxy cluster, it looks like there is far more gravitational matter than is revealed by its observed radiation. Its gravitational attraction is not enough to hold the cluster and the hot gas together, and the cluster is expected to "fly apart" considering its constituents velocities. The fact that it is held together means that there is more matter than we account for by observing the radiation, another form of matter that does not radiate (which is hence termed "dark matter"). To approximate the mass of all matter (including the dark matter) we can use the virial theorem, which is valid for systems at gravitational equilibrium, which are not evolving anymore. The virial theorem says

$$2\langle K\rangle + \langle U\rangle = 0 \tag{5.2}$$

$$\therefore \langle K\rangle = -\frac{\langle U\rangle}{2} \tag{5.3}$$

where K is the kinetic energy of the cluster and U is the gravitational potential energy. The following calculation is based on [24]. The virial theorem for this system can be written as

$$\frac{1}{2}M\langle v^2\rangle = \frac{\alpha G M^2}{2r_h} \tag{5.4}$$

where α is a numerical factor for the system and r_h is the half-mass radius, i.e. the radius at which half the mass is contained inside. The first evidence of dark matter was provided by the Swiss astronomer Fritz Zwicky during the 1930's. He was observing the Coma cluster of galaxies. Let us use the virial theorem to approximate the mass of that cluster and the amount of dark matter inside. For the Coma cluster, $\alpha = 0.4$. r_h can be calculated from the half light radius and is $r_h \approx 1.5\,\text{Mpc} \approx 4.6\times 10^{22}\,\text{m}$, and $\langle v^2\rangle$ can be calculated from the radial velocity (based on the Doppler shift of the spectral lines) and the velocity dispersion (the width of the Doppler line) and is $\langle v^2\rangle = 2.32\times 10^{12}\,\text{m}^2/\text{s}^2$. Putting all of this together, one obtains

$$M_{\text{Coma}} = \frac{\langle v^2\rangle r_h}{\alpha G} \approx 2\times 10^{15} M_\odot \tag{5.5}$$

where $M_\odot$ is one solar mass. Comparing this to the mass of baryonic components of the Coma cluster based on the observed emitted radiation, $M_{\text{Coma,stars}} \approx 3 \times 10^{13}\, M_{\odot}$ and $M_{\text{Coma,gas}} \approx 2 \times 10^{14}\, M_{\odot}$, the total mass of luminous matter is only about 12% of the total mass. Therefore the majority of the mass is dark matter! A similar situation exists in other galaxy clusters.

5.1.2 Galactic rotation curve

It is known that spiral galaxies are made of a bulge at the center, and a thin disk containing stars and gas. If we observe stars or gas particles in a spiral galaxy and record their velocities, we can plot their velocity as a function of their distance from the galactic center. This is called a rotation curve. Suppose a star of mass m rotates at a radius R from the center. Then the force of gravity acting on it is due to the mass inside the radius R, $M(R)$, and is equal to the centripetal force:

$$\frac{GM(R)m}{R^2} = \frac{mv^2}{R} \tag{5.6}$$

$$\therefore \quad v = \sqrt{\frac{GM(R)}{R}} \tag{5.7}$$

If we expect most of the luminous matter to be close to the center at a roughly constant density, the mass would grow with radius as $M \propto R^3$. This yields $v \propto R$. On the other hand, at larger radii, we expect the mass to stop growing and be constant, since almost all the mass would be inside the radius R. Therefore we would get $v \propto 1/\sqrt{R}$. This is known as a Keplerian curve, since in our solar system the planets follow this curve in their motion around the Sun, with almost all the mass of the solar system being contained in the Sun. This type of rotation curve measurement was accurately carried out by the astronomers Vera Rubin and Kent Ford in 1970. By measuring the rotation curve of hot gas in M31 (Andromeda) galaxy, they found that while it increased linearly at small radii in the bulge, out at larger radii it stayed flat(!) instead of decreasing as $1/\sqrt{R}$. The luminosity in the galactic disk decreases according to $I = I_0 e^{-R/R_s}$ where R_s is a typical scale of a few kiloparsecs. For M31, $R_s \approx 6\,\text{kpc}$. Rubin and Ford measured the velocity curve up to $R \lesssim 4R_s$, and a couple of years later another team measured it up to $R \approx 5R_s$. Therefore the situation is a decreasing amount of luminous matter at high radii, but steady amount of mass based on gravitational effects. Therefore there must be nonluminous matter at large radii, i.e. this provides evidence for the existing of dark matter inside galaxies. Also, without this additional dark matter mass, the stars / gas would fly apart and not stay gravitationally bound at these velocities.

5.1.3 CMB anisotropies

Lastly, dark matter can be measured from the anisotropies in the cosmic microwave background radiation (CMB). In the early universe, after inflation took place, the universe consisted of a hot plasma of photons and baryons, undergoing acoustic oscillations. The dark matter (which constitutes most of the mass) did not participate in the oscillations but constituted the gravitational potential well for these oscillations. These oscillations continued until the recombination phase, where the electrons combined with protons to form atoms, and the photons became decoupled from the plasma and were released as the CMB. Then the acoustic wave 'froze' and its imprints exist in the largely isotropic CMB spectrum. The existing shape of the measured power spectrum of the isotropies necessitates dark matter, hence providing evidence for its existence, and by measuring the height and spacing of the acoustic peaks it is possible to calculate the ratio of dark to baryonic matter densities.

5.2 Dark Matter candidates

Since dark matter had not been detected yet, the possibilities of what it could be are vast. Different candidates had been suggested with masses as little as fractions of eV for particles such as the axions to as large as several stellar masses for MACHO (see below). Let us consider the different types of major candidates and the current knowledge regarding them, starting with baryonic matter and moving to nonbaryonic (and yet hypothetical) options.

5.2.1 Neutrinos

Neutrinos are one of the first dark matter (DM) candidates coming to mind: For once, they are particles we know to exist. They are interacting very weakly with the Standard Model (SM) particles, only through the weak interaction (and no electromagnetic interaction means they are 'dark'). Thermodynamic calculations in the early universe lead to the number density ratio of neutrinos and photons today [24] $n_\nu = (3/11)n_\gamma$. This gives

$$\Omega_\nu = \frac{\rho_\nu}{\rho_c} = \frac{(\sum m_\nu c^2)n_\nu}{\rho_c} = \frac{(\sum m_\nu c^2)\left(\frac{3}{11}\right)n_\gamma}{\rho_c} \tag{5.8}$$

and taking the number density of CMB photons today as $n_\gamma = 412\,\mathrm{cm}^{-3}$ and the critical density of the universe today as $\rho_c = 5200\,\mathrm{eV/cm}^3$ we get

$$\Omega_{\nu,0} = \frac{(\sum m_\nu c^2)\left(\frac{3}{11}\right)412\ \mathrm{cm}^{-3}}{5200\,\mathrm{eV\,cm}^{-3}} = \frac{\sum m_\nu c^2}{47\,\mathrm{eV}} \tag{5.9}$$

where $\Omega_{\nu,0}$ is the ratio of the neutrino energy density to the critical energy density at the current time. Let us consider some data regarding the sum of neutrino masses, to see if they can make most of the dark matter. Lab experiments set an upper limit of $\sum m_\nu c^2 \lesssim 7.5\,\mathrm{eV}$ but cosmology sets a more stringent bound. The exact cosmology bounds based on CMB measurements vary between experiments [25] and although there had been more strict recent results, let us assume the conservative higher bound of $\sum m_\nu c^2 \lesssim 0.68\,\mathrm{eV}$. Neutrino oscillation experiments give on the other hand [26] $\sum m_\nu c^2 \gtrsim 50\,\mathrm{meV}$. Therefore we have the bounds $0.00106 < \Omega_{\nu,0} < 0.00144$. Comparing this to the dark matter density

$$\Omega_{\mathrm{dm},0} = 0.26 \tag{5.10}$$

puts the neutrino between $0.4\% - 5.6\%$ of dark matter even with the more relaxed bounds we chose. This means that only a small (though not insignificant!) fraction of dark matter is in the form of baryonic SM neutrinos. In addition to this, the small neutrino mass described above also implies that neutrinos had been ‘hot’ at their time of decoupling, moving at relativistic speeds. If they constituted most of dark matter, this would have prevented structure formation later on since neutrinos would fly away instead of providing steady gravitational wells for density fluctuations to grow and structure formation to happen.

5.2.2 MACHO

Another natural baryonic option to consider is stellar objects. The first ones coming to mind are stars and interstellar gas but they are obviously not good candidates since they emit light. Interstellar dust also re-emits radiation in the IR range. We are then left with dim objects inside the galactic halo (the term MACHO stands for Massive Compact Halo Objects). These include stellar remnants such as black holes and neutron stars, and dim stars such as red and brown dwarfs. Stellar remnants are less plausible because they arise from main sequence stars, and since there are not many stars inside the halo, we don't expect a lot of stellar remnants there either. Other options are M-stars (“red dwarfs”, dim stars with $M \lesssim 0.1M_{\odot}$) and brown dwarfs (even dimmer, with $M \lesssim 0.08M_{\odot}$ which are not massive enough to ignite hydrogen and shine only from residual energy due to gravitational contraction). These are the best MACHO candidates (and are also the most common stars in the galactic disk). As these objects are dim and we cannot see them directly, a technique called ‘microlensing’ is used in experiments, such as MACHO or EROS, in order to observe them. The technique relies on the fact that if we observe starlight coming from a distant source, and the light beam passes near a MACHO, the light beam will bend due to gravity from the stellar object, so the object essentially functions as a gravitational lens for these beams. As a result, the star light intensity will be amplified, having a distinct curve as a function of time, which allows to distinguish it from other events. These types of observations had been made on stars in the Large Magellanic Cloud (LMC), a small satellite galaxy of the Milky Way, about 50 kpc away. The LMC is a good choice for light sources since it has enough bright stars, it is far enough away so that the line of sight intersects a significant fraction of the galactic halo, and it is far enough above the galactic plane so that one actually cuts through the halo, not just through the galactic disk [27]. One problem is that the optical depth for microlensing stars in the LMC is $\sim 10^{-6}$. Therefore, if one observes 10^6 stars, one has a good chance of seeing a single microlensing event. Lots of measurements are therefore required. Such observations had been made for millions of stars over the past 3 decades, with the use of computerized search techniques. Results from EROS-2 and MACHO put an upper limit of $\sim 15\%$ of compact halo objects in the mass range $10^{-6} - 10^2 M_\odot$ [28]. In addition, the Hubble Space Telescope constrained the population of M-stars in the galactic halo to less than 6% [29]. Thus, MACHO are not the dominant form of dark matter in the galactic halo.

5.2.3 WIMP

From the sections above it is evident that baryonic matter does not constitute the majority of dark matter in the universe, therefore we must look at nonbaryonic (hypothetical as of yet) options. One category is WIMP, or Weakly Interacting Massive Particles, potential cold dark matter (CDM), having a large mass and interacting only weakly with standard model (SM) particles. One option is provided by a minimal extension of the SM which introduces an additional two Higgs scalar doublet having a discrete symmetry. This neutral scalar or pseudoscalar boson particle does not couple directly to SM fermions or to photons, and would be stable due to the discrete symmetry of the model [30] and therefore would not decay through the evolution of the universe. Because of these features it would be an excellent dark matter candidate. Its predicted mass range is 54-74 GeV [31].

Another possibility is a heavy neutrino. We are familiar with 3 generations of neutrinos, which are part of the SM. LEP experiment showed that there are exactly 3 generations of light neutrinos. A fourth generation is possible, however - it would need to have a mass $m > m_Z/2 \approx 46\,\mathrm{GeV/c^2}$ in order to not have been discovered yet. With such a heavy mass, we do not expect a large number of such particles to have been created in the Big Bang, and therefore, whether such a heavy neutrino exists or not, it would not explain the majority of dark matter.

Finally, popular options come from Supersymmetry (SUSY). SUSY theories predict that every particle in the SM has a supersymmetric partner, such that every fermion has a bosonic partner (names begin with 's' for 'supersymmetric', such as selectron, smuon etc.) and every boson has a supersymmetric fermionic partner (photino, Higgsino, Zino, etc.) A new quantum number, the R parity (+1 or -1), distinguishes SM particles from their SUSY partners. If the R parity is conserved (such as the case in the simplest SUSY theories) then the lightest supersymmetric particle (LSP) must be stable, since it cannot decay to other heavier SUSY particles, and decay modes to SM particles would violate conservation of R parity. Such a stable, weakly interacting particle is an attractive option to be dark matter. However, negative experimental results from CERN and other laboratories appear to rule out the minimal supersymmetric model as cold dark matter. Heavier non-minimally supersymmetric particles are still possible, though are less likely.

5.2.4 Axions

Axions belong in the category of WISP (Weakly Interacting Slim Particles). The axion is a very light pseudoscalar particle (spin-parity 0^-) that was originally postulated in order to solve the "strong CP problem" in particle physics. The problem arises as follows. The quantum chromodynamics (QCD) Lagrangian includes the term [32]:

$$\mathcal{L} = -\bar{\Theta}(\alpha_s/8\pi)G^{\mu\nu a}\tilde{G}^a_{\mu\nu} \tag{5.11}$$

where Θ is a dimensionless parameter, $\bar{\Theta}$ is the effective parameter after diagonalizing quark masses, $G^a_{\mu\nu}$ is the color field strength tensor and $\tilde{G}^{a,\mu\nu}$ is its dual. This term is not symmetric under CP transformation (which is a transformation under the combined C (charge conjugation) and P (parity)). Based on this Lagrangian, the electric dipole moment can be calculated and is equal to

$$d_n \approx 10^{-15}\,\bar{\Theta} \tag{5.12}$$

Naively there is no reason why the $\bar{\Theta}$ parameter should not be of $\mathcal{O}(1)$. However, current experimental bounds are found to be $d_n < 10^{-26}\,\mathrm{e}\cdot\mathrm{cm}$ [33]. Comparing this to Eq. (5.12) leads to the constraint $\left|\bar{\Theta}\right| < 10^{-11}$, making this CP-violating term essentially vanish, and the whole Lagrangian symmetric under the CP transformation. Since there is no a-priori reason to assume such a symmetry, this is known as the "strong CP problem". An elegant solution was suggested by Peccei and Quinn in 1977 [34]. They suggested that a field ϕ exists such that the modified Lagrangian becomes

$$\mathcal{L} = \left(\frac{\phi}{f_a} - \bar{\Theta}\right)\frac{\alpha_s}{8\pi}G^{\mu\nu a}\tilde{G}^a_{\mu\nu} \tag{5.13}$$

the vacuum expectation value (VEV) of ϕ is zero above some energy scale f_a, and acquires a nonzero VEV under f_a, of $\bar{\Theta}f_a$ (in a spontaneous symmetry breaking mechanism), which cancels out $\bar{\Theta}$ in Eq. (5.13) and makes this term in the whole Lagrangian vanish. This then gives a symmetry-invariant Lagrangian under the CP transformation, and naturally solves the strong CP problem. The particles which are the excitations of this nonzero VEV field after the symmetry breaking (the Goldstone bosons) are called "axions". The properties of the axion such as its mass and its coupling to photons all depend on the energy scale f_a:

$$m_a = 6\,\mathrm{eV}\left(\frac{10^6\mathrm{GeV}}{f_a}\right) \tag{5.14}$$

and

$$g_{a\gamma\gamma} = \frac{\alpha g_\gamma}{\pi f_a} \tag{5.15}$$

where g_γ is a dimensionless model-dependent parameter of order unity [35]. Now let's examine how well this particle can fit as a dark matter candidate. First, for a large value of the energy scale f_a, the coupling of the axion to photons is small, which fits the requirement of it being dark. Second, if axions make up a significant fraction of dark matter, the bounds on the axion mass are fairly strict. Supernova SN1987a occured in the Large Magellanic Cloud, a nearby satellite galaxy of the Milky Way. Most of the energy was released in the form of neutrinos. Measurements of those had put an upper limit on the mass of axions: too heavy of a mass would have distorted the escape time of neutrinos on their way to Earth in a measurable way. Axions with masses much above 10^{-2} eV would be in conflict with the number of neutrinos observed in this supernova [36]. On the other hand, the smaller the mass of the axions, the larger their energy density. Cosmology dictates that their density (relative to the critical density) is [35]

$$\Omega_a = \left(\frac{6\,\mu\text{eV}}{m_a}\right)^{7/6} \tag{5.16}$$

An axion of $m_a \approx 20\,\mu$eV would thus account for the entire dark matter density of the universe, $\Omega_m \approx 0.23$. If the axion mass is much below 1 μeV it would mean that the big bang produced way more axions than necessary to account for dark matter, which is unreasonable. This gives the best mass range estimate for dark matter axions of $10^{-6}\,\text{eV} < m_a < 10^{-2}\,\text{eV}$. It might seem like because of its small mass, the axion would be relativistic in the early universe just like the neutrino, and thus form a hot dark matter which wouldn't be able to establish structure formation and therefore can not form a good DM candidate. However, the very weak interactions of it with other particles mean that unlike the neutrino, it never was in thermal equilibrium with other particles in the early universe, and axions would have formed as a boson condensate of cold dark matter. The above features make the axion an excellent cold dark matter candidate.

While the axion could be what the majority of dark matter is made of, its existence was first motivated by the strong CP problem, and it is perfectly possible that axions outside the DM range exist, and are the solution to the strong CP problem while not being part of the DM particles in the universe. Furthermore, axion-like particles (ALP) are also motivated by string theory, and they are not bound to specific QCD models. Whether they exist or not, one thing is certain: Axions are worth searching for!

Chapter 6

Axion detection experiments

In this section I describe some of the major existing and planned experiments for detection of axions. These fall into 3 main categories: Haloscopes, helioscopes and LSW (light shining through a wall). Some other experiments are described as well. As we have seen, the axions are predicted to interact very weakly with photons (as seen from Eq. (5.2.4), with the energy scale f_a being large). This makes them an excellent dark matter candidate, but also hard to detect. Pierre Sikivie from the University of Florida came up with an idea in 1983 which made the detection of axions much more practical: Axions are much more likely to convert to photons under the influence of a strong magnetic field [37]. Likewise photons are likely to convert to axions under a strong magnetic field. This is based on the Primakoff effect, where neutral pseudoscalar mesons are likely to be created by or decay to photons under a strong magnetic field. Sikivie envisioned a microwave cavity in which this is employed, but this is a key component in most axion detection experiments today. To summarize the progress and results of experiments, Figure 6.2 is included at the end of the chapter, with the current and future searched parameter space. In it, the QCD band including the KSVZ and DFSZ models contain the region where axions solve the strong CP problem. As we saw in the previous chapter, dark matter axions are most likely to be in the range $\sim 10^{-6} - 10^{-2}$ eV, while QCD axions don't need to be (axions might solve the strong CP problem and not be dark matter). In addition to this, string theories predict that axion-like particles (ALP) are not restricted to the QCD band. Therefore in practice all of the (m_a, $g_{a\gamma\gamma}$) parameter space is interesting for axion search. In preparing the following descriptions, I found sources [35], [38] to be particularly helpful.

6.1 Haloscopes

Haloscopes are experiments designed to detect dark matter axions existing in the galactic halo. A main type of such experiments is the microwave cavity. Dark matter axions have typical nonrelativistic galactic speeds of $v \sim 10^{-3}c$ and hence negligible kinetic energy (since $E_{\text{tot}} = m_a c^2 + \frac{1}{2} m_a v^2 = m_a c^2(1 + v^2/2c^2) = m_a c^2(1 + \mathcal{O}(10^{-6})))$. Hence the resonance condition is approximately $h\nu = m_a c^2$ and with the assumed mass range for dark matter axions, the resulting photon frequency ν is in the microwave. The conversion power of axions to photons is given by [35]

$$P_{\text{SIG}} = \eta g_{a\gamma\gamma}^2 \left(\frac{\rho_a}{m_a}\right) B_0^2 V C Q_L \tag{6.1}$$

where ρ_a is the mass density of axions in the halo, m_a is the axion mass and $g_{a\gamma\gamma}$ is the axion-photon coupling. The quantities η (fraction of power coupled to the antenna), B_0 (magnetic field), V (volume), C (mode-dependent form-factor) and Q_L (loaded quality factors) are experimentally controlled. The system signal-to-noise ratio is given by

$$\frac{S}{N} = \frac{P_{\text{SIG}}}{kT_{\text{SYS}}} \sqrt{\frac{t}{\Delta\nu}} \tag{6.2}$$

where t is the integration time, $\Delta\nu$ is the bandwidth of the axion signal, and $T_{\text{SYS}} = T + T_{\text{N}}$ is the sum of the physical temperature and the noise temperature of the amplifier.

6.1.1 ADMX

The Axion Dark Matter eXperiment is the main haloscope experiment. It is located at the University of Washington. It has been able to achieve the stringent bounds on the axion-photon coupling yet, but for a narrow mass range in the μeV. A schematic of the system is shown in Figure 6.1. In the experiment, axions enter a microwave cavity of $Q \sim 10^5$, and if their mass is resonant with the cavity resonance frequency, they are converted into photons (the system has a main $8\,T$ magnet, which increases the probability of this process to happen). The signal is then detected and amplified using the SQUID amplifier. The role of the bucking magnet is to cancel the magnetic field of the main magnet in order to allow the detection of the tiny signal. By changing the cavity resonance frequency, a range of axion masses can be scanned. The system is cooled to a low temperature in order to reduce thermal noise. The first phase of the experiment (1995-2004) had been cooled to superfluid temperatures, having a noise temperature of $T_N \sim 1.5\,\mathrm{K}$. In the second phase of the experiment, the temperature was reduced to $T_N < 1.5\,T_{\mathrm{SQL}}$ (where SQL is the Standard Quantum Limit, an irreducible noise contribution of linear amplifiers, $kT_{\mathrm{SQL}} = h\nu$) [35]. To date, ADMX has covered $460\,\mathrm{MHz} - 1.01\,\mathrm{GHz}$ in frequency, corresponding to axion mass of $1.9 - 4.2\,\mu\mathrm{eV}$ [39], [40] and had been able to reach KSVZ sensitivities (see Figure 6.2). ADMX will soon incorporate a dilution refrigerator which should reduce the temperature to $T_{\mathrm{SYS}} < 200\,\mathrm{mK}$, sensitive to DFSZ axions.

A second, smaller ADMX platform, named ADMX-HF, is planned with a magnetic field of $9.4\,\mathrm{T}$, experiment temperatures of $T \sim 25\,\mathrm{mK}$, with noise temperature $T_N \sim T_{\mathrm{SQL}}$. In its initial configuration, the experiment is projected to reach a sensitivity in axion-photon coupling of $\sim 2 \times$ KSVZ. A major R&D effort is to use a receiver based on squeezed vacuum states to overcome the quantum noise limit (used currently only by LIGO and GEO). It will use a Josephson parametric amplifier to measure the signal. ADMX development has been able to achieve a noise temperature of $T_N = h\nu/4$.

6.2 Low mass axion searches

6.2.1 NMR based experiment: CASPEr-Wind

The Cosmic Axion Spin Precession Experiment (CASPEr)-Wind, located in Johannes Gutenberg University Mainz in Germany, is an experiment for detecting axions or ALP

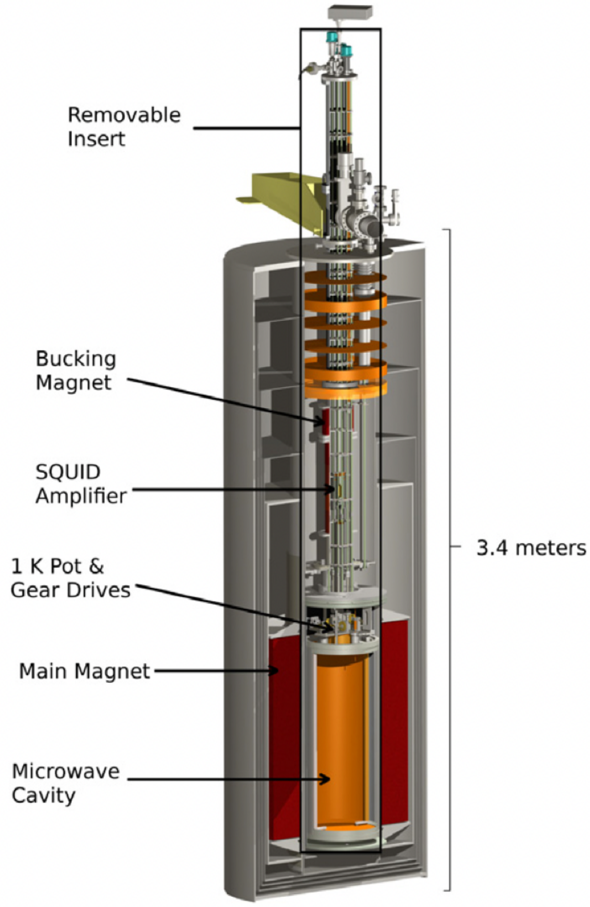

Figure 6.1: Schematic of the ADMX system. The DM axion enters the the microwave cavity where it is resonantly converted to microwave photons, under the effect of the magnetic field from the main magnet, which enhances this process. The bucking magnet then cancels the field of the main magnet to allow the weak signal to be detected, and it is then enhanced with the SQUID amplifier. The figure is adapted from [41]

.

dark matter, relying on the interaction of the axion field with the proton and neutron spins, described by the Lagrangian

$$\mathcal{L} = g_{aNN}[\partial_\mu a(\vec{r},t)]\bar{\Psi}_n\gamma^\mu\gamma_5\Psi_n \tag{6.3}$$

where g_{aNN} is the coupling between the axion and the nucleon spins, Ψ_n is the nucleon wave function and γ^μ and γ_5 are Dirac matrices. Unlike other axion experiments which rely on a loop-level axion-photon interaction, this one relies on a tree-level interaction of the axion with SM particles. The gradient is proportional to an effective magnetic field. In the nonrelativistic limit the Hamiltonian can be written as $\gamma\vec{B_a}\cdot\vec{\sigma_N}$ where

$$\vec{B_a} = \frac{g_{aNN}}{\gamma}\nabla a \simeq g_{aNN}\frac{\sqrt{2\rho_{DM}}}{\gamma}\cos(\omega_a t)\vec{v}_a \tag{6.4}$$

acts as an effective oscillating magnetic field which couples to nuclear spins [42]. Here $\vec{v}_a \sim 10^{-3}c$ is the DM velocity, $\rho_{DM} \approx 0.3\,\mathrm{GeV/cm^3}$ is the local DM density and γ is the gyromagnetic ratio. Because $\vec{B_a}$ is proportional to the DM velocity, this interaction is known as the "axion wind". CASPEr-Wind experiments are aimed to detect this wind. The main idea behind CASPEr-Wind is to use the time-varying nature of the effect to cause precession of nuclear spins in a sample of material. The Larmor frequency of the nuclear spins is scanned by increasing the magnetic field and at the frequency corresponding to the mass of the axion, an NMR signal is observed using a precise magnetometer. The experiment is aimed to explore a low mass range currently not searched for by other experiments. First experimental results were published in 2019 excluding ultralight ALP dark matter in the mass ranges $10^{-22}\,\mathrm{eV}$ to $1.3\times10^{-17}\,\mathrm{eV}$ with coupling constants $g_{aNN} > 6\times10^{-5}\,\mathrm{GeV^{-1}}$ [43] and $1.8\times10^{-16}\,\mathrm{eV}$ to $7.8\times10^{-14}\,\mathrm{eV}$ corresponding to Compton frequencies ranging from 45 mHz to 19 Hz with coupling constants $g_{aNN} > 5\times10^{-5}\,\mathrm{GeV^{-1}}$ [44]. A second apparatus, CASPEr-Wind high field (HF), currently under construction, will be capable of searching for ALPs with masses up to $\approx 2.4\times10^{-6}\,\mathrm{eV}$ [45].

6.3 Helioscopes

Axions or ALPs can be naturally produced inside the Sun's core, where the Sun's plasma creates a strong magnetic field which enhances the conversion of emitted photons into axions by the Primakoff effect. This flux of axions arrives Earth, and can be detected using an axion helioscope. These helioscopes implement a strong magnetic field, under which the axions convert back into photons. Considering the energies, these detected photons are in the x-ray range. The probability that a photon will convert to an axion inside the helioscope, traveling a length L in a magnetic field B, is [46] [35]

$$P_{a\gamma} = 2.6 \times 10^{-17} \left(\frac{g_{a\gamma\gamma}}{10^{-10}\,\mathrm{GeV}^{-1}}\right)^2 \left(\frac{B}{10\,\mathrm{T}}\right)^2 \left(\frac{L}{10\,\mathrm{m}}\right)^2 F \tag{6.5}$$

where F is a form factor accounting for the coherence:

$$F = \frac{2(1-\cos qL)}{(qL)^2} \tag{6.6}$$

and q is the momentum transfer. Since the photon is massless but the axion is not, they would grow out of phase with distance, therefore to keep the coherence we need $qL \ll 1$. For $L \sim 10\,\mathrm{m}$ this happens at axion masses up to $\sim 10^{-2}\,\mathrm{eV}$.

6.3.1 CAST

The big existing helioscope project is CAST (CERN Axion Solar Telescope) operating since 2003. It uses the LHC magnet of 9 T over a length of 9.3 m, and uses pn-CCD combined with an x-ray mirror system for detection [47]. It was able to follow the sun a couple of hours every day using an elevation and azimuth drive, and is the first helioscope to use x-ray focusing optics as well as low background techniques. In its first phase, CAST-I, it obtained the coupling limit $g_{a\gamma\gamma} \lesssim 8.8\times10^{-11}\,\mathrm{GeV}^{-1}$ for $m_a \lesssim 0.02\,\mathrm{eV}$ [48]. The second phase of the experiment had been using ^{4}He and ^{3}He buffer gases and is still in operation today. A buffer gas provides an effective mass m_γ to the photons, making the axion-photon momentum difference equal to $q = (m_a^2 - m_\gamma^2)/2E$. Eq. (6.6) then implies that $m_a \simeq m_\gamma$ are most likely to be produced. Changing the pressure and hence m_γ allows for scanning of different axion masses, and the experiment was able to scan up to $m_a \lesssim 1.2\,\mathrm{eV}$ [49]. Figure 6.2 shows the parameter space scanned by it to date.

6.3.2 IAXO and BabyIAXO

The International AXion Observatory (IAXO) is a planned helioscope, with improved equipment that should enable it to surpass the sensitivity of CAST by more than an order of magnitude. It will employ a larger magnetic field over a larger distance, with a higher area and a more sensitive focusing system. The design intends to include a 25 m long toroid magnet, producing 2.5 T in 8 bores of 600 mm diameter [35]. To maximize the efficiency, each of the bores will be equipped with x-ray focusing optics, with the goal to reach background levels below $10^{-7}\,\mathrm{counts} \cdot \mathrm{keV}^{-1}\,\mathrm{cm}^{-2}\,\mathrm{s}^{-1}$. It is expected to have 5 orders of magnitude better signal to noise ratio than CAST, which will enable it to achieve sensitivity $\sim 10^{-12}\,\mathrm{GeV}^{-1}$, and probe a broad range of QCD models. In addition to the axion-photon coupling, the scientific plan should enable it to probe axion-electron and axion-nucleon couplings, and thus learn about production mechanisms of axions in the Sun. The first step to IAXO will be the BabyIAXO experiment. It is supposed to be a prototype of all subsystems of IAXO and its operation will enable to observe the full system integration and fix mistakes. In addition, it is a fully functional helioscope by itself. it will exceed the sensitivity of CAST by a factor of ~ 4, searching a similar axion mass range. It will employ a 2 T, 10 m long superconducting magnet with two bores, each with a 70 cm diameter. The BabyIAXO experiment relies on common-coil superconducting cables available only in Russian industry [38]. However, since the Russian invasion of Ukraine in February 2022, collaboration with Russian institutes is frozen and the magnet cables are still missing. This affects the planned schedule. After the approval of the experiment to be hosted at DESY, the collaboration has taken first steps towards its construction. The first data taking is expected in 2028. The projected parameter space to be probed is shown in Figure 6.2.

6.4 Light Shining through a Wall

Light Shining through a Wall (LSW) experiments aim at producing axions in the lab (rather than detecting axions from the galactic halo or the Sun). In this type of experiments typically a coherent light is produced using a laser at the generation side, and is then converted to axions using a strong magnetic field. It then passes through an optically opaque barrier (the wall); this ensures that photons are not able to pass, and only the weakly-interacting axions pass the barrier to the detection side; there, under the effect of a magnetic field, the axions are converted back to photons, which are analyzed. Without axions, no light would be produced in the detection side, so a signal measurement there proves the existence of axions. Most systems employ a Fabry-Perot cavity at the production and / or the detection side, in order to increase the effective light power. One advantage of this type of experiments is the theory independence (in contrast to haloscopes or helioscopes, which depend on astrophysical models). Another advantage is the control of the laser frequency, and hence the corresponding axion mass to be probed. The probability of a ($\gamma \to a \to \gamma$) oscillation is given by [50]

$$P_{\gamma\to a\to\gamma} = \frac{1}{16}(g_{a\gamma\gamma}BL)^4 \left(\frac{2}{qL}\sin\frac{qL}{2}\right)^4 \mathcal{F}_{PC}\mathcal{F}_{DC} \tag{6.7}$$

where $\mathcal{F}_{PC}$ is the finesse of the production cavity, $\mathcal{F}_{DC}$ is the finesse of the detection cavity, and q is the momentum transfer between the photon and axion, given by $q = \left|\omega - \sqrt{\omega^2 - m_a^2}\right|$.

6.4.1 ALPS I

The Any Light Particle Search (ALPS) 1 at DESY operated between 2007-2010. It consisted of a 5 T HERA superconducting magnet and had two arms of 4.3 m each. It used a frequency doubled 1064 nm laser light with a power of 5W at 532 nm. The laser entered a vaccuum pipe where the photon-axion conversion was designed to happen. In order to increase the efficiency of the conversion, an optical resonator enclosed the generation pipe in order to increase the laser power and therefore enhance a hypothetical axion flux. It was the first LSW experiment to use a cavity in the generation tube. The beam would then pass an optically-thick wall into the detection pipe. Reconverted photons would have the same TEM_{00} mode as in the generation resonator. Such photons would then be directed to a CCD camera for detection. The newest results were published during 2009-2010 [51] and are shown in Figure 6.2.

6.4.2 OSQAR

The OSQAR (Optical Search for QED Vacuum Birefringence, Axions, and Photon Regeneration) experiment at CERN uses two 9 T dipole magnets of the LHC facility, and has a total length of 2×14.3m. It is using an 18.5 W continuous wave laser at a wavelength of 532 nm. After exiting the second magnet, the laser beam is focused by an optical lens onto a thermoelectric CCD which is cooled to a temperature in the -92^oC to -95^oC range to reduce thermal noise. In 2014 this experiment achieved its current best limits of $g_{a\gamma\gamma} < 3.5 \times 10^{-8}\,\mathrm{GeV}^{-1}$ at 95% CL for $m_a < 0.3\,\mathrm{meV}$ [52]. Its parameter space exclusion regions are sketched in Figure 6.2.

6.4.3 ALPS II

Any Light Particle Search number 2 will employ two long arms and high-finesse optical cavities both before and after the light-blocking wall. The experiment will use a 30 W, 1064 nm laser. It will also use a long string of superconducting dipole magnets. These are expected to increase the sensitivity by a factor of 10^3 relative to ALPS I. The experimental parameters are: $\mathcal{F}_{PC} = 5000$, $\mathcal{F}_{RC} = 40000$, $B = 5.3\,\mathrm{T}$, $L = 105.6\,\mathrm{m}$. Using Eq. (6.7) and taking $g_{a\gamma\gamma} = 2 \times 10^{-11}\,\mathrm{GeV}^{-1}$ (motivated by astrophysics) gives $P_{\gamma\to a\to\gamma} \sim 10^{-25}$. With these parameters, about 2 photons/day are expected to be detected as a result of the photon $\to$ axion $\to$ photon conversion [38]. ALPS II will have two different types of detectors. One of these is a heterodyne detector (HET) which measures the interference beat note between a local oscillator laser and the regenerated photon field, and the other is a Transition Edge Sensor (TES) operating at about 100 mK. It allows counting individual 1064 nm photons with energy resolution of 7% [38]. Each of those detectors has different systematic errors. Thus, if both of them get a signal with the same intensity, this increases the reliability of both coming from the axion detection. However, since the two detectors require different optical systems to operate, they cannot be used in parallel. The installation of ALPS II began in 2019 and a first science run with the HET detector is planned for 2024. Projected results of ALPS-II experiment are shown in Figure 6.2.

6.5 Other experiments

Here we consider additional experiments to detect axions, proposed in recent years.

6.5.1 Interferometry-based detection

An interferometry-based experiment had been suggested [54] in which a laser beam traverses a region of a magnetic field used to convert some of the photons to axions. This changes the intensity and the phase of the original beam. It then interferes with a beam from the original source. Unlike traditional LSW experiments, there is only one conversion of photons-to-axions, and no second conversion of axions-to-photons, therefore the sensitivity is higher and is proportional to $g_{a\gamma\gamma}^2$ instead of $g_{a\gamma\gamma}^4$. However, shot-noise limits the sensitivity. The situation is improved by the use of squeezed-light.

6.5.2 LSW in plasma

A plasma-based detection had been proposed in [55]: In the plasma, the presence of axions creates a new type of quasiparticle: the axion-plasmon polariton. The plasmon is an unstable electron wave, and if a magnetic field is applied, only the axion component will be affected by it and will grow in expense of the plasmon, therefore generating axions. These axions can then be converted into photons in a regeneration chamber and be detected, in a manner similar to traditional LSW experiments.

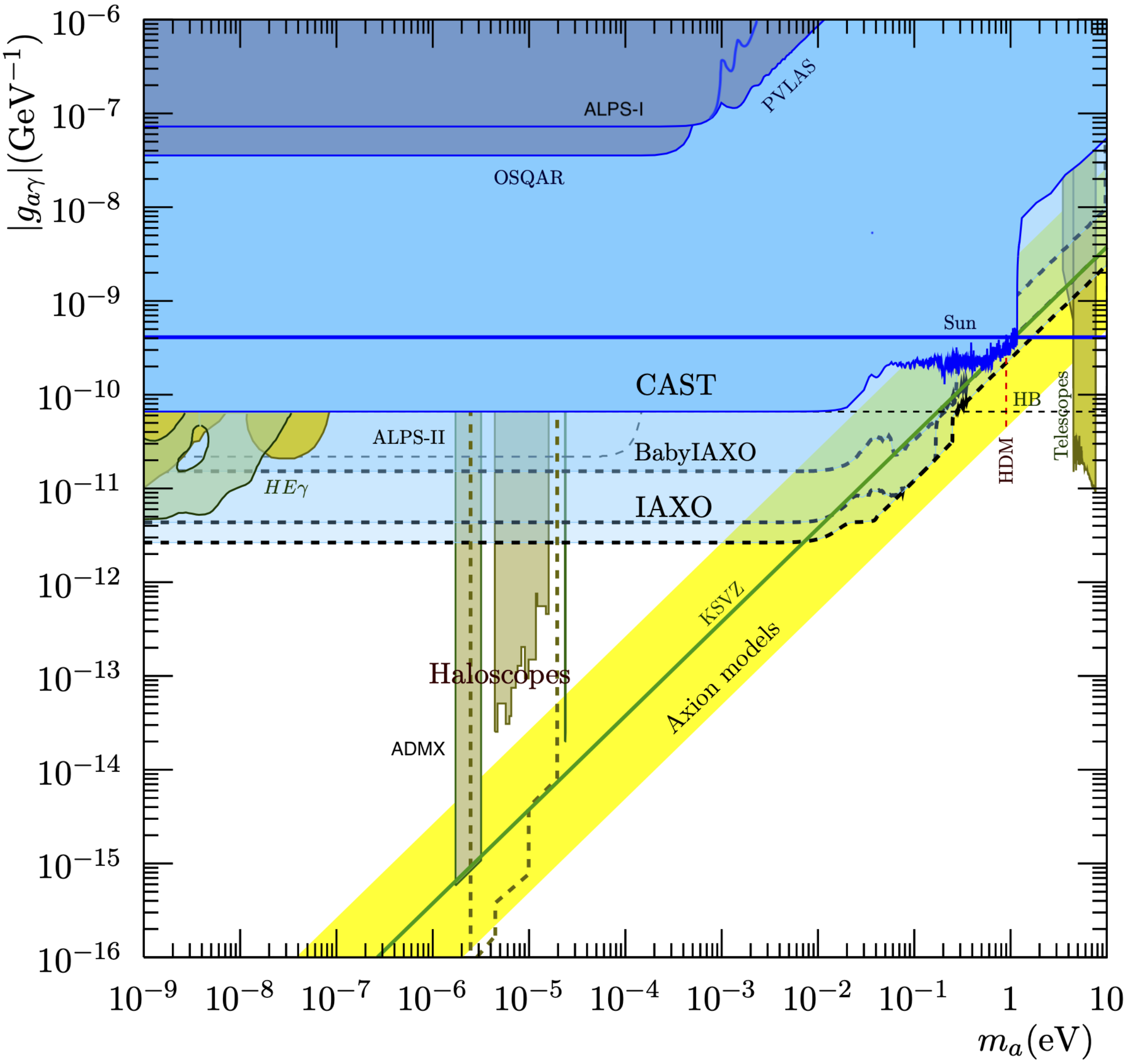

Figure 6.2: Scanned parameter space of current and future axion experiments. Solid lines indicate exclusion results of current experiments, while dashed lines indicate projection bounds of future experiments. The yellow band represents QCD models, where axions solve the strong CP problem. Adapted from [53].

Chapter 7

Our axion-detection scheme

7.1 Introduction

We propose a plan for LSW-type experimental system (to be built in the future) based on four-wave mixing of lasers in optical fibers, for detecting the axions. A detailed description is given in the sections below, but here is an overview of the setup: The system consists of two separate axion waveguides (optical fibers), a generation fiber and a detection fiber, see Figure 7.1. In the generation fiber, strong pump and Stokes laser beams are combined, and their nonlinear interaction of electromagnetic fields, $\vec{E} \cdot \vec{B}$, resonantly generates axions which propagate as fiber modes. By carefully choosing the frequencies of the pump and Stokes lasers, we can scan different axion masses to be searched. These axions leak into a detection fiber, while the laser photons are blocked. In the detection fiber we employ two laser beams as well: a mixing beam and a probe beam. Their frequencies are chosen such that the interaction of the incoming axions with the mixing beam generates photons at the probe frequency. This affects the intensity and phase of the probe beam. These changes are detected using a homodyne detector (for simplicity, we focus on changes only in intensity which are detected by a balanced detector). In the absence of axions, the probe and mixing beams don't interfere since they have different frequencies. Axions create the conditions for interference, and a nonzero signal is detected.

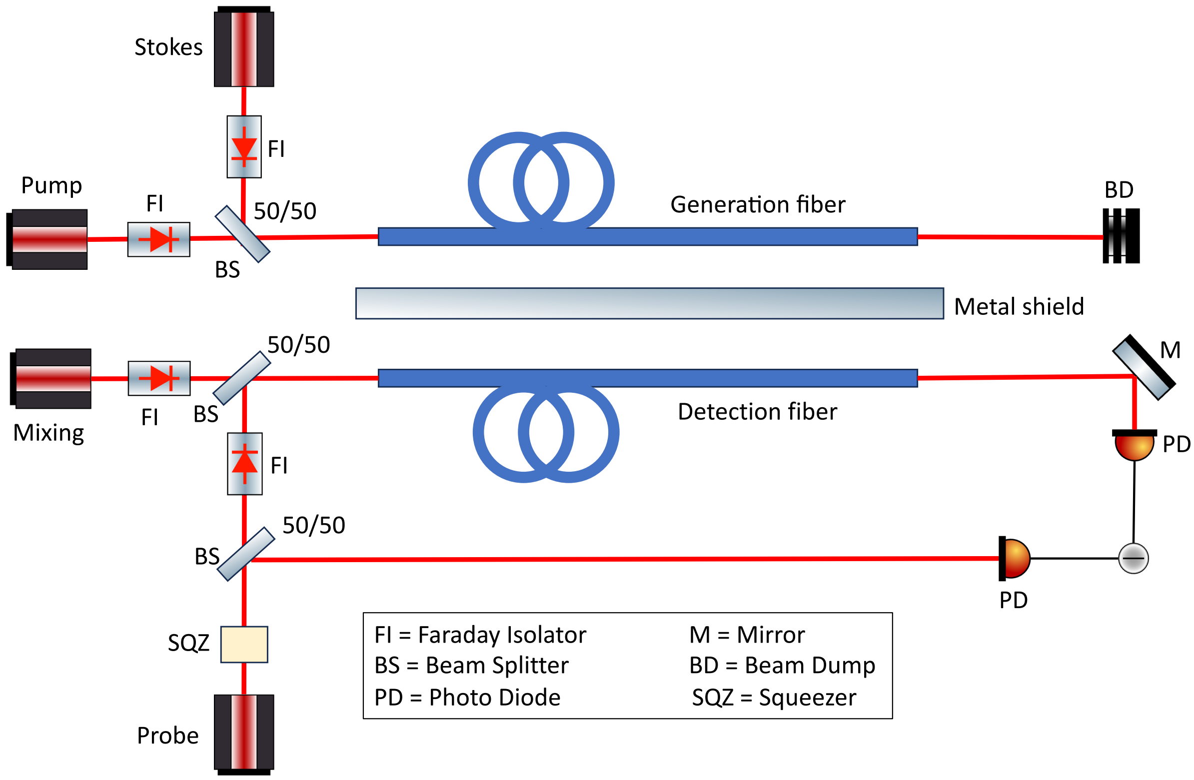

Figure 7.1: The experimental scheme for axion generation and detection. The pump and Stokes beams generate axions in the generation fiber. These axions pass through the fibers and the metal shield to the detection fiber, while photons are blocked. These axions mix with the mixing beam, generating photons at the probe frequency. The changes in intensity of the probe beam are then measured using a balanced detector.

7.2 Electromagnetic and axion field equations

The Lagrangian describing the axion and electromagnetic fields is given by [56]:

$$\mathcal{L} = \frac{1}{2}\partial_\mu\phi\partial^\mu\phi - \frac{1}{2}\left(\frac{mc}{\hbar}\right)^2\phi^2 - \frac{1}{4\mu_0}F_{\mu\nu}F^{\mu\nu} - A_\mu j^\mu - \frac{g_{a\gamma\gamma}}{8\mu_0}\phi\,\varepsilon^{\mu\nu\alpha\beta}F_{\mu\nu}F_{\alpha\beta} \tag{7.1}$$

where ϕ represents the axion field and $F^{\mu\nu}$ is the electromagnetic tensor. The first 4 terms in the Lagrangian are the free-field terms. The first two terms describe the free axion field, and the next two terms describe the electromagnetic field (including sources). The last term in blue color describes the interaction between these fields. This term can also be written as

$$\mathcal{L}_{a\gamma\gamma} = \frac{g_{a\gamma\gamma}}{\mu_0 c}\phi\,\vec{E}\cdot\vec{B} \tag{7.2}$$

Based on this Lagrangian it is possible to derive the axion field equation and the modified Maxwell's equations for the EM field. In these, there will be coupling between the fields. The derivation is shown in Appendix D. For a medium with no free charge density and with current density $\vec{J}$ the resulting electromagnetic field equations are:

$$\vec{\nabla}\cdot\vec{E} = -g_{a\gamma\gamma}c\vec{\nabla}\phi\cdot\vec{B} \tag{7.3}$$

$$\vec{\nabla}\cdot\vec{B} = 0 \tag{7.4}$$

$$\vec{\nabla}\times\vec{E} = -\frac{\partial\vec{B}}{\partial t} \tag{7.5}$$

$$\vec{\nabla}\times\vec{B} = \frac{1}{c^2}\frac{\partial\vec{E}}{\partial t} + \mu_0\vec{J} + \frac{g_{a\gamma\gamma}}{c}\left(\frac{\partial\phi}{\partial t}\vec{B} + \vec{\nabla}\phi\times\vec{E}\right) \tag{7.6}$$

and the resulting axion field equation is:

$$\nabla^2\phi - \frac{1}{c^2}\frac{\partial^2\phi}{\partial t^2} - \left(\frac{mc}{\hbar}\right)^2\phi = -\frac{g_{a\gamma\gamma}}{\mu_0 c}\vec{E}\cdot\vec{B} \tag{7.7}$$

where the blue-colored terms are additional terms to the Maxwell / Klein-Gordon equations due to the field interactions. Maxwell's equations for $\vec{\nabla}\cdot\vec{E}$ and $\vec{\nabla}\times\vec{B}$ acquired additional charge and current density terms while the other two were unaffected, and the axion field equation acquired a term proportional to $\vec{E}\cdot\vec{B}$ which produces an effective second-order nonlinearity. In the following, we will borrow many ideas from nonlinear optics, specifically from four-wave mixing processes [57].

7.3 Generation of guided axion waves: axitons

Let us consider the generation waveguide (an optical fiber). In this fiber, we use two strong laser beams: pump and Stokes. Through the term $\vec{E}\cdot\vec{B}$, the electric field of the pump and the magnetic field of the Stokes will drive the axion generation. We take the fiber to be cylindrically symmetric and assume the pump and Stokes lasers to be in specific modes of the fiber. A schematic of the energy levels of the laser beams and the axion, along with a schematic of the guided axion waves, which we term "axitons" are shown in Figure 7.2. Working in cylindrical coordinates (r,φ,z) we can write these two fields as

$$\begin{aligned}\vec{E}_P(r,\varphi,z) &= E_P\, u_P(r)\exp(i\ell_P\varphi)\exp(i\beta_P z - i\omega_P t)\hat{e} + \text{c.c}\\ \vec{B}_S(r,\varphi,z) &= -B_S\, u_s(r)\exp(i\ell_S\varphi)\exp(i\beta_S z - i\omega_S t)\hat{e} + \text{c.c}\end{aligned} \tag{7.8}$$

where c.c denotes complex conjugation. Here, the minus sign in the expression for $\vec{B}_S$ is arbitrary and was chosen in order to make the RHS in the later Eq. (7.15), following from Eq. (7.7), positive. E_P and B_S are the electric and magnetic field amplitudes for the pump and Stokes laser beams, and $\hat{e}$ denotes the common polarization direction for the two vectors (which is any direction orthogonal to the propagation direction $\hat{z}$). The quantities $u_P(r)$ and $u_S(r)$ are the radial mode functions of the corresponding lasers, and the integers ℓ_P and ℓ_S are typically referred to as orbital angular momentum numbers for the associated photons [57]. β_P and β_S are the propagation constants and ω_P and ω_S are angular frequencies of the waves. Noting the energy diagram of Figure 7.2, the

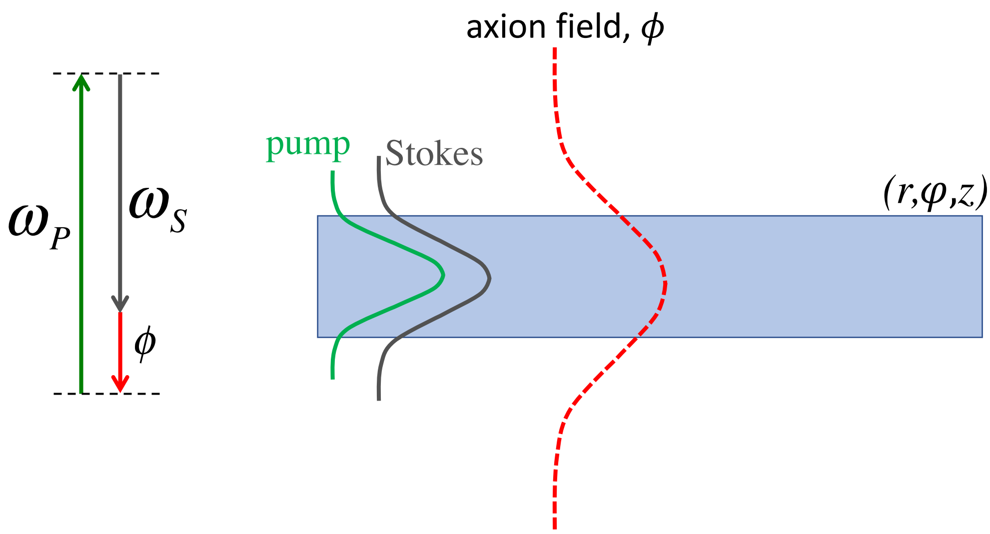

Figure 7.2: Energy level diagram and simplified schematic for producing guided axitons. Pump and Stokes laser beams having a frequency difference $\omega_P - \omega_S$, are tuned close to the rest energy of the axion, resonantly drive axion generation. The two lasers are confined to an optical fiber and the solid curves are cartoon schematics for the radial profiles of the two lasers. The spatial profiles of the two beams then confine axion generation, producing guided axitons, which are shown in the dashed curve.

frequency difference of the pump and Stokes beams, $\omega_P - \omega_S$ is tuned close to the rest energy of the axion. In general, there is another contribution to the generation of the axion wave, which is driven by the magnetic field of the pump and the electric field of the Stokes laser. For plane-wave like lasers propagating inside a bulk material, this second contribution (which is proportional to $B_P E_S^*$), would interfere destructively with the main contribution that we consider below (which is proportional to $E_P B_S^*$), reducing the produced axion amplitude. Therefore, we choose the relevant modes of the fiber appropriately so that this second contribution can be ignored compared with the first one. For example, one could use a TE (transverse electric) mode for the pump, and a TM (transverse magnetic) mode for the Stokes laser. This way, the vectors E_P and B_S can be aligned, maximizing the dot product. However, an angle would be present between B_P and E_S, which can be tuned to minimize their dot product using specific choice of modes. Because the axion generation is driven by the $\vec{E} \cdot \vec{B}$ term, we are looking for axion field solutions of the form:

$$\phi(r,\varphi,z) = u_\phi(r)\exp[i(\ell_P-\ell_S)\varphi]\exp[i(\beta_P-\beta_S)z - i(\omega_P-\omega_S)t] + \text{c.c} \tag{7.9}$$

Using Eqs. (7.8) and (7.9) in the axion field equation (7.7), using the Laplacian operator in cylindrical coordinates, and taking the terms in Eq. (7.8) that produce the same exponents as in the axion ansatz (7.9) and denoting the exponential terms as "exponents", we get

$$\begin{aligned}
&\left[\frac{1}{r}\left(\frac{du_\phi}{dr} + r\frac{d^2u_\phi}{dr^2}\right) - \frac{(\ell_P-\ell_S)^2}{r^2}u_\phi(r) - (\beta_P-\beta_S)^2u_\phi(r)\right]\cdot(\text{exponents}) \\
&\quad + \frac{1}{c^2}(\omega_P-\omega_S)^2u_\phi(r)\cdot(\text{exponents}) - \left(\frac{mc}{\hbar}\right)^2 u_\phi(r)\cdot(\text{exponents}) \\
&\quad = \frac{g_{a\gamma\gamma}}{\mu_0 c}\cdot E_P\,u_P(r)\,B_S^*\,u_s^*(r)\cdot(\text{exponents})
\end{aligned} \tag{7.10}$$

which yields after cancelling out the exponent terms:

$$\begin{aligned}
&\frac{d^2u_\phi(r)}{dr^2} + \frac{1}{r}\frac{du_\phi(r)}{dr} - \frac{(\ell_P-\ell_S)^2}{r^2}u_\phi(r) + \left[\frac{(\omega_P-\omega_S)^2}{c^2} - (\beta_P-\beta_S)^2 - \left(\frac{mc}{\hbar}\right)^2\right]u_\phi(r) \\
&= \frac{g_{a\gamma\gamma}}{\mu_0 c}\,E_P\,B_S^*\,u_P(r)\,u_S^*(r)
\end{aligned} \tag{7.11}$$

to simplify this equation, denote

$$\Delta k^2 \equiv \frac{(\omega_P-\omega_S)^2}{c^2} - (\beta_P-\beta_S)^2 - \left(\frac{mc}{\hbar}\right)^2 \tag{7.12}$$

this is the energy difference in units of a k-vector between the pump and Stokes lasers and the axion, since:

$$\frac{\Delta E^2_{\text{lasers}}}{c^2\hbar^2} = \frac{\hbar^2(\omega_P-\omega_S)^2}{c^2\hbar^2} = \frac{(\omega_P-\omega_S)^2}{c^2} \tag{7.13}$$

and

$$\frac{E_{\text{axion}}^2}{c^2\hbar^2} = \frac{p^2c^2 + m^2c^4}{c^2\hbar^2} = \frac{p^2}{\hbar^2} + \frac{m^2c^2}{\hbar^2} = \beta_{\text{axion}}^2 + \left(\frac{mc}{\hbar}\right)^2 = (\beta_P - \beta_S)^2 + \left(\frac{mc}{\hbar}\right)^2 \quad (7.14)$$

To make the physics stand out, define the dimensionless quantities $\tilde{r} \equiv \kappa_{\text{axion}} r$ and $\Delta\tilde{k} \equiv \Delta k/\kappa_{\text{axion}}$ which are r and Δk scaled by the Compton wave-number of the axion, $\kappa_{\text{axion}} = mc/\hbar$. With these changes, the radial equation reads:

$$\frac{d^2u_\phi}{d\tilde{r}^2} + \frac{1}{\tilde{r}}\frac{du_\phi}{d\tilde{r}} - \frac{(\ell_P - \ell_S)^2}{\tilde{r}^2}u_\phi + \Delta\tilde{k}^2 u_\phi = \frac{1}{\kappa_{\text{axion}}^2}\frac{g_{a\gamma\gamma}}{\mu_0 c}E_P B_S^* \, u_P(\tilde{r})u_S^*(\tilde{r}) \quad (7.15)$$

Given the parameters of the system, this equation can now be numerically integrated to find the radial profile of the axion excitation, $u_\phi(\tilde{r})$. We will now look at physical solutions to this equation that have a maximum at $\tilde{r} = 0$. We impose the boundary condition: $\frac{du_\phi}{d\tilde{r}}(\tilde{r} = 0) = 0$. We then numerically integrate Eq. (7.15), with a trial initial state $u_\phi(\tilde{r} = 0)$. For a given initial state, the integration will typically not result in a bounded axion field, i.e. $u_\phi(\tilde{r} \to \infty) \neq 0$, which is not physical. Given the parameters of the system, we vary the initial state $u_\phi(\tilde{r} = 0)$ until a bounded solution with $u_\phi(\tilde{r} \to \infty) = 0$ is found.

Figure 7.3 shows numerically calculated normalized axiton profiles, $u_\phi(\tilde{r})$, for $\Delta\tilde{k}^2 = -1$ (solid black), $\Delta\tilde{k}^2 = -0.1$ (solid red), and $\Delta\tilde{k}^2 = -0.01$ (solid green), respectively. For comparison, the dashed blue line shows the mode profiles for the driving laser beams, $u_P(\tilde{r})$ and $u_S(\tilde{r})$. Here, for simplicity, we take the profiles for the pump and Stokes laser beams to be Gaussian with unity width, $u_P(\tilde{r}) = u_S^*(\tilde{r}) = \exp(-\tilde{r}^2)$. We also take the angular momentum numbers for the pump and Stokes fields to be the same, $\ell_P = \ell_S$. Due to well-known Bessel function solutions to differential equations of the form of Eq. (7.15), for a physical bounded solution such that $u_\phi(\tilde{r} \to \infty) = 0$, we require $\Delta\tilde{k}^2 < 0$. As the quantity $\Delta\tilde{k}^2$ gets closer to 0, the axiton radial mode profile gets broader and extends significantly beyond the confinement of the driving lasers. This is well-illustrated in the solid green curve in Fig. 7.3. The quantity $\Delta\tilde{k}^2$ will likely be an

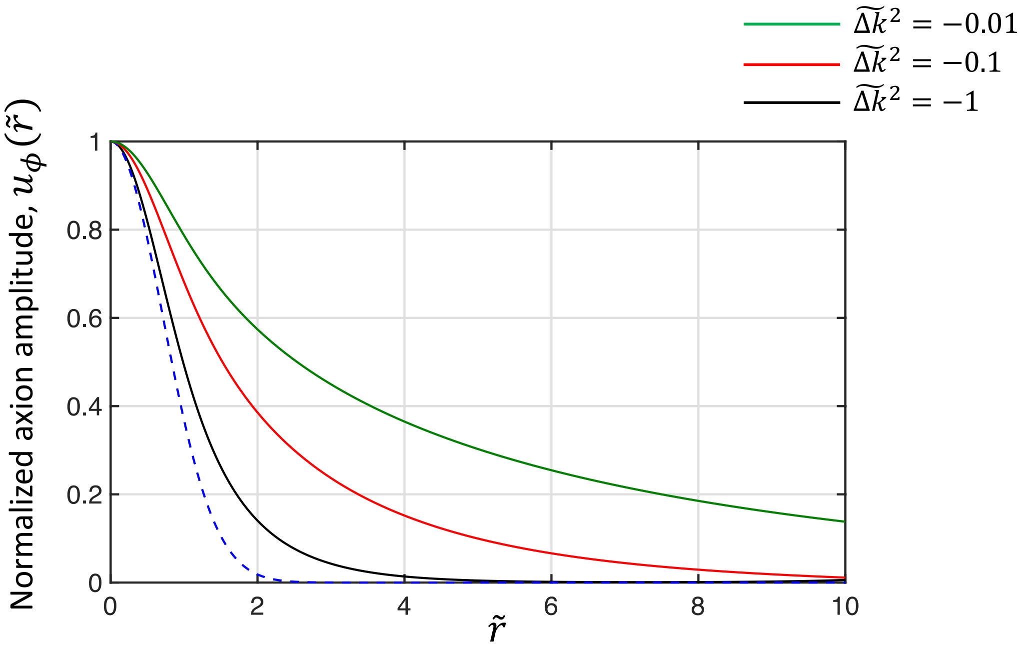

Figure 7.3: Numerically calculated normalized axiton profiles, $u_\phi(\tilde{r} = 0)$, for $\Delta\tilde{k} = -1$ (solid black), $\Delta\tilde{k} = -0.1$ (solid red) and $\Delta\tilde{k} = -0.01$ (solid green), respectively. For comparison, the dashed blue line shows the mode profiles for the driving laser beams, $u_P(\tilde{r})$ and $u_S(\tilde{r})$. For a bounded physical solution such that $u_\phi(\tilde{r} \to \infty) = 0$, we require $\Delta\tilde{k} < 0$. As the quantity $\Delta\tilde{k}^2$ gets closer to 0, the axion mode profile gets broader and extends significantly beyond the confinement of the driving lasers.

important parameter to tune in future experiments, since the broader the axion profile is, the more it will leak to the second fiber as we will discuss in the detection scheme below. The numerically found initial amplitudes for the axitons, each multiplied by the scaling factor on the right hand side of Eq. (7.15) (that is, by $g_{a\gamma\gamma} E_P B_S^* / (\mu_0 c\, \kappa_{\text{axion}}^2)$) are $u_\phi(\tilde{r} = 0) = 0.23$ (for $\Delta\tilde{k}^2 = -1$), $u_\phi(\tilde{r} = 0) = 0.48$ (for $\Delta\tilde{k}^2 = -0.1$), and $u_\phi(\tilde{r} = 0) = 0.76$ (for $\Delta\tilde{k}^2 = -0.01$), respectively. Once the radial mode profile for the axion field is numerically found as shown in Fig. 7.3, the expression in eq. (7.9) gives the full description of the axiton mode.

7.4 Detection of axions using the guided-wave geometry

In the previous section we focused on the generation of confined axitons by the pump and Stokes beams, which propagate along the fiber. Now, we discuss the second half of the problem, namely how to detect these guided axitons. The vision that we have for a future experiment is shown in Figure. 7.4. Inspired by the LSW experiments, we use a separate fiber, the detection fiber. This is necessary, since any material will possess a four-wave mixing nonlinearity, which would completely overwhelm the four-wave mixing interaction mediated by the axion field. We therefore need to make sure that the four involved laser beams do not spatially overlap. The central idea in Figure 7.4 is that the axiton mode produced in the generation fiber overlaps with the detection fiber, while the pump and Stokes laser beam profiles do not. If necessary, the extinction of the pump and Stokes lasers at the detection fiber can be guaranteed by putting a metal shield between the two fibers (see Figure 7.1 and section 7.6). In the detection fiber, the axion field mixes with the magnetic field of another laser, the mixing laser. Through the axion interaction, the mixing laser then affects the propagation (both phase and intensity) of a probe laser beam. The search for the axion relies on detecting this change in the probe laser beam. In a similar manner to the pump and Stokes beams in the generation fiber, we now take the mixing and probe lasers to be modes of the detection fiber and assume

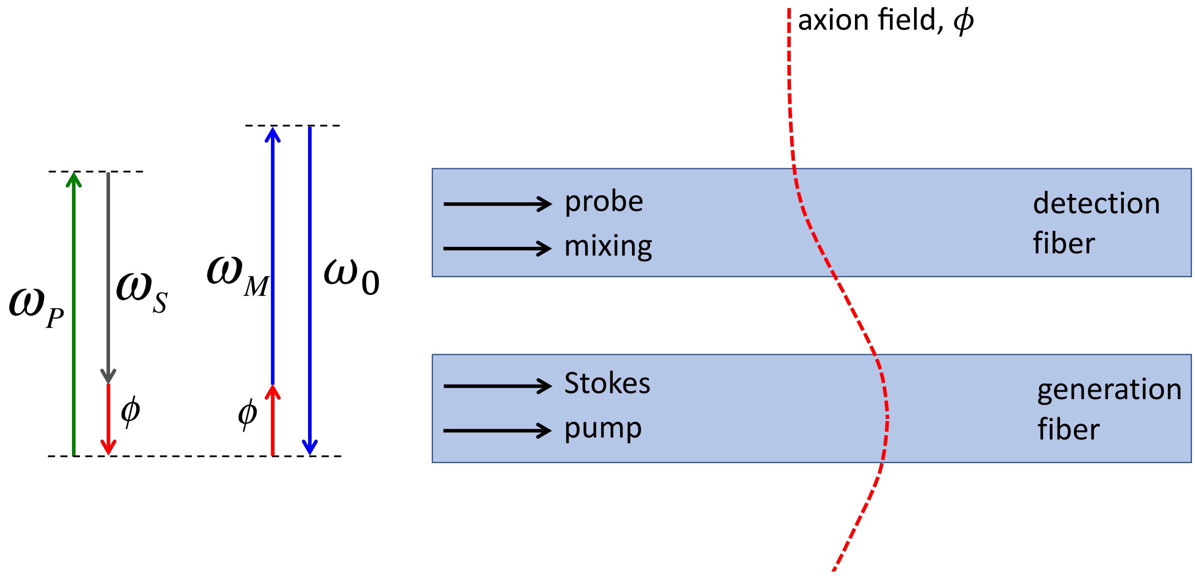

Figure 7.4: Left: energy level diagram for the four-wave mixing scheme for generating and detecting the axions. The axion field, ϕ, produced by the pump and Stokes laser beams mix with the mixing laser, affecting the propagation of the probe laser at frequency ω_0. The four-wave mixing interaction forms a closed loop: $\omega_P - \omega_S + \omega_M = \omega_0$. The mixing and the probe lasers propagate along a separate fiber, which we refer to as the detection fiber. Inspired by the LSW experiments, the axion field produced in the generation fiber (by the pump and Stokes lasers), overlaps with the detection fiber and mediates the interaction between the mixing and probe lasers.

the following forms for the two waves:

$$\begin{aligned} \vec{E}_{\text{probe}}(r,\varphi,z) &= E_0(z)u_0(r)\exp(i\ell_0\varphi)\exp(i\beta z - i\omega_0 t)\hat{e} + \text{c.c} \\ \vec{B}_M(r,\varphi,z) &= B_M u_M(r)\exp(i\ell_M\varphi)\exp(i\beta_M z - i\omega_M t)\hat{e} + \text{c.c} \end{aligned} \tag{7.16}$$

Here, B_M is the magnetic field amplitude of the mixing beam, and $E_0(z)$ is the electric field amplitude of the probe beam. It depends on the propagation coordinate z as a result of the interaction with the axion field. The change of $E_0(z)$ will allow the measuring of the changes in the intensity and the phase of the probe beam, thus detecting the axion. In the above expression, $u_0(r)$ and $u_M(r)$ are the radial mode functions of the probe and mixing beams, and ℓ_0 and ℓ_M are their angular momentum numbers. β_0 and β_M are the propagation constants in the direction of propagation, and ω_0 and ω_M are the angular frequencies. Now, in order to solve for the probe beam after the interaction with the mixing beam and the axion, we use Maxwell's equations to get an equation describing this interaction. Taking the equation

$$\nabla \times \vec{E} = -\frac{\partial \vec{B}}{\partial t} \tag{7.17}$$

then applying $\nabla\times$ on both sides and using a derivative identity,

$$\nabla \times \nabla \times \vec{E} = -\frac{\partial}{\partial t}\nabla \times \vec{B} \tag{7.18}$$

$$\therefore \nabla(\nabla \cdot \vec{E}) - \nabla^2 \vec{E} = -\frac{\partial}{\partial t}\left[\frac{1}{c^2}\frac{\partial \vec{E}}{\partial t} + \mu_0 \vec{J} + \frac{g_{a\gamma\gamma}}{c}\left(\frac{\partial \phi}{\partial t}\vec{B} + \nabla\phi \times \vec{E}\right)\right] \tag{7.19}$$

to solve this analytically, we make some simplifying assumptions. From the first Maxwell's equation,

$$\nabla \cdot \vec{E} = -g_{a\gamma\gamma} c \nabla\phi \cdot \vec{B} \tag{7.20}$$

where

$$\nabla\phi \cdot \vec{B} = \frac{\partial \phi}{\partial r} B_r + \frac{1}{r}\frac{\partial \phi}{\partial \varphi} B_\varphi \tag{7.21}$$

(and $B_z = 0$ as the magnetic field is transverse, so the component $(\partial\phi/\partial z)B_z$ doesn't exist). We assume that the axion field varies sufficiently slowly as a function of the radial coordinate in the detection fiber, $\partial\phi/\partial r \approx 0$. We also assume that the pump and Stokes driving laser modes have $\ell_p = \ell_S$ so that $\partial\phi/\partial\varphi = 0$. With these assumptions, we have

$$\nabla \cdot \vec{E} = 0 \tag{7.22}$$

now, consider the probe field to have a current density $\vec{J}$, and suppose the fiber has an index of refraction n. Since there are no free charges flowing, $\vec{J}$ is the current density due to the bound charges, $\vec{J} = \partial\vec{P}/\partial t$ where $\vec{P}$ is the polarization of the material. Taking the linear term, $\vec{P} = \epsilon_0 \chi_e \vec{E}$. The index of refraction is $n = \sqrt{1 + \chi_e}$ and $c = 1/\sqrt{\mu_0 \epsilon_0}$.

Using all of this, we have

$$
\begin{aligned}
\frac{1}{c^2}\frac{\partial \vec{E}}{\partial t} + \mu_0 \vec{J} &= \mu_0\epsilon_0 \frac{\partial \vec{E}}{\partial t} + \mu_0 \frac{\partial \vec{P}}{\partial t} \\
&= \mu_0\epsilon_0 \frac{\partial \vec{E}}{\partial t} + \mu_0\epsilon_0\chi_e \frac{\partial \vec{E}}{\partial t} \\
&= \mu_0\epsilon_0(1+\chi_e)\frac{\partial \vec{E}}{\partial t} \\
&= \frac{n^2}{c^2}\frac{\partial \vec{E}}{\partial t}
\end{aligned} \tag{7.23}
$$

with these modifications, Eq. (7.19) becomes:

$$
\nabla^2 \vec{E} = \frac{n^2}{c^2}\frac{\partial^2 \vec{E}}{\partial t^2} + \frac{g_{a\gamma\gamma}}{c}\left[\frac{\partial^2 \phi}{\partial t^2}\vec{B} + \frac{\partial \phi}{\partial t}\frac{\partial \vec{B}}{\partial t} + \frac{\partial}{\partial t}(\nabla\phi \times \vec{E})\right] \tag{7.24}
$$

Consider the last term, $\frac{g_{a\gamma\gamma}}{c}\frac{\partial}{\partial t}(\nabla\phi \times \vec{E})$. The electric field contributing to this term is the mixing field $\vec{E}_M$ (which together with the axion field creates a term at the probe frequency ω_0). For simplicity, we assume the mixing beam is in a fiber mode such that E_M is small and this term is negligible. Then, substituting the interacting fields expressions (7.9) and (7.16) into Eq. (7.24):

$$
\begin{aligned}
&\left[\frac{d^2 u_0}{dr^2} + \frac{1}{r}\frac{du_0}{dr} - \frac{\ell_0^2}{r^2}u_0\right] E_0 \exp(i\ell_0\varphi)\exp[i(\beta_0 z - \omega_0 t)] \\
&+\left[\frac{d^2 E_0}{dz^2} + 2i\beta_0\frac{dE_0}{dz} - \beta_0^2 E_0\right] u_0 \exp(i\ell_0\varphi)\exp[i(\beta_0 z - \omega_0 t)] \\
&= -\frac{n^2}{c^2}\omega_0^2 E_0 u_0 \exp(i\ell_0\varphi)\exp[i(\beta_0 z - \omega_0 t)] \\
&-\frac{g_{a\gamma\gamma}}{c}B_M(\omega_P - \omega_S)^2 u_\phi u_M \exp[i(\ell_P - \ell_S + \ell_M)\varphi]\cdot \\
&\quad \cdot \exp[i(\beta_P - \beta_S + \beta_M)z - i(\omega_P - \omega_S + \omega_M)t] \\
&-\frac{g_{a\gamma\gamma}}{c}B_M(\omega_P - \omega_S)\omega_M u_\phi u_M \exp[i(\ell_P - \ell_S + \ell_M)\varphi]\cdot \\
&\quad \cdot \exp[i(\beta_P - \beta_S + \beta_M)z - i(\omega_P - \omega_S + \omega_M)t]
\end{aligned} \tag{7.25}
$$

we now make a couple of simplifying assumptions: (i) conservation of energy: we assume the frequencies satisfy: $\omega_P - \omega_S + \omega_M = \omega_0$. (ii) conservation of angular momentum: angular momentum numbers satisfy $\ell_P - \ell_S + \ell_M = \ell_0$. (iii) the Slowly Varying Envelope Approximation (SVEA) for the probe beam, $\left|\frac{dE_0}{dz}\right| \ll \beta_0 E_0$. Finally, since without the axion interaction (setting $u_\phi = 0$) the probe wave is a mode of the fiber, we get the following equation for the radial profile:

$$\frac{d^2 u_0}{dr^2} + \frac{1}{r}\frac{du_0}{dr} + \left(\frac{n^2}{c^2}\omega_0^2 E_0 - \beta_0^2 - \frac{\ell_0^2}{r^2}\right) u_0 = 0 \tag{7.26}$$

(here the SVEA makes $|-2i\beta_0 dE_0/dz| \ll |-\beta_0^2 E_0|$ and also $d^2E_0/dz^2 \ll |-2i\beta_0 dE_0/dz|$ therefore we can ignore these terms relative to β_0^2). This allows us to cancel these terms. With these assumptions and simplifications, Eq. (7.25) reduces to:

$$2i\beta_0 \frac{dE_0}{dz} u_0 = -\frac{g_{a\gamma\gamma}}{c}(\omega_P - \omega_S)\omega_0 B_M u_\phi \, u_M \exp[i(\beta_P - \beta_S + \beta_M - \beta_0)z] \tag{7.27}$$

where we dropped d^2E_0/dz^2 again due to the SVEA, and assumed conservation of energy and angular momentum. Finally, to simplify this further, we assume that the probe and mixing beams have similar radial profiles, $u_0(r) \approx u_M(r)$. We also take the radial variation of the axion field over the detection fiber to be negligible, and assume $u_\phi(r) \approx$ constant. Since Eq. (7.15) has dimensionless parameters, then up to a numerical factor, the value of the axion radial field profile is $u_\phi \sim \frac{1}{\kappa^2_{\text{axion}}} \frac{g_{a\gamma\gamma}}{\mu_0 c} E_P B_S^*$. Using these, we get the propagation equation for the probe beam:

$$2i\beta_0 \frac{dE_0}{dz} = -\frac{g^2_{a\gamma\gamma}}{c^2}\frac{1}{\kappa^2_{\text{axion}}}(\omega_P - \omega_S)\omega_0 \left(\frac{1}{\mu_0} B_M B_s^*\right) E_P \exp[i(\beta_P - \beta_S + \beta_M - \beta_0)z] \tag{7.28}$$

In the above expression, the quantity $(\beta_P - \beta_S + \beta_M - \beta_0)z$ is the total phase mismatch of the four-wave mixing interaction. Denoting $\Delta k_{\text{FWM}} \equiv \beta_P - \beta_S + \beta_M - \beta_0$, and $n_{\text{eff}} \equiv \frac{\beta_0}{\omega_0/c}$ as the refractive index of the probe as it propagates through the detection fiber, the differential equation for the probe propagation can be written as

$$\frac{dE_0}{dz} = i\xi E_P \exp(i\Delta k_{\mathrm{FWM}} z) \tag{7.29}$$

where the quantity ξ summarizes the whole interaction,

$$\xi = g_{a\gamma\gamma}^2 \frac{1}{n_{\mathrm{eff}}} \frac{1}{c} \frac{1}{\kappa_{\mathrm{axion}}^2} \left(\frac{1}{2\mu_0} B_M B_S^* \right) (\omega_P - \omega_S) \tag{7.30}$$

Let us establish that ξ is a small number, mainly due to the greatness of κ_{axion}. Considering the parameters in Eq. (7.30), let us assume high-end parameters with a higher-end value of $g_{a\gamma\gamma} \sim 10^{-3}\,\mathrm{GeV}^{-1}$. Suppose that using metamaterials $n_{\mathrm{eff}} \sim 0.01$. Also, taking mass at the lower range of our search $m_a \sim 10^{-6}\,\mathrm{eV}$ we get on the high end that $\kappa_{\mathrm{axion}} = m_a c/\hbar \sim 10^{36}\,\mathrm{m}^{-1}$; Now consider lasers at the higher end intensity suggested in phase 4 of our experiment (see table 7.1). Taking $I_S \sim I_M \sim 10^{15}\,\mathrm{W/m}^2$, we have $E_S \sim E_M \sim 10^8\,\mathrm{V/m}$. Then with $B \sim E/c$, we have $B_M \sim B_S \sim 1\,\mathrm{T}$, $\mu_0 \sim 10^{-6}\,\mathrm{m\,kg\,s^{-2}\,A^{-2}}$, and $\omega_P \sim \omega_S \sim 10^{15}\,\mathrm{rad/s}$ (near-IR $1.55\,\mu\mathrm{m}$ frequencies). Let us take an interaction length in the fiber of $L \approx 1000\,\mathrm{km}$. With these numbers, our (higher-end) approximation is $\xi \sim 10^{-53}$. We will use the smallness of ξ in the derivation of Eq. (7.34) below.

We next focus on the ideal phase-matched case where we assume that the mode wave numbers can be adjusted such that $\Delta k_{\mathrm{FWM}} \to 0$. In this case, the probe propagation equation has a particularly simple form and can be immediately solved:

$$\frac{dE_0}{dz} = i\xi E_P \tag{7.31}$$

$$\Rightarrow E_0(L) = E_0(0) + i\xi E_P L \tag{7.32}$$

Here, L is the total length of each fiber, which is essentially the interaction length. Eq. (7.32) describes the change in the electric field of the probe beam due to the axion interaction. Based on this we will be able to find the change in intensity. Squaring both sides of Eq. (7.32), we get

$$
\begin{aligned}
|E_0(L)|^2 &= \left| E_0(0)\left(1+\frac{i\xi E_P L}{E_0(0)}\right)\right|^2 \\
\therefore \frac{|E_0(L)|^2}{|E_0(0)|^2} &= \left|1+\frac{i\xi\left\{\Re(E_P)+i\Im(E_P)\right\}L}{E_0(0)}\right|^2 \\
\therefore \frac{|E_0(L)|^2}{|E_0(0)|^2} &= \left(1-\frac{\xi\Im(E_P)L}{E_0(0)}\right)^2+\left(\frac{\xi\Re(E_P)L}{E_0(0)}\right)^2 \\
\therefore \frac{|E_0(L)|^2}{|E_0(0)|^2} &= 1-\frac{2\xi\Im(E_P)L}{E_0(0)}+\frac{\xi^2(\Im(E_p))^2L^2}{E_0(0)^2}+\frac{\xi^2(\Re(E_p))^2L^2}{E_0(0)^2}
\end{aligned}
\tag{7.33}
$$

where the symbols $\Re$ and $\Im$ stand for taking the real part and the imaginary part of the term inside the brackets. The last two terms are of order $(\xi L)^2$ and are negligible compared with the first two. Therefore

$$
\frac{|E_0(L)|^2}{|E_0(0)|^2} \approx 1-\frac{2\xi\Im(E_P)L}{E_0(0)} \tag{7.34}
$$

and considering the intensity $I \propto |E^2|$:

$$
\frac{I(L)}{I(0)} = 1-2\xi L\frac{\Im(E_P)}{E_0(0)} \tag{7.35}
$$

Note that by changing the phase of the pump field, E_P, we can change the sign of the quantity $\Im(E_P)$, and thereby control whether the probe beam will experience absorption or amplification due to axion-mediated four-wave mixing interaction. By measuring the change in intensity, we can find the value of ξ, which allows us to put a bound on the coupling constant, as described in the next section.

7.5 Bounds on the coupling constant

We now discuss the bounds that this type of experiment can place on the coupling constant, given specific experimental conditions. The sensitivity of such an experiment will critically depend on the precision in which we can measure the change in the intensity of the probe beam. From Eq. (7.35), the fractional change in intensity is

$$\frac{\Delta I}{I} = \frac{|I(L) - I(0)|}{I(0)} = 2\xi L \frac{\Im(E_P)}{E_0(0)} \tag{7.36}$$

To increase the achievable sensitivity, we apply photon-number squeezing to the probe photons (creating sub-Poissonian light), and indicate the degree of squeezing by the Mandel-Q parameter, denoted as Q_M (see Eq. 2.88). In the absence of other noise sources, and given a total number N of detected probe photons, the shot-noise fluctuations would be of order $\sqrt{N}$, and the sub shot-noise detection sensitivity can be written as

$$\frac{\Delta I}{I} = (1 + Q_M)\frac{\sqrt{N}}{N} = (1 + Q_M)\frac{1}{\sqrt{N}} \tag{7.37}$$

At this point it is important to notice that nonlinear Raman and Brillouin scattering of the mixing beam in the fiber would introduce noise at the probe beam, reducing the sensitivity of the experiment. While Brillouin scattering could be controlled fairly well (see the discussion in section 7.6), Raman scattering will inevitably reduce the experiment sensitivity. To get a rough estimate of this effect, we assume the "worst case scenario" in which the linewidth of the probe laser fully overlaps with the linewidth of the Raman scattering. We assume to first order that the Raman lineshape is flat, and also that each affected probe photon is eliminated (rather than changed in a more general way, for example, a change in phase). To get a sense for the size of this effect, we assume the probe laser linewidth to be $\delta_p \sim 100\,\text{kHz}$, and the Raman scattering linewidth to be $\Gamma \sim 1\,\text{THz}$. Therefore a first order approximation of the power at which mixing beam photons are Raman scattered:

$$P_R \simeq P_M \frac{\delta_p}{\Gamma_R} \sim P_M \frac{100\,\text{kHz}}{1\,\text{THz}} = 10^{-7} P_M \tag{7.38}$$

Now, the number of photons lost in the Raman scattering during a time T:

$$N_R = \frac{P_R T}{\hbar \omega_M} \tag{7.39}$$

where T is the integration time. Let us calculate this numerically for phase 4 of the experiment. For this phase, taking a fiber diameter of $\sim 100\,\mu$m, we have $P_M \sim 7.85 \times 10^6$ W and $P_R \sim 0.785$ W. This corresponds to $N_R \approx 1.98 \times 10^{24}$ photons lost due to Raman scattering (compared with $N_p \sim 2.52 \times 10^{24}$ probe photons, so 78% are lost!). Therefore, we take $N = N_p - N_R \approx 0.54 \times 10^{24}$ as the number of probe beam photons surviving the noise in Eq. (7.37), for phase 4 of the experiment. Now, equating Eqs. (7.36), (7.37) we get:

$$2\xi L \frac{\Im(E_P)}{E_0(0)} = (1 + Q_M)\frac{1}{\sqrt{N}} \tag{7.40}$$

then, since $P \propto E^2$ (where P is the power) and assuming similar mode sizes, we can write:

$$\frac{\Im(E_P)}{E_0(0)} \approx \sqrt{\frac{P_P}{P_0}} \tag{7.41}$$

where P_P is the optical power of the pump laser and P_0 is the optical power of the probe beam. Therefore

$$2\xi L \sqrt{\frac{P_P}{P_0}} = (1 + Q_M)\frac{1}{\sqrt{N}} \tag{7.42}$$

and using the expression for ξ from Eq. (7.30) we get:

$$g^2_{a\gamma\gamma} = (1 + Q_M)\frac{n_{\text{eff}}\kappa^2_{\text{axion}}}{2L(\frac{1}{2\mu_0}B_M B^*_S)\sqrt{N}\sqrt{\frac{P_P}{P_0}}\left(\frac{\omega_P - \omega_S}{c}\right)} \tag{7.43}$$

Finally, we will make the assumption that Δk^2 in expression (7.12) is zero, and also that $(\beta_P - \beta_S) = 0$ which corresponds to an axion having no kinetic energy. Using these simplifying assumptions, $(\omega_P - \omega_S)/c = \kappa_{\text{axion}} = m_a c/\hbar$ and we get

$$g^2_{a\gamma\gamma} = (1 + Q_M)\frac{n_{\text{eff}}\, m_a c}{2\hbar L(\frac{1}{2\mu_0}B_M B^*_S)\sqrt{N}\sqrt{\frac{P_P}{P_0}}} \tag{7.44}$$

The quantity $\frac{1}{2\mu_0}B_M B^*_S$ can be thought of as the magnetic energy density. We did

Parameter	Phase-1	Phase-2	Phase-3	Phase-4
Length of the fiber (L)	1 km	10 km	100 km	1000 km
Power in probe (P_0)	1 mW	10 mW	100 mW	1 W
Integration time (T)	100 s	10^3 s	10^4 s	10^6 s
Power in pump (P_P)	1 W	10 W	100 W	10 kW
Intensity of Stokes (I_S)	$0.1\,\mathrm{GW/cm^2}$	$1\,\mathrm{GW/cm^2}$	$10\,\mathrm{GW/cm^2}$	$100\,\mathrm{GW/cm^2}$
Intensity of mixing (I_M)	$0.1\,\mathrm{GW/cm^2}$	$1\,\mathrm{GW/cm^2}$	$10\,\mathrm{GW/cm^2}$	$100\,\mathrm{GW/cm^2}$
Probe refractive index (n_{eff})	1	10^{-1}	10^{-2}	10^{-4}
Squeezing of probe (dB)	0 dB	3 dB	6 dB	12 dB

Table 7.1: The set of parameters that are used for the four envisioned phases of the experiment.

the above calculation assuming $\Delta k_{\mathrm{FWM}} = 0$. For a finite Δk_{FWM}, the sensitivity of the scheme would be reduced, to first order by a factor of $\sim (\Delta k_{\mathrm{FWM}} L)^2$ (see Appendix E). We next evaluate the bounds on the coupling constant for four envisioned phases of the experiment. The parameters that are used in these four phases are given below in Table 7.1. The parameters for the lasers are well within the current state of the art of high-power fiber lasers [58]. We envision that the parameters that are used in the first two phases of the experiment (*phase-1* and *phase-2*) can be achieved in a few years timescale, while the last two phases of the experiment (*phase-3* and *phase-4*) can be performed within the next 5 to 10 years. The calculated bounds for the axion-photon coupling for these four envisioned phases of the experiment are shown in Figure 7.5. The range of axion masses in our plot is motivated by astrophysical constraints of axion dark matter. To put the parameters that are listed in Table 7.1 into perspective, the ALPS II project and IAXO (see sections 6.3.2 and 6.4.3) are shown as dashed lines. The envisioned *phase-4* experiment of our scheme (solid black line) is quite competitive with the planned ALPS II and IAXO experiments.

7.6 Noise and other practical limitations, and ways to improve them

Here we consider the most likely sources of noise, practical challenges and ways to optimize them and improve the system. One main source of noise in the experiment is

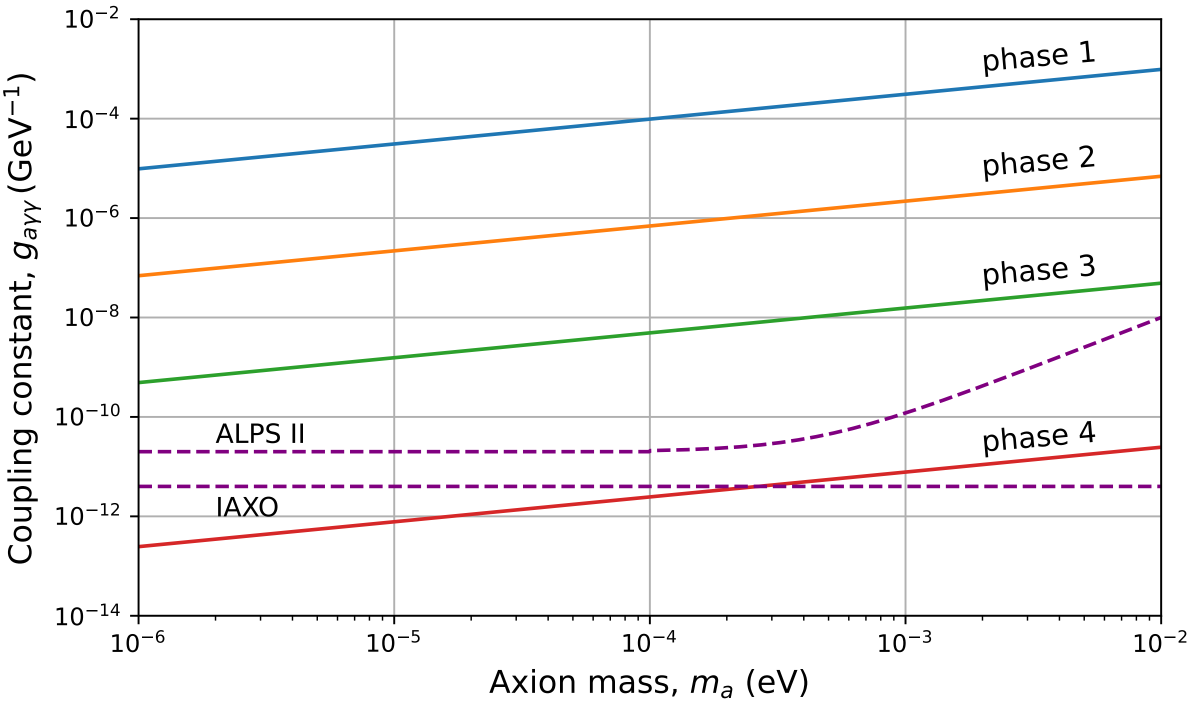

Figure 7.5: The calculated detection sensitivity for the axion-photon coupling constant for four different phases of the experiment. The phase-4 experiment is quite competitive with several planned experiments, such as the next generation LSW experiment (ALPS II) and the next generation solar helioscope (IAXO).

stimulated Raman and Brillouin scatterings of the intense mixing beam, which would affect the probe laser photons. Those are unavoidable at our high laser powers. We have taken Raman scattering into account in the calculation of the sensitivity limits, assuming the "worst case" (but simple to calculate) scenario where every affected probe photon was destroyed. Hollow-core photonic crystals would help reducing this effect since the core is vacuum. This could be used in phases 1 and 2 of the experiment where $n_{\text{eff}} = 1$. For Brillouin scattering, since the scattered photons are propagating backwards, it should be possible to keep them fairly separated from the probe photons, thus minimizing that effect.

Another challenge is related to a destructive interference effect in the generation fiber. To generate axions we relied on the $\vec{E} \cdot \vec{B}$ nonlinearity in the Klein-Gordon equation, and assumed that pump and Stokes beams combine as $E_P B_S^*$. However, another term would contribute at a similar frequency, $B_P E_S^*$, with an opposite sign, creating a destructive interference. Assuming the pump beam to be in the transverse-electric (TE) mode and the Stokes beam to be in the transverse magnetic (TM) mode, the combination is $E_P B_S^* - B_P E_S^*$, which is nonzero considering different refractive indices for the pump and Stokes lasers, n_P and n_S. This can be especially well controlled and optimized by using hybrid modes in sub-wavelength fiber. Those allow for non-orthogonal electric and magnetic field, and one could find the optimized angles to minimize this interference effect. This direction is being numerically investigated by our lab group.

Another possible systematics is leakage of the pump and Stokes laser beams from the generation fiber to the detection fiber. While the axion can easily pass between the two fibers (a fact on which the detection apparatus relies on) and the lasers should not, there would inevitably be little amount of leakage of the optical modes as well. To minimize this effect, we place a metal shield between the two fibers.

Another important effect comes from the index of refraction. To optimize the sensitivity of the experiment, we would ideally want the material to have a low index of refraction for the probe beam, as seen from Eq. (7.44). This is especially true in phases 3 and 4 of the experiment. A possible way to achieve this is to use appropriate metamaterials, such as polaritonic materials, multilayered metamaterials and photonic crystals [59] where the current state of the art at near-IR frequencies is $n \sim 0.01$ [60]. One practical problem of using a low index for the probe is that the mixing beam refractive index should not be as low since it would result in losses. At the higher end of our envisioned axion mass range of $\sim 10^{-2}\,\mathrm{eV}$ the frequency separation between the two beams is high enough and such a separation of refraction index is feasible. At the lower end of $\sim 10^{-6}\,\mathrm{eV}$ it would be harder to get two different indices of refraction, and the mixing beam would experience more loss. Therefore, scanning an axion mass closer to $\sim 10^{-2}\,\mathrm{eV}$ is preferable for this experiment.

Another limitation favoring the higher mass range of our search comes from the resilience of the fiber to bending. The Compton wavelength of the axion is $\lambda_a = h/m_a c$. For masses close to 10^{-6} eV, the wavelength of the axion would be large, requiring a thicker of fiber. Optical fibers with such high radius would be susceptible to breaking as the glass would need to be bent in order to fit a lab facility for the long optical fibers envisioned in this experiment.

An possible improvement in the system could be achieved by integrating a high-finesse cavity with the generation and detection fibers. Using a distributed Bragg reflector at each end of the fiber (which may be achieved by modulating the refractive index over a section near the beginning and the end each fiber), the lasers can be made to bounce back and forth along the fiber, thereby significantly increasing the interaction length. For this case, the sensitivity bounds for the axion-photon coupling constant $g_{a\gamma\gamma}$ would reduce by a factor $\sqrt{F}$, where F is the cavity finesse.

Finally, some attenuation of the beams over distance or loss because of fiber bending is unavoidable. Our beams operate around $\lambda = 1.55\,\mu$m which minimizes beam loss in the fiber. Losses still present can be compensated for by the use of optical repeaters such as an erbium-doped fiber amplifier (EDFA), ensuring that the axiton propagation is least affected.

7.7 Summary and future prospects

We have described an experimental setup based on four-wave mixing of lasers in optical fibers, with the mediation of the axion. The interaction with the axion affects the probe laser's intensity and phase in a measurable way. We assumed photon-number squeezing with sub shot-noise limitation of the experimental sensitivity, also taking into account Raman scattering, though other issues arise as well which reduce the detection sensitivity further, as described in the previous section. Yet, the prospects of this experiment compared to existing and projected ones look promising. Our research group is investigating further improvements. One direction which is investigated is the form of the axion waves (axitons) propagating in the optical fiber. For simplicity we have considered specific modes (TE for the pump and TM for the Stokes). However, other modes might be more advantageous as mentioned in section 7.6, though the calculation could be complicated. For this, using COMSOL Multiphysics, a commercially available software for solving Maxwell's equations including charge and current modifications (such as contributed by the axion) as described for example in [61] and specified boundary conditions as provided by the optical fiber, allows us to solve the equation numerically for more complicated mode functions of the fields, and then investigate the resulting axiton profile solutions.

Appendix A

Analytical calculations of squeezing

In this appendix we include the full analytical calculations for the quadrature squeezing calculations and wave function calculations done under certain conditions

A.1 Exact calculation in a vacuum state

Based on Eqs. (4.1), (4.2) the full Hamiltonian of the system is:

$$\begin{aligned}\hat{H} = \hbar\omega_p \hat{a}^\dagger \hat{a} + \hbar\omega_a \hat{\sigma}^+ \hat{\sigma}^- + i\hbar g_1 \exp\left[-i\left(\omega_{c2} + \Delta_2\right)t\right]\hat{a}^\dagger \hat{\sigma}^- + i\hbar g_2 \exp\left[i\left(\omega_{c1} + \Delta_1\right)t\right]\hat{a}\hat{\sigma}^- \\ - i\hbar g_1^* \exp\left[i\left(\omega_{c2} + \Delta_2\right)t\right]\hat{a}\hat{\sigma}^+ - i\hbar g_2^* \exp\left[-i\left(\omega_{c1} + \Delta_1\right)t\right]\hat{a}^\dagger \hat{\sigma}^+\end{aligned} \tag{A.1}$$

we can use the Heisenberg equation to get the equations of motion. The equation for $\hat{a}$:

$$\begin{aligned}\frac{d\hat{a}}{dt} &= \frac{1}{i\hbar}\left[\hat{a}, \hat{H}\right] \\ &= \frac{1}{i\hbar}\left(\hbar\omega_p \hat{a} + i\hbar g_1 \exp\left[-i\left(\omega_{c2} + \Delta_2\right)t\right]\hat{\sigma}^- - i\hbar g_2^* \exp\left[-i\left(\omega_{c1} + \Delta_1\right)t\right]\hat{\sigma}^+\right) \\ &= -i\omega_p \hat{a} + g_1 \exp\left[-i\left(\omega_{c2} + \Delta_2\right)t\right]\hat{\sigma}^- - g_2^* \exp\left[-i\left(\omega_{c1} + \Delta_1\right)t\right]\hat{\sigma}^+\end{aligned} \tag{A.2}$$

the equation for $\hat{\sigma}$:

$$
\begin{aligned}
\frac{d\hat{\sigma}}{dt} &= \frac{1}{i\hbar}\left[\hat{\sigma},\hat{H}\right] \\
&= \frac{1}{i\hbar}\left(\hbar\omega_a\hat{\sigma}^- + i\hbar g_1^*\exp\left[i\left(\omega_{c2}+\Delta_2\right)t\right]\hat{a}\hat{\sigma}_z + i\hbar g_2^*\exp\left[-i\left(\omega_{c1}+\Delta_1\right)t\right]\hat{a}^\dagger\hat{\sigma}_z\right) \\
&= -i\omega_a\hat{\sigma}^- + g_1^*\exp\left[i\left(\omega_{c2}+\Delta_2\right)t\right]\hat{a}\hat{\sigma}_z + g_2^*\exp\left[-i\left(\omega_{c1}+\Delta_1\right)t\right]\hat{a}^\dagger\hat{\sigma}_z
\end{aligned} \tag{A.3}
$$

looking at them together:

$$
\begin{aligned}
\frac{d\hat{a}}{dt} &= -i\omega_p\hat{a} + g_1\exp\left[-i\left(\omega_{c2}+\Delta_2\right)t\right]\hat{\sigma}^- - g_2^*\exp\left[-i\left(\omega_{c1}+\Delta_1\right)t\right]\hat{\sigma}^+ \\
\frac{d\hat{\sigma}}{dt} &= -i\omega_a\hat{\sigma}_z\hat{\sigma}^- + g_1^*\exp\left[i\left(\omega_{c2}+\Delta_2\right)t\right]\hat{a}\hat{\sigma}_z + g_2^*\exp\left[-i\left(\omega_{c1}+\Delta_1\right)t\right]\hat{a}^\dagger\hat{\sigma}_z
\end{aligned} \tag{A.4}
$$

now, to get rid of the first term on the RHS, define

$$
\begin{aligned}
\hat{a} &\equiv \tilde{\hat{a}}\exp\left(-i\omega_p t\right) \\
\hat{\sigma} &\equiv \hat{\sigma}_z\tilde{\hat{\sigma}}\exp\left(-i\omega_a t\right)
\end{aligned} \tag{A.5}
$$

substitution gives

$$
\begin{aligned}
\frac{d\tilde{\hat{a}}}{dt} &= g_1\exp\left[-i\left(\omega_{c2}+\Delta_2-\omega_p+\omega_a\right)t\right]\tilde{\hat{\sigma}}^- - g_2^*\exp\left[-i\left(\omega_{c1}+\Delta_1-\omega_p-\omega_a\right)t\right]\tilde{\hat{\sigma}}^+ \\
\hat{\sigma}_z\frac{d\tilde{\hat{\sigma}}}{dt} &= g_1^*\exp\left[i\left(\omega_{c2}+\Delta_2-\omega_p+\omega_a\right)t\right]\hat{a}\hat{\sigma}_z + g_2^*\exp\left[-i\left(\omega_{c1}+\Delta_1-\omega_p-\omega_a\right)t\right]\hat{a}^\dagger\hat{\sigma}_z
\end{aligned} \tag{A.6}
$$

we can multiply the second equation by $\hat{\sigma}_z^{-1}$ and define

$$
\begin{aligned}
\omega_{c1}+\Delta_1-\omega_p-\omega_a &\equiv \delta\omega_1 \\
\omega_{c2}+\Delta_2-\omega_p+\omega_a &\equiv \delta\omega_2
\end{aligned} \tag{A.7}
$$

so that the equations become

$$\begin{aligned}\frac{d\tilde{\hat{a}}}{dt} &= g_1 \exp\left(-i\delta\omega_2 t\right)\tilde{\hat{\sigma}}^- - g_2^* \exp\left(-i\delta\omega_1 t\right)\tilde{\hat{\sigma}}^+ \\ \frac{d\tilde{\hat{\sigma}}}{dt} &= g_1^* \exp\left(i\delta\omega_2 t\right)\tilde{\hat{a}} + g_2^* \exp\left(-i\delta\omega_1 t\right)\tilde{\hat{a}}^\dagger\end{aligned} \tag{A.8}$$

to proceed, assume that $\tilde{\hat{a}}$, $\tilde{\hat{a}}^+$ vary much slower than $\exp(i\delta\omega_1 t)$ **and** $\exp(i\delta\omega_2 t)$. Then from the second equation:

$$\tilde{\hat{\sigma}}\left(t\right) = \frac{g_1^*}{i\delta\omega_2}\exp\left(i\delta\omega_2 t\right)\tilde{\hat{a}} - \frac{g_2^*}{i\delta\omega_1}\exp\left(-i\delta\omega_1 t\right)\tilde{\hat{a}}^\dagger \tag{A.9}$$

substituting this in the first equation,

$$\begin{aligned}\frac{d\tilde{\hat{a}}}{dt} &= g_1 \exp\left(-i\delta\omega_2 t\right)\left[\frac{g_1^*}{i\delta\omega_2}\exp\left(i\delta\omega_2 t\right)\tilde{\hat{a}} - \frac{g_2}{i\delta\omega_1}^* \exp\left(-i\delta\omega_1 t\right)\tilde{\hat{a}}^\dagger\right] \\ &\quad - g_2^* \exp\left(-i\delta\omega_1 t\right)\left[-\frac{g_1}{i\delta\omega_2}\exp\left(-i\delta\omega_2 t\right)\tilde{\hat{a}}^\dagger + \frac{g_2}{i\delta\omega_1}\exp\left(i\delta\omega_1 t\right)\tilde{\hat{a}}\right]\end{aligned} \tag{A.10}$$

or

$$\frac{d\tilde{\hat{a}}}{dt} = \frac{\left|g_1\right|^2}{i\delta\omega_2}\tilde{\hat{a}} - \frac{g_1 g_2^*}{i\delta\omega_1}\exp\left[-i\left(\delta\omega_1+\delta\omega_2\right)t\right]\tilde{\hat{a}}^\dagger + \frac{g_1 g_2^*}{i\delta\omega_2}\exp\left[-i\left(\delta\omega_1+\delta\omega_2\right)t\right]\tilde{\hat{a}}^\dagger - \frac{\left|g_2\right|^2}{i\delta\omega_1}\tilde{\hat{a}} \tag{A.11}$$

and therefore

$$\frac{d\tilde{\hat{a}}}{dt} = -i\left(\frac{\left|g_1\right|^2}{\delta\omega_2} - \frac{\left|g_2\right|^2}{\delta\omega_1}\right)\tilde{\hat{a}} + i g_1 g_2^*\left(\frac{1}{\delta\omega_1} - \frac{1}{\delta\omega_2}\right)\exp\left[-i\left(\delta\omega_1+\delta\omega_2\right)t\right]\tilde{\hat{a}}^\dagger \tag{A.12}$$

Now let's calculate the quadratures. Defining $\hat{Q} = \hat{a} + \hat{a}^\dagger$, we have

$$\frac{d\hat{Q}}{dt} = \frac{d\hat{a}}{dt} + \frac{d\hat{a}^\dagger}{dt} \tag{A.13}$$

and using the fact that

$$\begin{aligned} \frac{d\hat{a}}{dt} &= \frac{d}{dt}\left[\tilde{\hat{a}}\exp\left(-i\omega_p t\right)\right] = \left(\frac{d\tilde{\hat{a}}}{dt} - i\omega_p\tilde{\hat{a}}\right)\exp\left(-i\omega_p t\right) \\ \frac{d\hat{a}^\dagger}{dt} &= \frac{d}{dt}\left[\tilde{\hat{a}}^\dagger\exp\left(i\omega_p t\right)\right] = \left(\frac{d\tilde{\hat{a}}^\dagger}{dt} + i\omega_p\tilde{\hat{a}}^\dagger\right)\exp\left(i\omega_p t\right) \end{aligned} \tag{A.14}$$

we have

$$\frac{d\hat{Q}}{dt} = \exp\left(-i\omega_p t\right)\frac{d\tilde{\hat{a}}}{dt} + \exp\left(i\omega_p t\right)\frac{d\tilde{\hat{a}}^\dagger}{dt} - i\omega_p\exp\left(-i\omega_p t\right)\tilde{\hat{a}} + i\omega_p\exp\left(i\omega_p t\right)\tilde{\hat{a}}^\dagger \tag{A.15}$$

now we use Eq. (A.12) to express this using $\tilde{\hat{a}}$ and $\tilde{\hat{a}}^\dagger$:

$$\begin{aligned} \frac{d\hat{Q}}{dt} &= \exp\left(-i\omega_p t\right)\left[-i\left(\frac{|g_1|^2}{\delta\omega_2} - \frac{|g_2|^2}{\delta\omega_1}\right)\tilde{\hat{a}} + ig_1g_2^*\left(\frac{1}{\delta\omega_1} - \frac{1}{\delta\omega_2}\right)\exp\left[-i\left(\delta\omega_1+\delta\omega_2\right)t\right]\tilde{\hat{a}}^\dagger\right] \\ &+ \exp\left(i\omega_p t\right)\left[i\left(\frac{|g_1|^2}{\delta\omega_2} - \frac{|g_2|^2}{\delta\omega_1}\right)\tilde{\hat{a}}^\dagger - ig_1^*g_2\left(\frac{1}{\delta\omega_1} - \frac{1}{\delta\omega_2}\right)\exp\left[i\left(\delta\omega_1+\delta\omega_2\right)t\right]\tilde{\hat{a}}\right] \\ &- i\omega_p\exp\left(-i\omega_p t\right)\tilde{\hat{a}} + i\omega_p\exp\left(i\omega_p t\right)\tilde{\hat{a}}^\dagger \end{aligned} \tag{A.16}$$

or, finally

$$\begin{aligned} \frac{d\hat{Q}}{dt} = &\left\{-i\left(\frac{|g_1|^2}{\delta\omega_2} - \frac{|g_2|^2}{\delta\omega_1} + \omega_p\right)\exp\left(-i\omega_p t\right)\right. \\ &\left. -ig_1^*g_2\left(\frac{1}{\delta\omega_1} - \frac{1}{\delta\omega_2}\right)\exp\left[i\left(\delta\omega_1+\delta\omega_2\right)t\right]\exp\left(i\omega_p t\right)\right\}\tilde{\hat{a}} \\ &+\left\{i\left(\frac{|g_1|^2}{\delta\omega_2} - \frac{|g_2|^2}{\delta\omega_1} + \omega_p\right)\exp\left(i\omega_p t\right)\right. \\ &\left. +ig_1g_2^*\left(\frac{1}{\delta\omega_1} - \frac{1}{\delta\omega_2}\right)\exp\left[-i\left(\delta\omega_1+\delta\omega_2\right)t\right]\exp\left(-i\omega_p t\right)\right\}\tilde{\hat{a}}^\dagger \end{aligned} \tag{A.17}$$

Now, since

$$\hat{Q}^2 = \left(\hat{a} + \hat{a}^\dagger\right)^2 = \hat{a}^2 + \hat{a}\hat{a}^\dagger + \hat{a}^\dagger\hat{a} + \hat{a}^{\dagger^2} \tag{A.18}$$

we have

$$\begin{aligned}\frac{d\left(\hat{Q}^2\right)}{dt} &= \hat{a}\,\frac{d\hat{a}}{dt} + \frac{d\hat{a}}{dt}\hat{a} + \hat{a}\frac{d\hat{\hat{a}^\dagger}}{dt} + \frac{d\hat{a}}{dt}\hat{a}^\dagger + \frac{d\hat{a}^\dagger}{dt}\hat{a} + \hat{a}^\dagger\frac{d\hat{a}}{dt} + \frac{d\hat{a}^\dagger}{dt}\hat{a} + \hat{a}^\dagger\frac{d\hat{a}^\dagger}{dt} + \frac{d\hat{a}^\dagger}{dt}\hat{a}^\dagger \\ &= \left(\hat{a} + \hat{a}^\dagger\right)\frac{d\hat{a}}{dt} + \left(\hat{a} + \hat{a}^\dagger\right)\frac{d\hat{a}^\dagger}{dt} + \frac{d\hat{a}}{dt}\left(\hat{a} + \hat{a}^\dagger\right) + \frac{d\hat{a}^\dagger}{dt}\left(\hat{a} + \hat{a}^\dagger\right)\end{aligned} \tag{A.19}$$

therefore

$$\begin{aligned}\frac{d\left(\hat{Q}^2\right)}{dt} &= \left(\tilde{\hat{a}}\exp\left(-2i\omega_p t\right) + \tilde{\hat{a}}^\dagger\right)\left(\frac{d\tilde{\hat{a}}}{dt} - i\omega_p\tilde{\hat{a}}\right) \\ &+ \left(\tilde{\hat{a}} + \tilde{\hat{a}}^\dagger\exp\left(2i\omega_p t\right)\right)\left(\frac{d\tilde{\hat{a}}^\dagger}{dt} + i\omega_p\tilde{\hat{a}}^\dagger\right) \\ &+ \left(\frac{d\tilde{\hat{a}}}{dt} - i\omega_p\tilde{\hat{a}}\right)\left(\tilde{\hat{a}}\exp\left(-2i\omega_p t\right) + \tilde{\hat{a}}^\dagger\right) \\ &+ \left(\frac{d\tilde{\hat{a}}^\dagger}{dt} + i\omega_p\tilde{\hat{a}}^\dagger\right)\left(\tilde{\hat{a}} + \tilde{\hat{a}}^\dagger\exp\left(2i\omega_p t\right)\right)\end{aligned} \tag{A.20}$$

From this,

$$\begin{aligned}\frac{d\left(\hat{Q}^2\right)}{dt} &= \exp\left(-2i\omega_p t\right)\tilde{\hat{a}}\frac{d\tilde{\hat{a}}}{dt} - i\omega_p\exp\left(-2i\omega_p t\right)\tilde{\hat{a}}^2 + \tilde{\hat{a}}^\dagger\frac{d\tilde{\hat{a}}}{dt} \\ &+ \tilde{\hat{a}}\frac{d\tilde{\hat{a}}^\dagger}{dt} + \exp\left(2i\omega_p t\right)\tilde{\hat{a}}^\dagger\frac{d\tilde{\hat{a}}^\dagger}{dt} + 2i\omega_p\exp\left(2i\omega_p t\right)\tilde{\hat{a}}^{\dagger 2} \\ &+ \exp\left(-2i\omega_p t\right)\frac{d\tilde{\hat{a}}}{dt}\tilde{\hat{a}} + \frac{d\tilde{\hat{a}}}{dt}\tilde{\hat{a}}^\dagger - i\omega_p\exp\left(-2i\omega_p t\right)\tilde{\hat{a}}^2 \\ &+ \frac{d\tilde{\hat{a}}^\dagger}{dt}\tilde{\hat{a}} + \exp\left(2i\omega_p t\right)\frac{d\tilde{\hat{a}}^\dagger}{dt}\tilde{\hat{a}}^\dagger\end{aligned} \tag{A.21}$$

the first line in Eq. (A.21) gives

$$
\begin{aligned}
T_1 &= \exp\left(-2i\omega_p t\right)\tilde{\tilde{a}}\frac{d\tilde{\tilde{a}}}{dt} - i\omega_p \exp\left(-2i\omega_p t\right)\tilde{\tilde{a}}^2 + \tilde{\tilde{a}}^\dagger \frac{d\tilde{\tilde{a}}}{dt} \\
&= \exp\left(-2i\omega_p t\right)\tilde{\tilde{a}}\left[-i\left(\frac{|g_1|^2}{\delta\omega_2} - \frac{|g_2|^2}{\delta\omega_1}\right)\tilde{\tilde{a}}\right. \\
&\left. + ig_1g_2^*\left(\frac{1}{\delta\omega_1} - \frac{1}{\delta\omega_2}\right)\exp\left[-i\left(\delta\omega_1+\delta\omega_2\right)t\right]\,\tilde{\tilde{a}}^\dagger\right] \\
&- i\omega_p \exp\left(-2i\omega_p t\right)\tilde{\tilde{a}}^2 + \tilde{\tilde{a}}^\dagger\left[-i\left(\frac{|g_1|^2}{\delta\omega_2} - \frac{|g_2|^2}{\delta\omega_1}\right)\tilde{\tilde{a}}\right. \\
&\left. + ig_1g_2^*\left(\frac{1}{\delta\omega_1} - \frac{1}{\delta\omega_2}\right)\exp\left[-i\left(\delta\omega_1+\delta\omega_2\right)t\right]\,\tilde{\tilde{a}}^\dagger\right] \\
&= -i\left(\frac{|g_1|^2}{\delta\omega_2} - \frac{|g_2|^2}{\delta\omega_1} + \omega_p\right)\exp\left(-2i\omega_p t\right)\tilde{\tilde{a}}^2 \\
&+ ig_1g_2^*\left(\frac{1}{\delta\omega_1} - \frac{1}{\delta\omega_2}\right)\exp\left(-2i\omega_p t\right)\exp\left[-i\left(\delta\omega_1+\delta\omega_2\right)t\right]\tilde{\tilde{a}}\tilde{\tilde{a}}^\dagger \\
&- i\left(\frac{|g_1|^2}{\delta\omega_2} - \frac{|g_2|^2}{\delta\omega_1}\right)\tilde{\tilde{a}}^\dagger\tilde{\tilde{a}} + ig_1g_2^*\left(\frac{1}{\delta\omega_1} - \frac{1}{\delta\omega_2}\right)\exp\left[-i\left(\delta\omega_1+\delta\omega_2\right)t\right]\,\tilde{\tilde{a}}^{\dagger 2}
\end{aligned}
\tag{A.22}
$$

the second line in Eq. $(A.21)$ gives

$$
\begin{aligned}
T_2 &= \tilde{\tilde{a}}\frac{d\tilde{\tilde{a}}^\dagger}{dt} + \exp\left(2i\omega_p t\right)\tilde{\tilde{a}}^\dagger\frac{d\tilde{\tilde{a}}^\dagger}{dt} + i\omega_p\exp\left(2i\omega_p t\right)\tilde{\tilde{a}}^{\dagger 2} \\
&= \tilde{\tilde{a}}\left[i\left(\frac{|g_1|^2}{\delta\omega_2} - \frac{|g_2|^2}{\delta\omega_1}\right)\tilde{\tilde{a}}^\dagger - ig_1^*g_2\left(\frac{1}{\delta\omega_1} - \frac{1}{\delta\omega_2}\right)\exp\left[i\left(\delta\omega_1+\delta\omega_2\right)t\right]\,\tilde{\tilde{a}}\right] \\
&+ \exp\left(2i\omega_p t\right)\tilde{\tilde{a}}^\dagger\left[i\left(\frac{|g_1|^2}{\delta\omega_2} - \frac{|g_2|^2}{\delta\omega_1}\right)\tilde{\tilde{a}}^\dagger - ig_1^*g_2\left(\frac{1}{\delta\omega_1} - \frac{1}{\delta\omega_2}\right)\exp\left[i\left(\delta\omega_1+\delta\omega_2\right)t\right]\,\tilde{\tilde{a}}\right] \\
&+ i\omega_p\exp\left(2i\omega_p t\right)\tilde{\tilde{a}}^{\dagger 2} \\
&= i\left(\frac{|g_1|^2}{\delta\omega_2} - \frac{|g_2|^2}{\delta\omega_1}\right)\tilde{\tilde{a}}\tilde{\tilde{a}}^\dagger - ig_1^*g_2\left(\frac{1}{\delta\omega_1} - \frac{1}{\delta\omega_2}\right)\exp\left[i\left(\delta\omega_1+\delta\omega_2\right)t\right]\,\tilde{\tilde{a}}^2 \\
&+ i\left(\frac{|g_1|^2}{\delta\omega_2} - \frac{|g_2|^2}{\delta\omega_1}\right)\exp\left(2i\omega_p t\right)\tilde{\tilde{a}}^{\dagger 2} \\
&- ig_1^*g_2\left(\frac{1}{\delta\omega_1} - \frac{1}{\delta\omega_2}\right)\exp\left(2i\omega_p t\right)\exp\left[i\left(\delta\omega_1+\delta\omega_2\right)t\right]\tilde{\tilde{a}}^\dagger\tilde{\tilde{a}}
\end{aligned}
\tag{A.23}
$$

the third line in Eq. (A.21) gives:

$$
\begin{aligned}
T_3 &= \exp\left(-2i\omega_p t\right) \frac{d\tilde{\hat{a}}}{dt}\tilde{\hat{a}} + \frac{d\tilde{\hat{a}}}{dt}\tilde{\hat{a}}^{\dagger} - i\omega_p \exp\left(-2i\omega_p t\right)\tilde{\hat{a}}^2 \\
&= \exp\left(-2i\omega_p t\right)\left[-i\left(\frac{|g_1|^2}{\delta\omega_2} - \frac{|g_2|^2}{\delta\omega_1}\right)\tilde{\hat{a}}\right. \\
&\left. + ig_1 g_2^* \left(\frac{1}{\delta\omega_1} - \frac{1}{\delta\omega_2}\right)\exp\left[-i\left(\delta\omega_1 + \delta\omega_2\right)t\right]\ \tilde{\hat{a}}^{\dagger}\right]\tilde{\hat{a}} \\
&- i\left(\frac{|g_1|^2}{\delta\omega_2} - \frac{|g_2|^2}{\delta\omega_1}\right)\tilde{\hat{a}}\tilde{\hat{a}}^{\dagger} + ig_1 g_2^*\left(\frac{1}{\delta\omega_1} - \frac{1}{\delta\omega_2}\right)\exp\left[-i\left(\delta\omega_1 + \delta\omega_2\right)t\right]\ \tilde{\hat{a}}^{\dagger 2} \\
&- i\omega_p \exp\left(-2i\omega_p t\right)\tilde{\hat{a}}^2 \\
&= -i\left(\frac{|g_1|^2}{\delta\omega_2} - \frac{|g_2|^2}{\delta\omega_1}\right)\exp\left(-2i\omega_p t\right)\tilde{\hat{a}}^2 \\
&+ ig_1 g_2^*\left(\frac{1}{\delta\omega_1} - \frac{1}{\delta\omega_2}\right)\exp\left(-2i\omega_p t\right)\exp\left[-i\left(\delta\omega_1 + \delta\omega_2\right)t\right]\tilde{\hat{a}}^{\dagger}\tilde{\hat{a}} \\
&- i\left(\frac{|g_1|^2}{\delta\omega_2} - \frac{|g_2|^2}{\delta\omega_1}\right)\tilde{\hat{a}}\tilde{\hat{a}}^{\dagger} + ig_1 g_2^*\left(\frac{1}{\delta\omega_1} - \frac{1}{\delta\omega_2}\right)\exp\left[-i\left(\delta\omega_1 + \delta\omega_2\right)t\right]\ \tilde{\hat{a}}^{\dagger 2}
\end{aligned} \tag{A.24}
$$

and the fourth line in Eq. (A.21) gives:

$$
\begin{aligned}
T_4 &= \frac{d\tilde{\hat{a}}^{\dagger}}{dt}\tilde{\hat{a}} + \exp\left(2i\omega_p t\right)\frac{d\tilde{\hat{a}}^{\dagger}}{dt}\tilde{\hat{a}}^{\dagger} \\
&= i\left(\frac{|g_1|^2}{\delta\omega_2} - \frac{|g_2|^2}{\delta\omega_1}\right)\tilde{\hat{a}}^{\dagger}\tilde{\hat{a}} - ig_1^* g_2\left(\frac{1}{\delta\omega_1} - \frac{1}{\delta\omega_2}\right)\exp\left[i\left(\delta\omega_1 + \delta\omega_2\right)t\right]\ \tilde{\hat{a}}^2 \\
&+ i\exp\left(2i\omega_p t\right)\left(\frac{|g_1|^2}{\delta\omega_2} - \frac{|g_2|^2}{\delta\omega_1}\right)\tilde{\hat{a}}^{\dagger 2} \\
&- ig_1^* g_2\left(\frac{1}{\delta\omega_1} - \frac{1}{\delta\omega_2}\right)\exp\left(2i\omega_p t\right)\exp\left[i\left(\delta\omega_1 + \delta\omega_2\right)t\right]\ \tilde{\hat{a}}\tilde{\hat{a}}^{\dagger}
\end{aligned} \tag{A.25}
$$

adding up the terms $T_1 + T_2 + T_3 + T_4$ we finally get

$$
\begin{aligned}
\frac{d\left(\hat{Q}^2\right)}{dt} = &\left\{-2i\left(\frac{|g_1|^2}{\delta\omega_2}-\frac{|g_2|^2}{\delta\omega_1}\right)\exp\left(-2i\omega_p t\right)\right.\\
&\left.-2i\,g_1^* g_2\left(\frac{1}{\delta\omega_1}-\frac{1}{\delta\omega_2}\right)\exp\left[i\left(\delta\omega_1+\delta\omega_2\right)t\right]\right\}\tilde{\hat{a}}^2\\
&+\left\{2ig_1g_2^*\left(\frac{1}{\delta\omega_1}-\frac{1}{\delta\omega_2}\right)\exp\left[-i\left(\delta\omega_1+\delta\omega_2\right)t\right]\right.\\
&\left.+2i\left(\frac{|g_1|^2}{\delta\omega_2}-\frac{|g_2|^2}{\delta\omega_1}\right)\exp\left(2i\omega_p t\right)\right\}\tilde{\hat{a}}^{\dagger 2}\\
&+\left\{ig_1g_2^*\left(\frac{1}{\delta\omega_1}-\frac{1}{\delta\omega_2}\right)\exp\left(-2i\omega_p t\right)\exp\left[-i\left(\delta\omega_1+\delta\omega_2\right)t\right]\right.\\
&\left.-ig_1^*g_2\left(\frac{1}{\delta\omega_1}-\frac{1}{\delta\omega_2}\right)\exp\left(2i\omega_p t\right)\exp\left[i\left(\delta\omega_1+\delta\omega_2\right)t\right]\right\}\tilde{\hat{a}}^{\dagger}\tilde{\hat{a}}\\
&+\left\{ig_1g_2^*\left(\frac{1}{\delta\omega_1}-\frac{1}{\delta\omega_2}\right)\exp\left(-2i\omega_p t\right)\exp\left[-i\left(\delta\omega_1+\delta\omega_2\right)t\right]\right.\\
&\left.-ig_1^*g_2\left(\frac{1}{\delta\omega_1}-\frac{1}{\delta\omega_2}\right)\exp\left(2i\omega_p t\right)\exp\left[i\left(\delta\omega_1+\delta\omega_2\right)t\right]\right\}\tilde{\hat{a}}\tilde{\hat{a}}^{\dagger}
\end{aligned}
\tag{A.26}
$$

Consider the quadrature we are looking for:

$$
\begin{aligned}
\frac{d}{dt}\langle\Delta\hat{Q}^2\rangle &= \frac{d}{dt}\left(\langle\hat{Q}^2\rangle-\langle\hat{Q}\rangle^2\right)\\
&=\frac{d}{dt}\langle\hat{Q}^2\rangle-\frac{d}{dt}\left(\langle\hat{Q}\rangle^2\right)\\
&=\frac{d}{dt}\langle\hat{Q}^2\rangle-2\langle\hat{Q}\rangle\frac{d\langle\hat{Q}\rangle}{dt}\\
&=\left\langle\frac{d\left(\hat{Q}^2\right)}{dt}\right\rangle-2\langle\hat{Q}\rangle\left\langle\frac{d\hat{Q}}{dt}\right\rangle
\end{aligned}
\tag{A.27}
$$

We now calculate the quadrature squeezing associated with a vacuum state. In such a state,

$$
\langle\hat{Q}\rangle=\langle 0|\hat{Q}|0\rangle=\langle 0|\left(\hat{a}+\hat{a}^\dagger\right)|0\rangle=0 \tag{A.28}
$$

therefore the second term in the $d\langle\Delta\hat{Q}^2\rangle/dt$ expression above vanishes, and we have

$$\frac{d}{dt}\langle\Delta\hat{Q}^2\rangle = \left\langle \frac{d\left(\hat{Q}^2\right)}{dt} \right\rangle \tag{A.29}$$

Using Eq. (A.26) and considering that only the term proportional to $\tilde{\hat{a}}\,\tilde{\hat{a}}^\dagger$ survives in the vacuum expectation value, we get

$$\begin{aligned}\frac{d}{dt}\langle\Delta\hat{Q}^2\rangle = {} & ig_1g_2^*\left(\frac{1}{\delta\omega_1}-\frac{1}{\delta\omega_2}\right)\exp\left[-i\left(\omega_{c1}+\omega_{c2}+\Delta_1+\Delta_2\right)t\right] \\ & - ig_1^*g_2\left(\frac{1}{\delta\omega_1}-\frac{1}{\delta\omega_2}\right)\exp\left[i\left(\omega_{c1}+\omega_{c2}+\Delta_1+\Delta_2\right)t\right]\end{aligned} \tag{A.30}$$

this is easily integrated to give

$$\begin{aligned}\langle\Delta\hat{Q}^2\rangle = {} & -\frac{1}{\left(\omega_{c1}+\omega_{c2}+\Delta_1+\Delta_2\right)}\left(\frac{1}{\delta\omega_1}-\frac{1}{\delta\omega_2}\right)\left(g_1^*g_2\exp\left[i\left(\omega_{c1}+\omega_{c2}+\Delta_1+\Delta_2\right)t\right]\right. \\ & \left.+g_1g_2^*\exp\left[-i\left(\omega_{c1}+\omega_{c2}+\Delta_1+\Delta_2\right)t\right]\right)\end{aligned} \tag{A.31}$$

A.2 Code for perturbative calculation of wave functions

Here we include a code complementing section 4.3.2 for the calculation of the system wave functions.

```
    (* initial conditions: setting the initial values of the wave \
function coefficients, as well as the system parameter values *)


g0 = 1;

g1 = 0;

g2 = 0;

g3 = 0;

g4 = 0;
```

```
g5 = 0;

g6 = 0;


e0 = 0;

e1 = 0;

e2 = 0;

e3 = 0;

e4 = 0;

e5 = 0;

e6 = 0;


wa = 3;

wp = 7;

wc1 = 10;

wc2 = 4;

Delta1 = 0;

Delta2 = 0;

k1 = 0.2;

k2 = 0.1;


(* order to which the perturbation will be calculated *)

PertOrder = 8;


For[j = 0, j < PertOrder, j++,


 (* solving the differential equations for the wave-function \

coefficients, substituting the previous order solution in each \

iteration *)
```

```
sol1 = DSolve[{ cg0'[t] == k2 Exp[I (wc1 + Delta1) t]*e1 ,
   cg0[0] == 1}, cg0[t], t];
sol2 = DSolve[{
   cg1'[t] == -I wp g1 + k1 Exp[-I (wc2 + Delta2) t] e0 +
     k2 Exp[I (wc1 + Delta1) t] Sqrt[2] e2, cg1[0] == 0}, cg1[t],
  t];
sol3 = DSolve[{
   cg2'[t] == -2 I wp g2 + k1 Exp[-I (wc2 + Delta2) t] Sqrt[2] e1 +
     k2 Exp[I (wc1 + Delta1) t] Sqrt[3] e3, cg2[0] == 0}, cg2[t],
  t];
sol4 = DSolve[{cg3'[t] == -3 I wp g3 +
     k1 Exp[-I (wc2 + Delta2) t] Sqrt[3] e2 +
     k2 Exp[I (wc1 + Delta1) t] Sqrt[4] e4 , cg3[0] == 0}, cg3[t], t];
sol5 = DSolve[{cg4'[t] == -4 I wp g1 +
     k1 Exp[-I (wc2 + Delta2) t] Sqrt[4] e3 +
     k2 Exp[I (wc1 + Delta1) t] Sqrt[5] e5, cg4[0] == 0}, cg4[t],
  t];
sol6 = DSolve[{
   cg5'[t] == -5 I wp g1 + k1 Exp[-I (wc2 + Delta2) t] Sqrt[5] e4 +
     k2 Exp[I (wc1 + Delta1) t] Sqrt[6] e6 , cg5[0] == 0}, cg5[t], t];
sol7 = DSolve[{cg6'[t] == -6 I wp g1 +
     k1 Exp[-I (wc2 + Delta2) t] Sqrt[6] e5 , cg6[0] == 0}, cg6[t],
  t];


sol8 = DSolve[{
   ce0'[t] == -I*wa*e0 - Conjugate[k1] Exp[I (wc2 + Delta2) t] g1,
   ce0[0] == 0}, ce0[t], t];
sol9 = DSolve[{
   ce1'[t] == -I wp *e1 - I*wa*e1 -
```

```
    Conjugate[k1] Exp[I (wc2 + Delta2) t] g2 -
    Conjugate[k2] Exp[-I (wc1 + Delta1) t] g0, ce1[0] == 0}, ce1[t],
  t];
sol10 =
 DSolve[{
   ce2'[t] == -2 I wp *e2 - I*wa*e2 -
     Conjugate[k1] Exp[I (wc2 + Delta2) t] Sqrt[3] g3 -
     Conjugate[k2] Exp[-I (wc1 + Delta1) t] Sqrt[2] g1, ce2[0] == 0},
   ce2[t], t];
sol11 =
 DSolve[{
   ce3'[t] == -3 I wp *e3 - I*wa*e3 -
     Conjugate[k1] Exp[I (wc2 + Delta2) t] Sqrt[4] g4 -
     Conjugate[k2] Exp[-I (wc1 + Delta1) t] Sqrt[3] g2, ce3[0] == 0},
   ce3[t], t];
sol12 =
 DSolve[{
   ce4'[t] == -4 I wp *e4 - I*wa*e4 -
     Conjugate[k1] Exp[I (wc2 + Delta2) t] Sqrt[5] g5 -
     Conjugate[k2] Exp[-I (wc1 + Delta1) t] Sqrt[4] g3, ce4[0] == 0},
   ce4[t], t];
sol13 =
 DSolve[{
   ce5'[t] == -5 I wp *e5 - I*wa*e5 -
     Conjugate[k1] Exp[I (wc2 + Delta2) t] Sqrt[6] g6 -
     Conjugate[k2] Exp[-I (wc1 + Delta1) t] Sqrt[5] g4, ce5[0] == 0},
   ce5[t], t];
sol14 =
 DSolve[{
```

```
    ce6'[t] == -6 I wp *e6 - I*wa*e6 -
      Conjugate[k2] Exp[-I (wc1 + Delta1) t] Sqrt[6] g5, ce6[0] == 0},
    ce6[t], t];

 g0 = cg0[t] /. sol1[[1]];
 g1 = cg1[t] /. sol2[[1]];
 g2 = cg2[t] /. sol3[[1]];
 g3 = cg3[t] /. sol4[[1]];
 g4 = cg4[t] /. sol5[[1]];
 g5 = cg5[t] /. sol6[[1]];
 g6 = cg6[t] /. sol7[[1]];

 e0 = ce0[t] /. sol8[[1]];
 e1 = ce1[t] /. sol9[[1]];
 e2 = ce2[t] /. sol10[[1]];
 e3 = ce3[t] /. sol11[[1]];
 e4 = ce4[t] /. sol12[[1]];
 e5 = ce5[t] /. sol13[[1]];
 e6 = ce6[t] /. sol14[[1]];

 solutions =
  FullSimplify[
   List[sol1, sol2, sol3, sol4, sol5, sol6, sol7, sol8, sol9, sol10,
    sol11, sol12, sol13, sol14]];
 ]

ProbExcited = (Abs[e0])^2 + (Abs[e1])^2 + (Abs[e2])^2 + (Abs[
    e3])^2 + (Abs[e4])^2 + (Abs[e5])^2 + (Abs[e6])^2
```

```
ProbGround = (Abs[g0])^2 + (Abs[g1])^2 + (Abs[g2])^2 + (Abs[
    g3])^2 + (Abs[g4])^2 + (Abs[g5])^2 + (Abs[g6])^2
```

Appendix B

Squeezed light, all simulation results

In this chapter we include a comprehensive collection of our simulation results, showing the time evolution of quadrature and photon statistics expectation values, and revealing quadrature and photon-number squeezing of light for specific parameter.

$$g_1 = 0.25, \; g_2 = 1.0$$

$N = 1$ atom

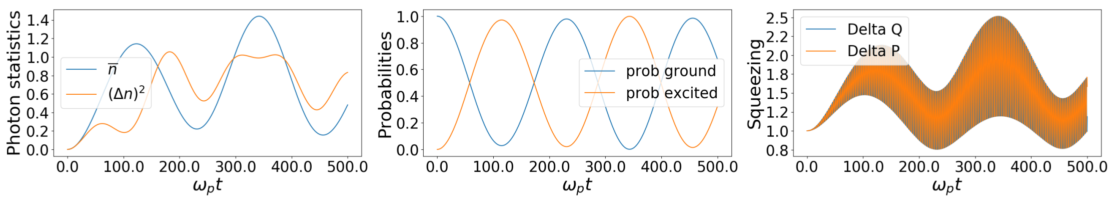

$N = 2$ atoms

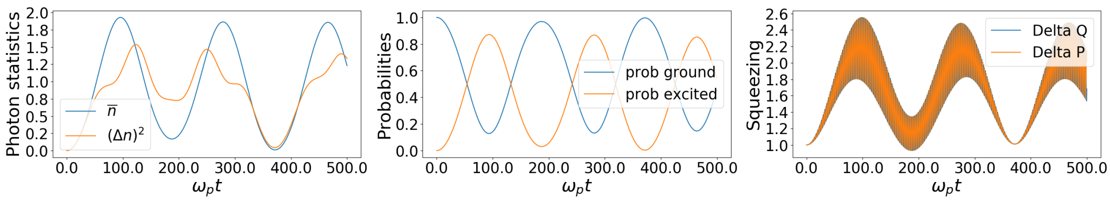

$N = 5$ atoms

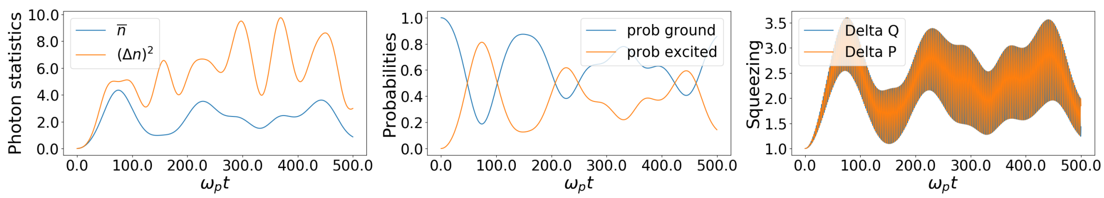

$N = 10$ atoms

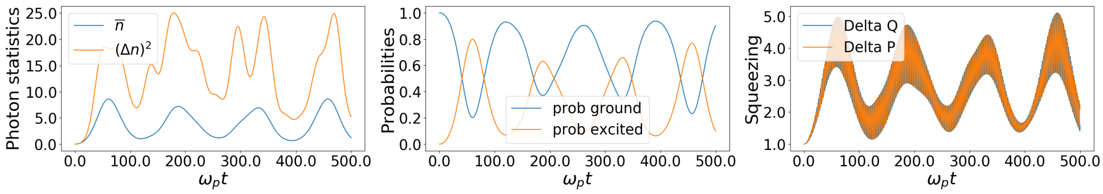

$$g_1 = 0.5, \; g_2 = 1.0$$

$N = 1$ atom

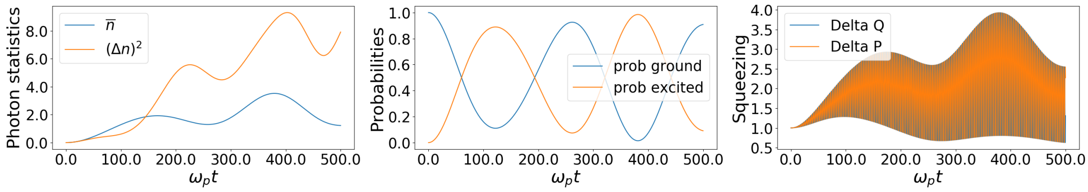

$N = 2$ atoms

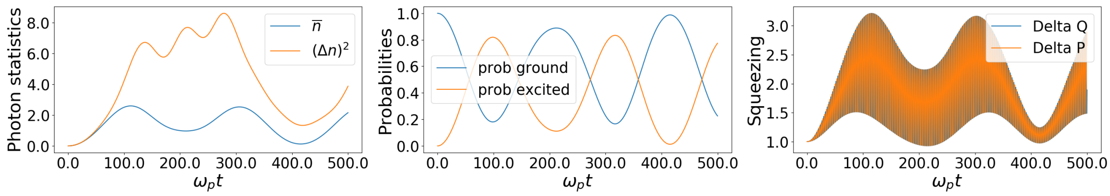

$N = 5$ atoms

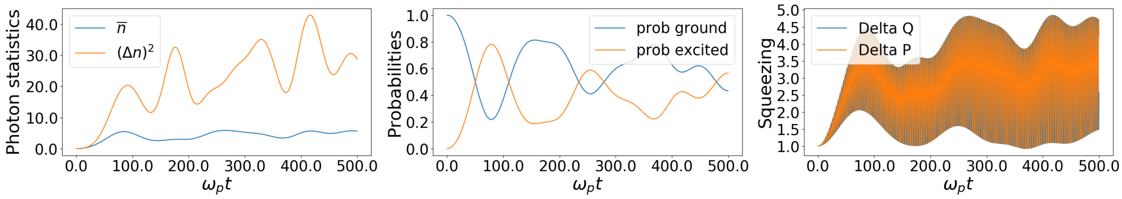

$N = 10$ atoms

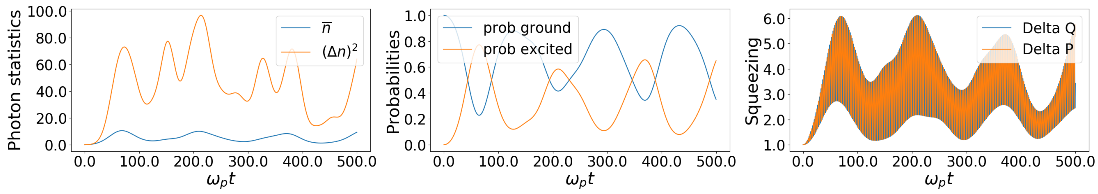

$$g_1 = 0.75, \; g_2 = 1.0$$

$N = 1$ atom

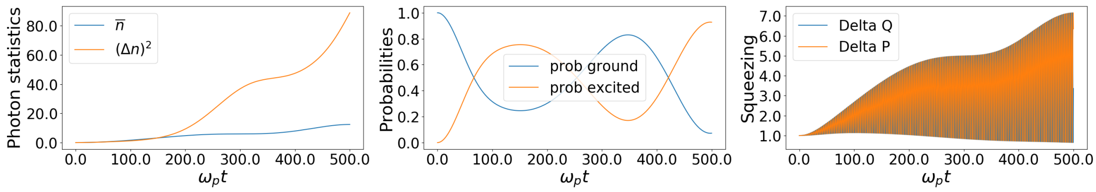

$N = 2$ atoms

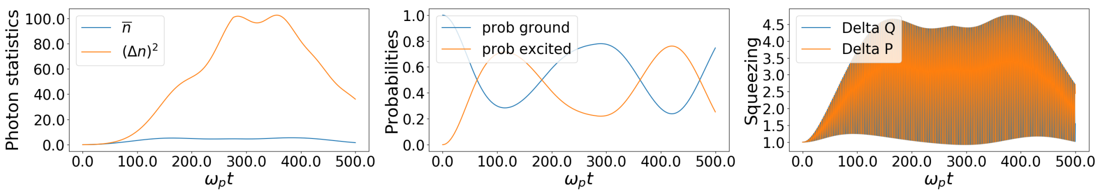

$N = 5$ atoms

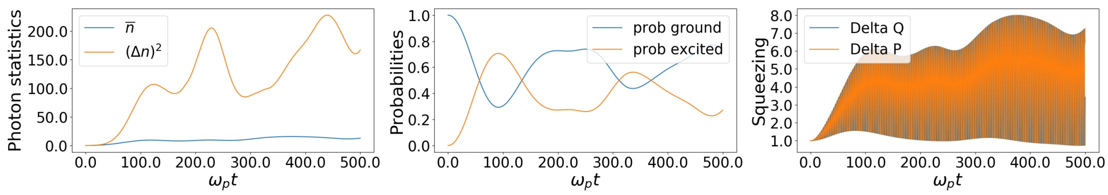

$$g_1 = 1.0, \; g_2 = 1.0$$

$N = 1$ atom

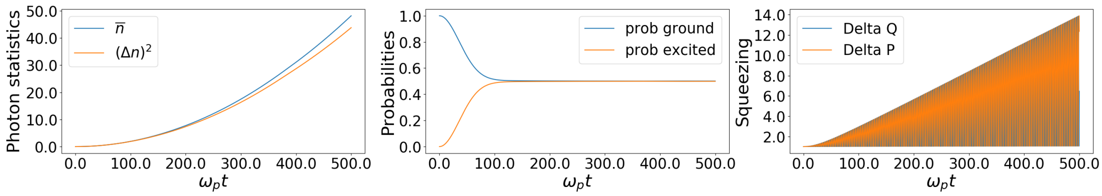

$N = 2$ atoms

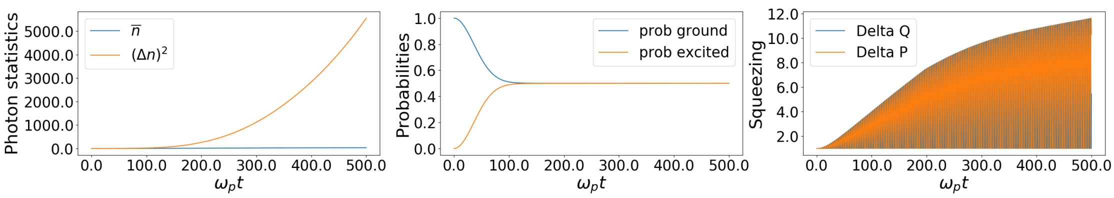

$N = 5$ atoms

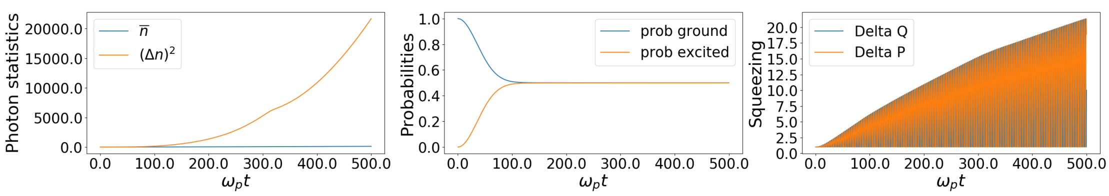

$g_1 = 1.0, \; g_2 = 0.25$

$N = 1$ atom

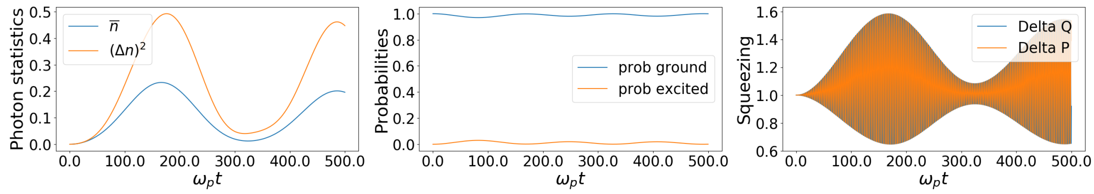

$N = 5$ atoms

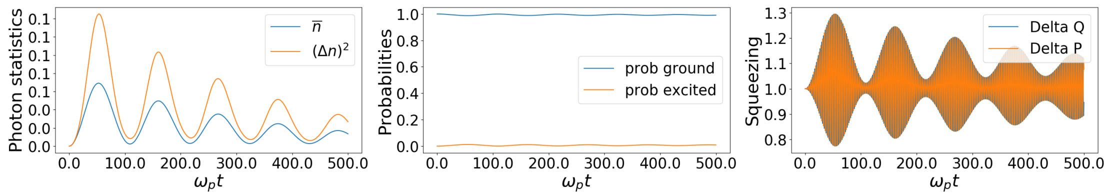

$N = 10$ atoms

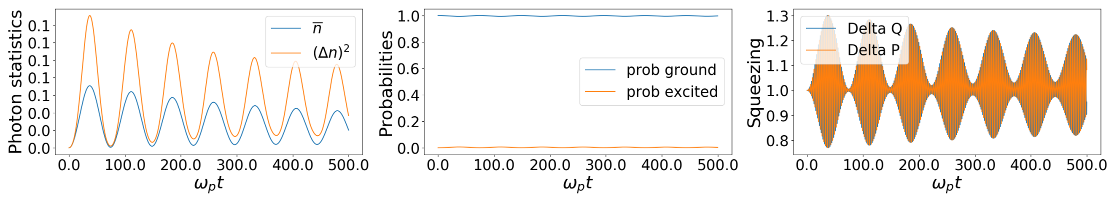

$g_1 = 1.0, \; g_2 = 0.5$

$N = 1$ atom

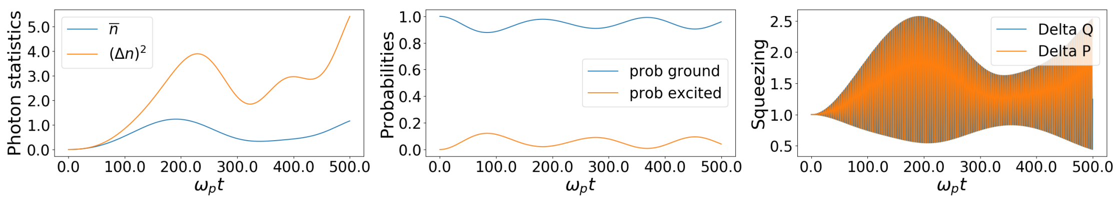

$N = 2$ atoms

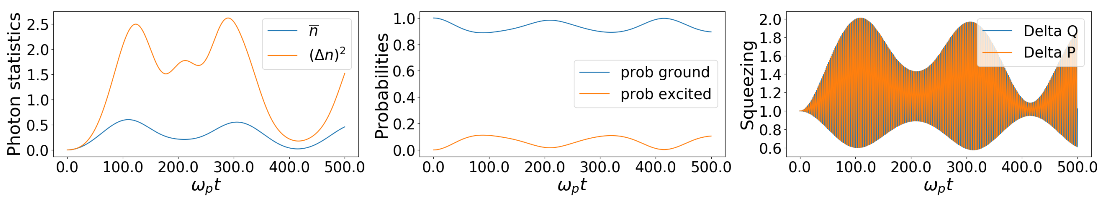

$N = 5$ atoms

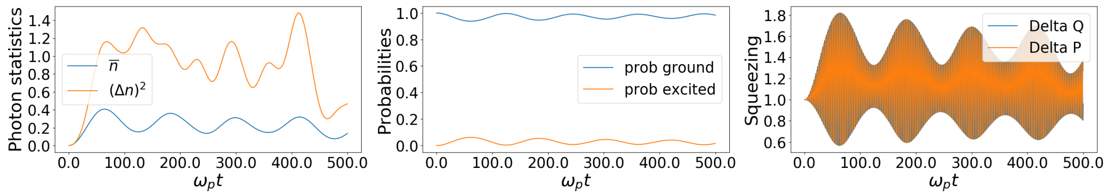

$N = 10$ atoms

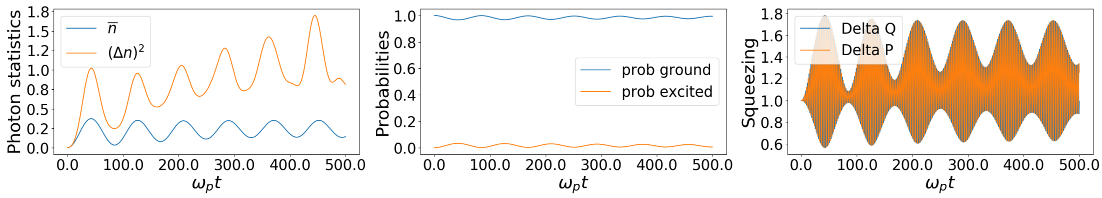

$g_1 = 1.0, \; g_2 = 0.75$

$N = 1$ atom

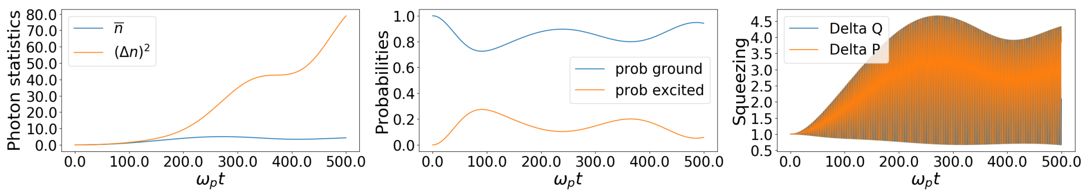

$N = 2$ atoms

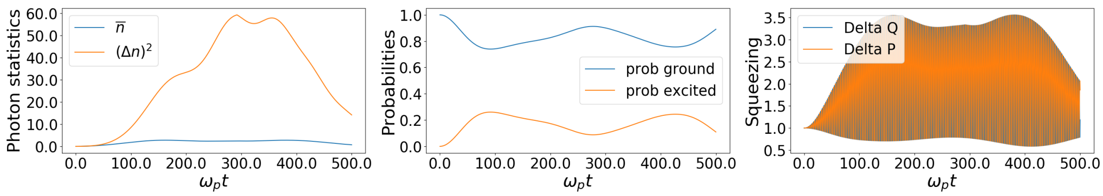

$N = 5$ atoms

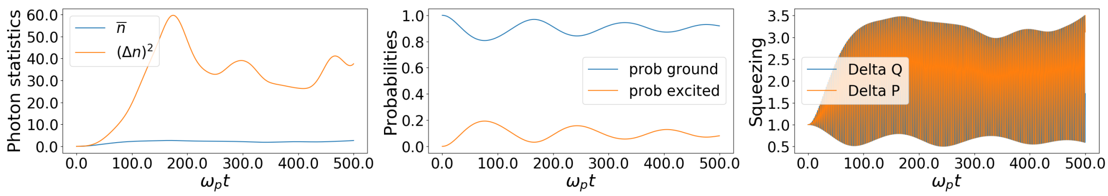

$g_1 = 1.0, \; g_2 = 2.0$

$N = 1$ atom

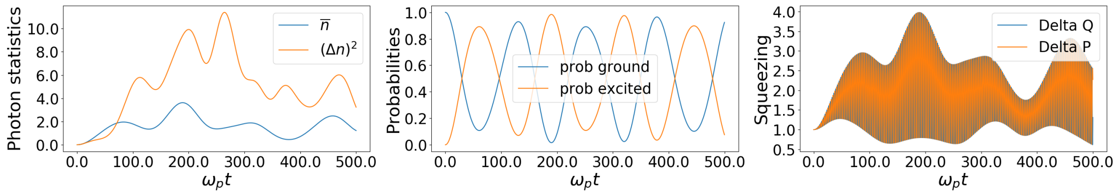

$N = 2$ atoms

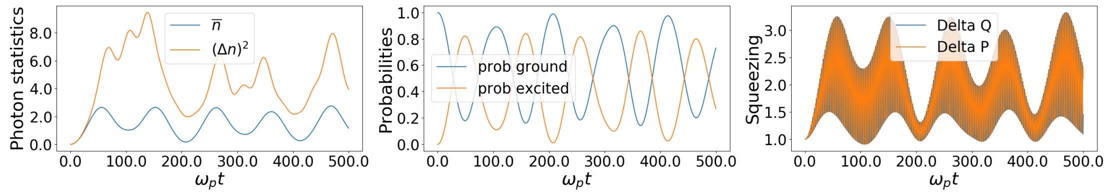

$N = 5$ atoms

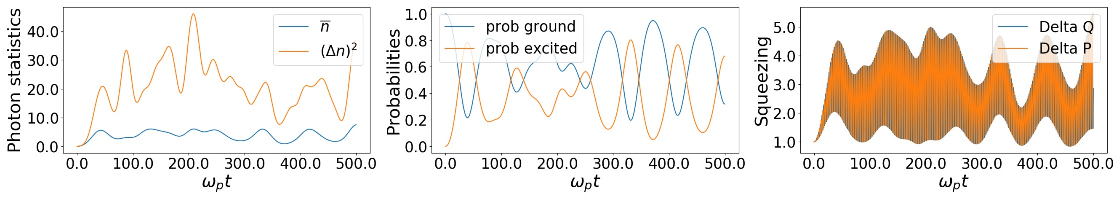

$N = 10$ atoms

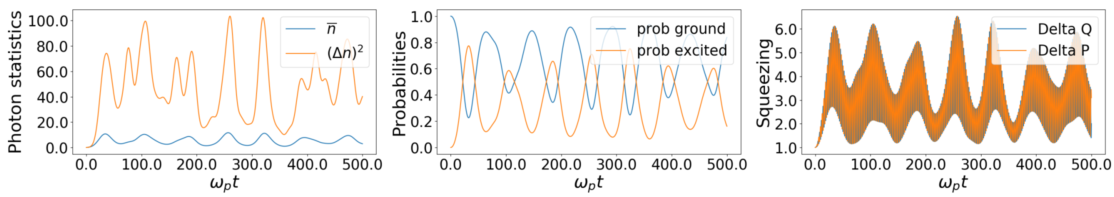

$g_1 = 1.0, \; g_2 = 5.0$

$N = 1$ atom

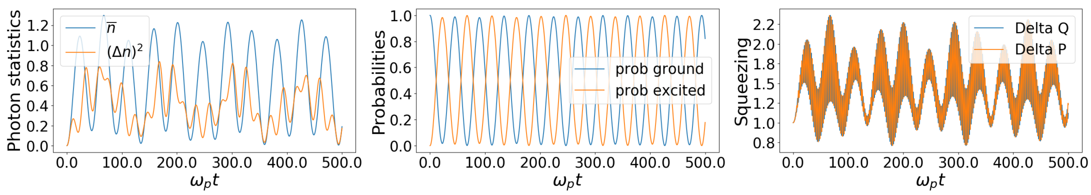

$N = 2$ atoms

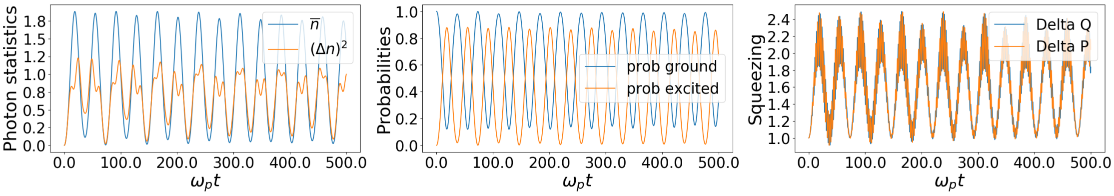

$N = 5$ atoms

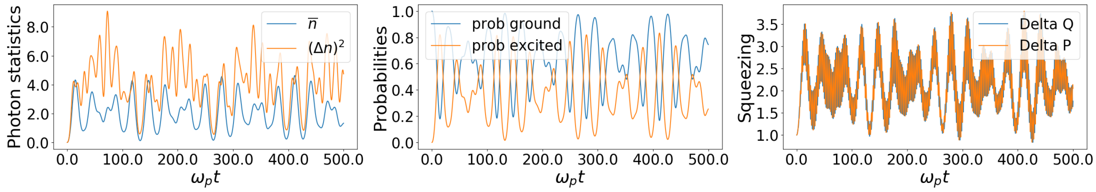

$N = 10$ atoms

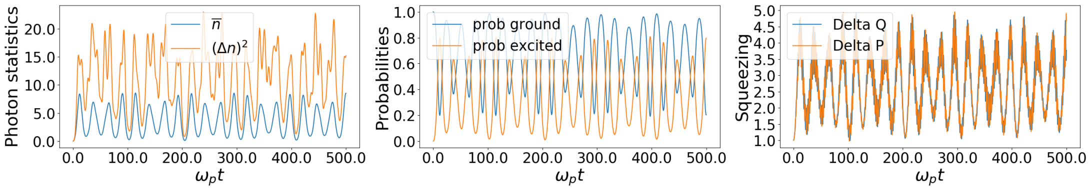

$$g_1 = 1.0,\ g_2 = 10.0$$

$N = 1$ atom

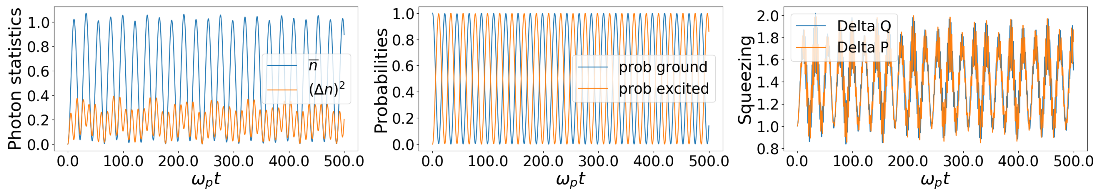

$N = 2$ atoms

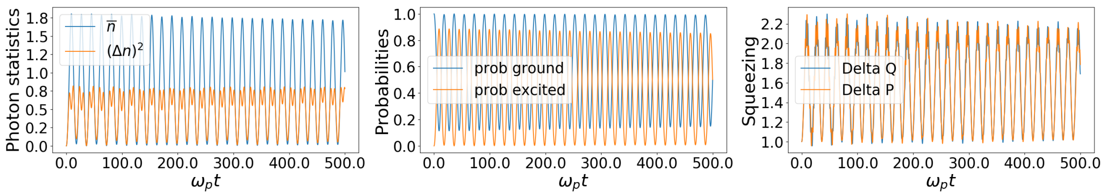

$N = 5$ atoms

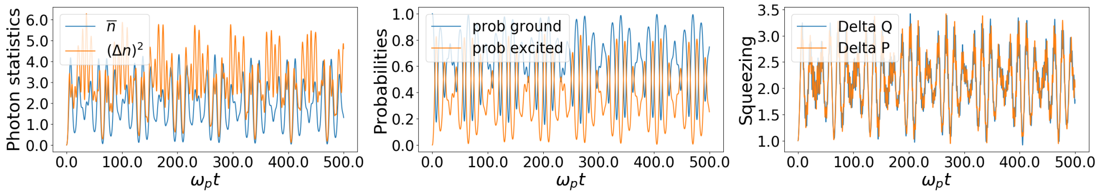

$N = 10$ atoms

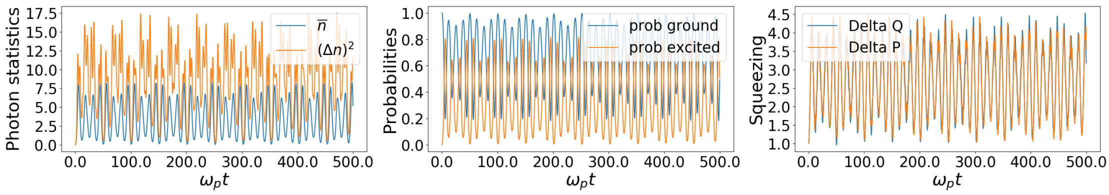

$g_1 = 2.0,\ g_2 = 1.0$

$N = 1$ atom

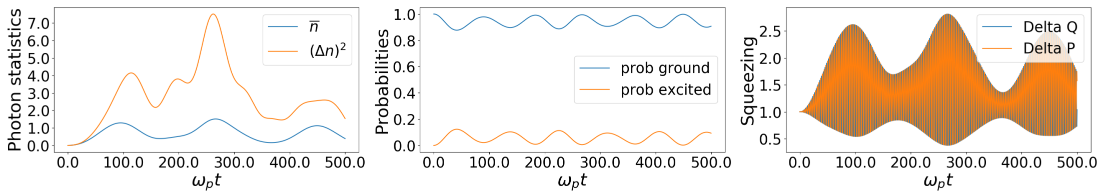

$N = 2$ atoms

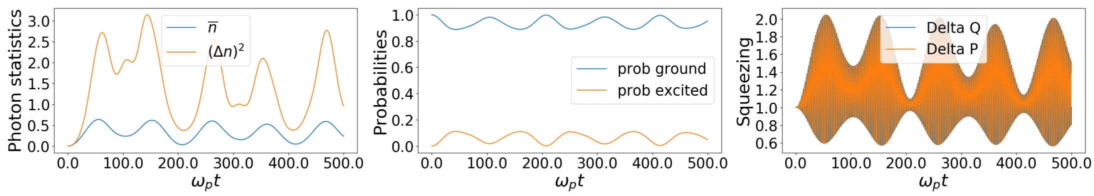

$N = 5$ atoms

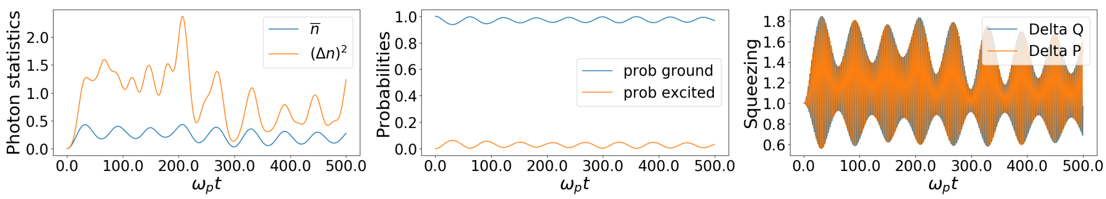

$N = 10$ atoms

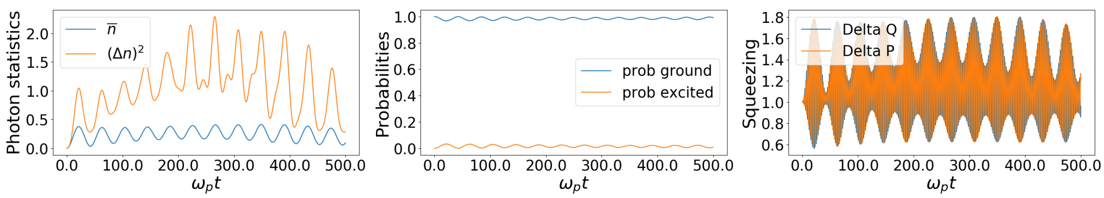

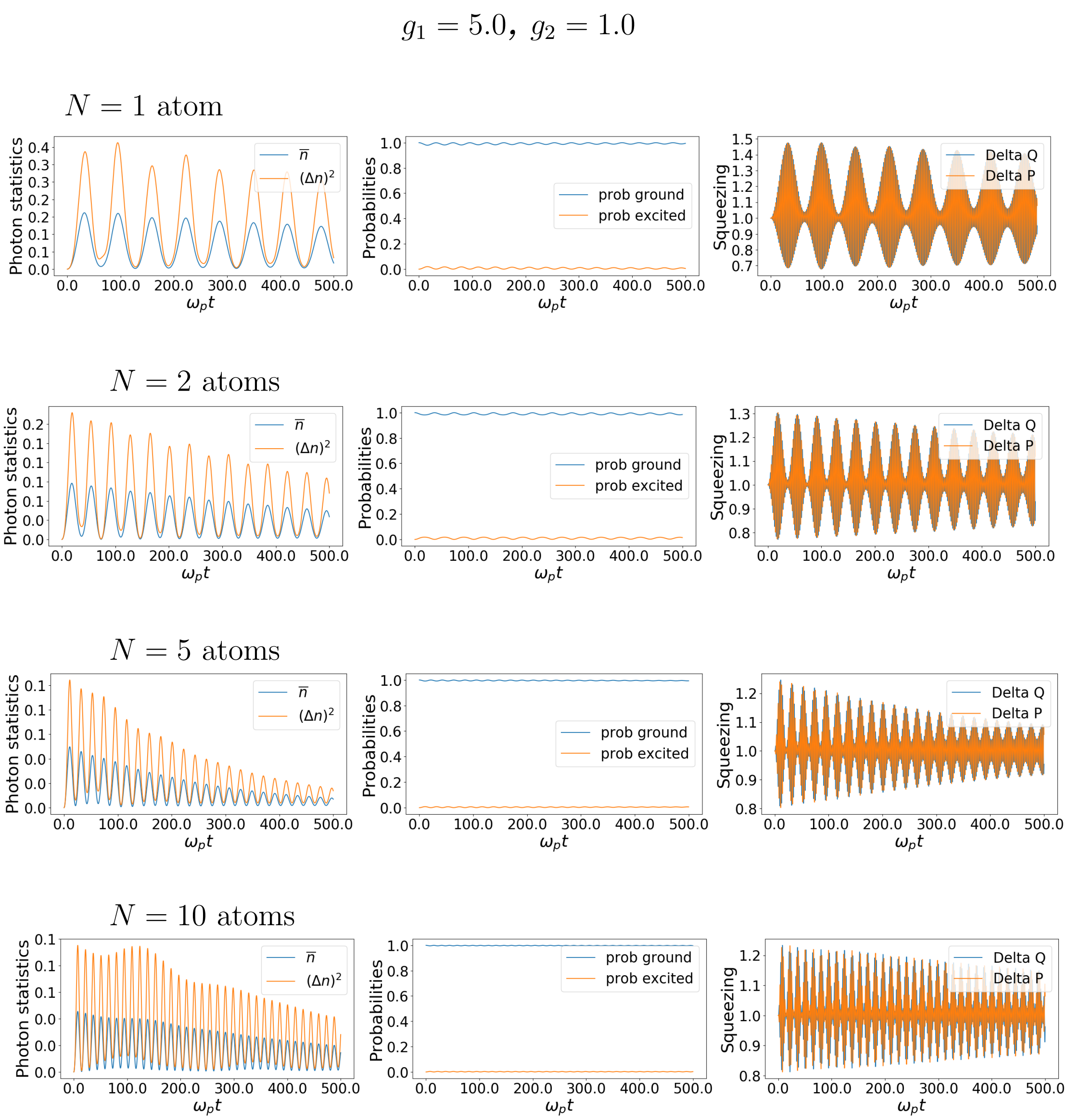

$g_1 = 5.0, \; g_2 = 1.0$
$N = 1$ atom
$N = 2$ atoms
$N = 5$ atoms
$N = 10$ atoms
Photon statistics
$\overline{n}$
$(\Delta n)^2$
Probabilities
prob ground
prob excited
Squeezing
Delta Q
Delta P
$\omega_p t$

$$g_1 = 10.0, \; g_2 = 1.0$$

$N = 1$ atom

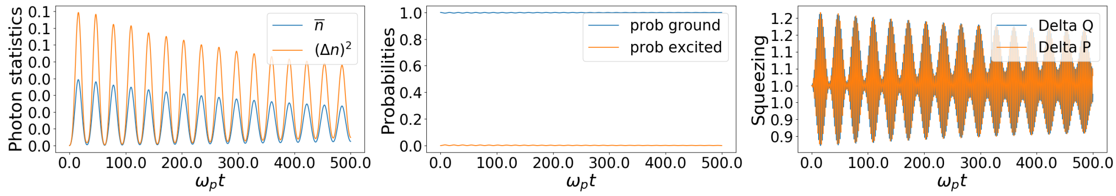

$N = 2$ atoms

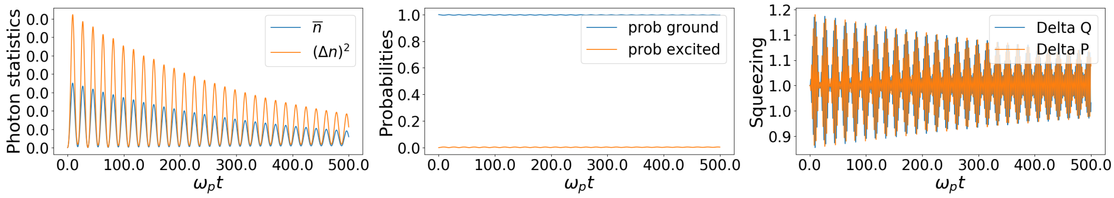

$N = 5$ atoms

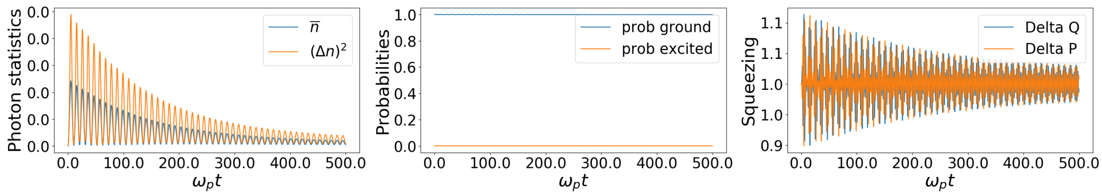

$N = 10$ atoms

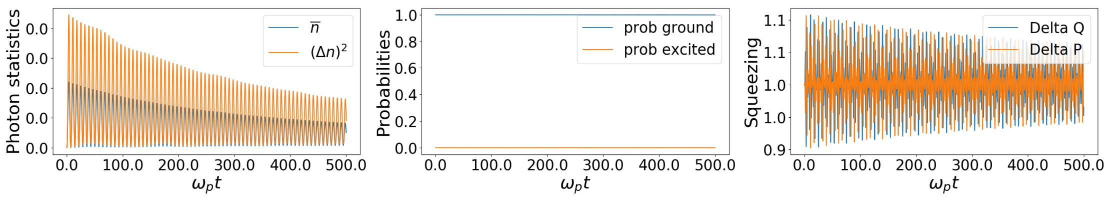

Appendix C

Squeezed light, simulation code

```
import numpy as np

import matplotlib.pyplot as plt

from qutip import *

import matplotlib.ticker as mtick

from mpl_toolkits.mplot3d import Axes3D

import os.path

import sys



wp = 70.0               # probe beam frequency

wc1 = 100.0             # control laser 1 frequency

wc2 = 40.0              # control laser 2 frequency

wa = 30.0               # atom frequency


g1_default  = 0.5       # coupling strength resonance 1

g2_default  = 1.0       # coupling strength resonance 2


kappa = 0.000            # photon dissipation rate

gamma = 0.00             # atoms dissipation rate
```

```
N = 500             # dimension of Fock space
n_th_a = 0.0           # temperature in frequency units



Delta1_default = 0.0
Delta2_default = 0.0

# definition of the time interval to run
t_min = 0.0
t_max = 500.0
time_step = 0.01
tlist = np.arange(t_min, t_max, time_step)




### SINGLE ATOM DEFINITIONS ###

# intial state (wave function) of the system

psi0_number_state = tensor(basis(N,n), basis(2,0))
# start with a photon number state n
psi0_coherent = tensor(coherent(N,alpha), basis(2,0))
# start with a coherent state of parameter alpha
psi0_vacuum = tensor(coherent(N,0), basis(2,0))
# start with a vacuum state

psi0_default = psi0_vacuum

# Operator definitions. From this, expectation values are calculated
```

```
a  = tensor(destroy(N), qeye(2))
sigma_minus = tensor(qeye(N), destroy(2))
sigma_plus = sigma_minus.dag()

n_operator = a.dag()*a
Q_op = a + a.dag()
P_op = 1j*(a.dag() - a)

# Hamiltonian definition


def Hamiltonian(g1, g2, g3, Delta1, Delta2):
#Here Delta1 and Delta2 are the detunings from resonance

    H0 = wp*a.dag()*a + wa*sigma_plus*sigma_minus

    H1 = g1*a.dag()*sigma_minus
    H2 = g2*a*sigma_minus
    H3 = H1.dag()    #H3 = np.conjugate(g1)*sigma_plus*a
    H4 = H2.dag()    #H4 = np.conjugate(g2)*sigma_plus*a.dag()
    H5 = g3 * a**2
    H6 = H5.dag()

    def H1_coeff(t, args):
        return np.exp(-1j*(wc2+Delta2)*t)

    def H2_coeff(t, args):
        return np.exp(1j*(wc1+Delta1)*t)
```

```
    def H3_coeff(t, args):
        return np.exp(1j*(wc2+Delta2)*t)

    def H4_coeff(t, args):
        return np.exp(-1j*(wc1+Delta1)*t)

    def H5_coeff(t, args):
        return np.exp(-1j*wc3*t)

    def H6_coeff(t, args):
        return np.exp(1j*wc3*t)


    H = [H0,[H1,H1_coeff],[H2,H2_coeff],[H3,H3_coeff],
    [H4,H4_coeff],[H5,H5_coeff],[H6,H6_coeff]]

    return H

### MULTIPLE ATOMS DEFINITIONS ###

# intial state (wave function) of the system

psi0_vacuum = qutip.tensor(basis(N,0),
*[qutip.basis(2, 0) for _ in range(atom_num)])
psi0_number_state = qutip.tensor(basis(N,n),
*[qutip.basis(2, 0) for _ in range(atom_num)])
# start with a photon number state
psi0_coherent = qutip.tensor(basis(N,alpha),
```

```
*[qutip.basis(2, 0) for _ in range(atom_num)])
# start with a coherent state


# operators

a = qutip.tensor(destroy(N),*[qeye(2) for _ in range(atom_num)])

sigma_multiplications = 0
sigma_minus_sum = 0
sigma_plus_sum = 0

for i in range(atom_num):
    lst = [qeye(N)] + [qeye(2) for _ in range(i)] + [destroy(2)]
    + [qeye(2) for _ in range(atom_num-i-1)]
    sigma_minus = qutip.tensor(*lst)
    sigma_plus = sigma_minus.dag()

    sigma_multiplications += sigma_plus * sigma_minus
    sigma_minus_sum += sigma_minus
    sigma_plus_sum += sigma_plus

n_operator = a.dag()*a
Q_op = a + a.dag()
P_op = 1j*(a.dag() - a)

# Expectation values to calculate

tmp_lst = [qeye(N)] + [qeye(2) for _ in range(0)] + [destroy(2)]
```

```
+ [qeye(2) for _ in range(atom_num-0-1)]
sigma_minus_one = qutip.tensor(*tmp_lst)
sigma_minus = sigma_minus_one
sigma_plus = sigma_minus.dag()


# Hamiltonian

H0 = wp*a.dag()*a + wa * sigma_multiplications


def Hamiltonian(g1, g2, g3, Delta1, Delta2):

    H1 = g1*a.dag()*sigma_minus_sum
    H2 = g2*a*sigma_minus_sum
    H3 = H1.dag()    #H3 = np.conjugate(g1)*sigma_plus*a
    H4 = H2.dag()    #H4 = np.conjugate(g2)*sigma_plus*a.dag()
    H5 = g3 * a**2
    H6 = H5.dag()

    def H1_coeff(t, args):
        return np.exp(-1j*(wc2+Delta2)*t)

    def H2_coeff(t, args):
        return np.exp(1j*(wc1+Delta1)*t)

    def H3_coeff(t, args):
        return np.exp(1j*(wc2+Delta2)*t)
```

```
    def H4_coeff(t, args):
        return np.exp(-1j*(wc1+Delta1)*t)

    def H5_coeff(t, args):
        return np.exp(-1j*wc3*t)

    def H6_coeff(t, args):
        return np.exp(1j*wc3*t)


    H = [H0,[H1,H1_coeff],[H2,H2_coeff],[H3,H3_coeff],
    [H4,H4_coeff],[H5,H5_coeff],[H6,H6_coeff]]

    return H



# Dissipation operators (if these are nonzero, the simulation
uses a master equation rather than Schrodinger's equation)

c_op_list = []

rate = kappa * (1 + n_th_a)
if rate > 0.0:
    c_op_list.append(np.sqrt(rate) * a)
    #c_op_list.append(np.sqrt(rate) * sigma_minus)

rate = kappa * n_th_a
if rate > 0.0:
```

```
    c_op_list.append(np.sqrt(rate) * a.dag())


rate = gamma
if rate > 0.0:
    c_op_list.append(np.sqrt(rate) * sigma_minus)





def Calculate_dynamics(psi0, H):
#QuTiP calculates the expectation values of the defined operators
by using either Schrodinger's equation or a master equation



    calc_list = [n_operator, n_operator**2, Q_op, \
                 Q_op**2, P_op, P_op**2, sigma_plus*sigma_minus,
                 sigma_minus*sigma_plus]

    output = mesolve(H, psi0, tlist, c_op_list, calc_list)

    n_avg = output.expect[0]
    n_squared_avg = output.expect[1]
    n_variance = n_squared_avg - n_avg**2

    Q_avg = output.expect[2]
    Q_avg_squared = output.expect[3]
    Delta_Q = np.sqrt(Q_avg_squared - Q_avg**2)

    P_avg = output.expect[4]
```

```
    P_avg_squared = output.expect[5]
    Delta_P = np.sqrt(P_avg_squared - P_avg**2)

    prob_excited = output.expect[6]

    prob_ground = output.expect[7]

    return(n_avg, n_variance, Delta_Q, Delta_P,
    prob_excited, prob_ground)




def Calculate_photon_statistics():
#Calculating time-dependent expectation values
of the photons and the atom

    Delta1_set = 0.0
    Delta2_set = 0.0

    H = Hamiltonian(g1_default, g2_default, Delta1_set, Delta2_set)
    n_avg, n_variance, Delta_Q, Delta_P, prob_excited,
    prob_ground = Calculate_dynamics(psi0_vacuum, H)

    save_path = 'Results/'

    results_file_name = "results_g1="+str(g1_default)+
    "g2="+str(g2_default)+".txt"
```

```
    completeName = os.path.join(save_path, results_file_name)

    with open(completeName, 'w'):
        np.savetxt(completeName, np.column_stack((n_avg,
        n_variance, Delta_Q, Delta_P, prob_excited,
        prob_ground)),delimiter=",")

def Plot_photon_statistics():
#Plotting expectation values for photon statistics analysis

    t_min = 0.0
    t_max = 500.0
    time_step = 0.001

    tlist = (1/wp)*np.arange(t_min, t_max, time_step)

    data_file = "all_results.txt"
    data_sorted = np.loadtxt(data_file, delimiter=',')

    n_avg = np.array(data_sorted[:,0])
    n_variance = np.array(data_sorted[:,1])
    Delta_Q = np.array(data_sorted[:,2])
    Delta_P = np.array(data_sorted[:,3])
    prob_excited = np.array(data_sorted[:,4])
    prob_ground = np.array(data_sorted[:,5])

    kappa_val = 0.0
    gamma_val = 0.0
    g1_val = 10.0
```

```
g2_val = 1.0

fig.suptitle("$g_1 = {}, g_2 = {}$ ".format(g1_val, g2_val))

plt.subplot(3,3,1)

plt.xlabel("$\\omega_p t$")
plt.ylabel("Photon statistics")
plt.plot(wp*tlist, n_avg, label='$\overline{n}$')
plt.plot(wp*tlist, n_variance, label='$(\\Delta n)^2$')

ax = plt.gca()
ax.legend()
ax.xaxis.set_major_formatter(mtick.FormatStrFormatter('%.1f'))
ax.yaxis.set_major_formatter(mtick.FormatStrFormatter('%.1f'))

plt.subplot(3,3,2)

plt.xlabel("$\\omega_p t$")
plt.ylabel("Probabilities")
plt.plot(wp*tlist, prob_ground, label='prob ground')
plt.plot(wp*tlist, prob_excited, label = 'prob excited')
ax = plt.gca()
ax.legend()
ax.xaxis.set_major_formatter(mtick.FormatStrFormatter('%.1f'))
ax.yaxis.set_major_formatter(mtick.FormatStrFormatter('%.1f'))

plt.subplot(3,3,3)
```

```
plt.xlabel("$\\omega_p t$")
plt.ylabel("Squeezing")
plt.plot(wp*tlist, Delta_Q, label='$\\Delta Q$')
plt.plot(wp*tlist, Delta_P, label='$\\Delta P$')
ax = plt.gca()
ax.legend()
ax.xaxis.set_major_formatter(mtick.FormatStrFormatter('%.1f'))
ax.yaxis.set_major_formatter(mtick.FormatStrFormatter('%.1f'))

return (tlist, Delta_Q, Delta_P)



def calculate_range(list_of_detunings):
#Plots the minimum value of the quadratures Q and P, for a range
of detunings Delta1 and Delta2 from the two resonances
#list_of_detunings include the range of detunings D1 and D2
from the two resonances

psi0 = psi0_default

H = Hamiltonian(g1_default, g2_default, g3_default, D1, D2)

n_avg, n_variance, Delta_Q, Delta_P, prob_excited =
Calculate_dynamics(psi0, H)

Delta_Q_vac, Delta_P_vac = Quadrature_squeezing_vacuum(H0)

Qlog = 10*np.log10(Delta_Q**2)
Plog = 10*np.log10(Delta_P**2)
```

```
    Qmin= np.min(Qlog)
    Pmin = np.min(Plog)

    save_path = 'Results/'

    results_file_name = "results_"+str(D1)+"_"+str(D2)+".txt"

    completeName = os.path.join(save_path, results_file_name)

    with open(completeName, 'w') as file:
        file.write('{}, {}, {}, {}\n'.format(D1, D2, Qmin, Pmin))


        file.close()



def plot_range_from_data():
# this function makes a contour plot of the data calculated with
the function plot_range_calculate.

    data_set = load_data()
    data_sorted = np.array(sorted(map(tuple,data_set)))

    Delta1_array = np.array(data_sorted[:,0])
    Delta2_array = np.array(data_sorted[:,1])
    Qmins = np.array(data_sorted[:,2])
    Pmins = np.array(data_sorted[:,3])
```

```
Mandel_Q = np.array(data_sorted[:,4])


Detuning_interval = np.arange(min_D,max_D,spacing)
#the interval along which D1 and D2 were calculated


D1, D2 = np.meshgrid(Detuning_interval, Detuning_interval)
#D1 and D2 as 2D object containing the detunings, for the
contour plot


counter = 0


Qmin_array = np.zeros( (Detuning_interval.size,
Detuning_interval.size) )
Pmin_array = np.zeros( (Detuning_interval.size,
Detuning_interval.size) )
Mandel_Q_array = np.zeros( (Detuning_interval.size,
Detuning_interval.size) )


for i in range(Detuning_interval.size):
    for j in range(Detuning_interval.size):


        Qmin_array[j,i] = Qmins[counter]
        Pmin_array[j,i] = Pmins[counter]
        Mandel_Q_array[j,i] = Mandel_Q[counter]


        counter+=1


figQ = plt.figure('Q and P contour plots')
```

```
ax = plt.gca()
ax.xaxis.set_major_formatter(mtick.FormatStrFormatter('%.1f'))
ax.yaxis.set_major_formatter(mtick.FormatStrFormatter('%.1f'))



plt.subplot(2,3,1)
cq = plt.contourf(D1, D2, Qmin_array, 500)
cbar1 = plt.colorbar(cq)
plt.title('min of $(\Delta Q)^2$ in dB')
plt.xlabel('$\Delta_1$')
plt.ylabel('$\Delta_2$')
plt.show()

plt.subplot(2,3,2)
cp = plt.contourf(D1, D2, Pmin_array, 500)
cbar2 = plt.colorbar(cp)
plt.title('min of $(\Delta P)^2$ in dB')
plt.xlabel('$\Delta_1$')
plt.ylabel('$\Delta_2$')
plt.show()

plt.subplot(2,3,3)
cp = plt.contourf(D1, D2, Mandel_Q_array, 500)
cbar3 = plt.colorbar(cp)
cbar3.ax.yaxis.set_major_formatter(mtick.FormatStrFormatter('%.1f'))
plt.title('Contour min ($\Delta n^2 - \overline{n}$) Plot')
plt.xlabel('$\Delta_1$')
plt.ylabel('$\Delta_2$')
plt.show()
```

```
return (D1, D2, Qmin_array, Pmin_array, Mandel_Q_array)

return data_sorted

return (Delta1_array, Delta2_array)

return Mandel_Q
```

Appendix D

Field equations from EM and axion Lagrangian

It is natural and convenient to derive the electromagnetic and axion field equations using a relativistcally covariant formalism. The covariant Lagrangian describing the axion and electromagnetic fields is

$$\mathcal{L} = \frac{1}{2}\partial_\mu\phi\partial^\mu\phi - \frac{1}{2}\left(\frac{mc}{\hbar}\right)^2\phi^2 - \frac{1}{4\mu_0}F_{\mu\nu}F^{\mu\nu} - A_\mu j^\mu - \frac{g_{a\gamma\gamma}}{8\mu_0}\phi\,\varepsilon^{\mu\nu\alpha\beta}F_{\mu\nu}F_{\alpha\beta} \tag{D.1}$$

where ϕ describes the axion field and $F^{\mu\nu}$ is the electromagnetic tensor, given by $F^{\mu\nu} = \partial^\mu A^\nu - \partial^\nu A^\mu$ where $A^\mu = (\frac{1}{c}\phi_e, \vec{A})$ is the four-potential and ϕ_e and $\vec{A}$ are the electric potential and the magnetic vector potential. $j^\mu = (c\rho, \vec{J})$ is the 4-current. The electromagnetic tensor can also be expressed using the electric and magnetic fields as we discuss below. The first 4 terms in the Lagrangian are the free-field terms. The first two terms describe the axion scalar field while the third and fourth terms describe the electromagnetic (EM) field. The last term describes the interaction between the EM field and the axion. Using the Euler-Lagrange (EL) equations, we can derive the axion field equation and modified Maxwell's equations describing these fields.

It is useful to express the electromagnetic tensor using the electric and magnetic fields. In 3D terms, the electric and magnetic fields $\vec{E}$ and $\vec{B}$ are both vector quantities, each having 3 components and all together they have 6 components. Relativistically, these 6 components form an anti-symmetric tensor $F^{\mu\nu} = -F^{\nu\mu}$. This tensor can be written in a matrix form as:

$$F^{\mu\nu} = \begin{pmatrix} 0 & -E_x/c & -E_y/c & -E_Z/c \\ E_x/c & 0 & -B_z & B_y \\ E_y/c & B_z & 0 & -B_x \\ E_z/c & -B_y & B_x & 0 \end{pmatrix} \tag{D.2}$$

or using the components $F^{00} = 0$, $F^{0i} = -E^i/c$, $F^{i0} = E^i/c$, $F^{ij} = -\varepsilon^{ijk}B^k$. From this, we can get $F_{\mu\nu}$. In all of the following we use repeated indices to mean summation over that index (contraction of the tensors over that index). Using the flat-space metric $g^{\mu\nu} = g_{\mu\nu} = \mathrm{diag}(1, -1, -1, -1)$ to raise and lower indices:

$$F_{\mu\nu} = g_{\mu\alpha}F^{\alpha\beta}g_{\beta\nu} = \begin{pmatrix} 0 & E_x/c & E_y/c & E_z/c \\ -E_x/c & 0 & -B_z & B_y \\ -E_y/c & B_z & 0 & -B_x \\ -E_z/c & -B_y & B_x & 0 \end{pmatrix} \tag{D.3}$$

Finally, we define the dual tensor

$$G^{\mu\nu} = \frac{1}{2}\varepsilon^{\mu\nu\rho\sigma}F_{\rho\sigma} = \begin{pmatrix} 0 & -B_x & -B_y & -B_z \\ B_x & 0 & E_z/c & -E_y/c \\ B_y & -E_z/c & 0 & E_z/c \\ B_z & E_y/c & -E_x/c & 0 \end{pmatrix} \tag{D.4}$$

and from these tensors we get the useful relation $G^{\mu\nu}F_{\mu\nu} = -4\vec{E}\cdot\vec{B}/c$. Let us now derive the axion field equation. The EL equation for the axion field:

$$\frac{\partial\mathcal{L}}{\partial\phi} = \partial_\sigma\frac{\partial\mathcal{L}}{\partial(\partial_\sigma\phi)} \tag{D.5}$$

and using the fact that

$$\frac{\partial(\partial_\mu\phi)}{\partial(\partial_\nu\phi)} = \delta^\nu_\mu \tag{D.6}$$

we have

$$\begin{aligned}
\partial_\sigma \frac{\partial \mathcal{L}}{\partial(\partial_\sigma\phi)} &= \partial_\sigma \frac{\partial}{\partial(\partial_\sigma\phi)}\left[\frac{1}{2}g^{\mu\nu}\partial_\mu\phi\partial_\nu\phi\right] \\
&= \frac{1}{2}\partial_\sigma\left[g^{\mu\nu}\frac{\partial(\partial_\mu\phi)}{\partial(\partial_\sigma\phi})\partial_\nu\phi + g^{\mu\nu}\partial_\mu\phi\frac{\partial(\partial_\nu\phi)}{\partial(\partial_\sigma\phi)}\right] \\
&= \frac{1}{2}\partial_\sigma(g^{\mu\nu}\delta^\sigma_\mu\partial_\nu\phi + g^{\mu\nu}\partial_\mu\phi\delta^\sigma_\nu) \\
&= \frac{1}{2}\partial_\sigma(g^{\sigma\nu}\partial_\nu\phi + g^{\mu\sigma}\partial_\mu\phi) \\
&= \frac{1}{2}\partial_\sigma(\partial^\sigma\phi + \partial^\sigma\phi) \\
&= \partial_\sigma\partial^\sigma\phi
\end{aligned} \tag{D.7}$$

and

$$\begin{aligned}
\frac{\partial\mathcal{L}}{\partial\phi} &= -\left(\frac{mc}{\hbar}\right)^2\phi - \frac{g_{a\gamma\gamma}}{8\mu_0}\varepsilon^{\mu\nu\alpha\beta}F_{\mu\nu}F_{\alpha\beta} \\
&= -\left(\frac{mc}{\hbar}\right)^2\phi + \frac{g_{a\gamma\gamma}}{8\mu_0}\cdot\frac{8\vec{E}\cdot\vec{B}}{c} \\
&= -\left(\frac{mc}{\hbar}\right)^2\phi + \frac{g_{a\gamma\gamma}}{\mu_0 c}\,\vec{E}\cdot\vec{B}
\end{aligned} \tag{D.8}$$

therefore

$$\begin{aligned}
\partial_\sigma\partial^\sigma\phi &= -\left(\frac{mc}{\hbar}\right)^2\phi + \frac{g_{a\gamma\gamma}}{\mu_0 c}\,\vec{E}\cdot\vec{B} \\
\therefore \partial_0\partial^0\phi + \partial_j\partial^j\phi &= -\left(\frac{mc}{\hbar}\right)^2\phi + \frac{g_{a\gamma\gamma}}{\mu_0 c}\,\vec{E}\cdot\vec{B}
\end{aligned} \tag{D.9}$$

now, considering that $\partial_\mu = (\frac{1}{c}\frac{\partial}{\partial t}, \nabla)$ while $\partial^\mu = g^{\mu\nu}\partial_\nu = (\frac{1}{c}\frac{\partial}{\partial t}, -\nabla)$, we get:

$$
\begin{aligned}
&\frac{1}{c^2}\frac{\partial^2\phi}{\partial t^2} - \nabla^2\phi = -\left(\frac{mc}{\hbar}\right)^2\phi + \frac{g_{a\gamma\gamma}}{\mu_0 c}\vec{E}\cdot\vec{B} \\
\therefore &\boxed{\nabla^2\phi - \frac{1}{c^2}\frac{\partial^2\phi}{\partial t^2} - \left(\frac{mc}{\hbar}\right)^2\phi = -\frac{g_{a\gamma\gamma}}{\mu_0 c}\vec{E}\cdot\vec{B}}
\end{aligned}
\tag{D.10}
$$

Now, let's consider the electromagnetic field equations. The two homogeneous Maxwell's equations follow from the identity:

$\partial^\lambda F^{\mu\nu} + \partial^\mu F^{\nu\lambda} + \partial^\nu F^{\lambda\mu} = 0$

which can be written using the 4D Levi-Civita tensor:

$$\varepsilon_{\alpha\lambda\mu\nu}\partial^\lambda F^{\mu\nu} = 0 \tag{D.11}$$

the proof of it relies on the properties of the electromagnetic tensor. Since this doesn't depend on other fields / sources, it should be clear at this point that the homogeneous Maxwell's equations will remain unchanged with the addition of the axion field. We can prove this identity by writing $F^{\mu\nu} = \partial^\mu A^\nu - \partial^\nu A^\mu$. Then

$$
\begin{aligned}
&\varepsilon_{\alpha\lambda\mu\nu}\partial^\lambda(\partial^\mu A^\nu - \partial^\nu A^\mu) = 0 \\
\therefore\ &\varepsilon_{\alpha\lambda\mu\nu}\partial^\lambda\partial^\mu A^\nu - \varepsilon_{\alpha\lambda\mu\nu}\partial^\lambda\partial^\nu A^\mu = 0
\end{aligned}
\tag{D.12}
$$

since $\varepsilon_{\alpha\lambda\mu\nu}$ is a totally antisymmetric tensor, it is antisymmetric in the change of indices $\lambda \leftrightarrow \mu$ while $\partial^\lambda\partial^\mu$ is symmetric in these indices, so their contraction is equal to zero and the first term vanishes. The second term vanishes for the same reason, with the change of indices $\lambda \leftrightarrow \nu$. This proves the identity (D.11). In the following we will use the relation

$$\varepsilon^{jki}\varepsilon^{jk\ell} = \delta^{kk}\delta^{i\ell} - \delta^{k\ell}\delta^{ik} = 3\delta^{i\ell} - \delta^{i\ell} = 2\delta^{i\ell} \tag{D.13}$$

To get the first homogeneous Maxwell's equation, take $\alpha = 0$.

$$\begin{aligned}\varepsilon_{0\lambda\mu\nu}\partial^\lambda F^{\mu\nu} &= \varepsilon^{ijk}\partial^i F^{jk} = -\varepsilon^{ijk}\partial^i \varepsilon^{jk\ell} B^\ell \\ &= -2\delta^{i\ell}\partial^i B^\ell = -2\partial^\ell B^\ell = -2\nabla \cdot \vec{B} = 0\end{aligned} \tag{D.14}$$

therefore,

$$\boxed{\nabla \cdot \vec{B} = 0} \tag{D.15}$$

To get the other homogeneous Maxwell equation, set $\alpha = i = 1, 2, 3$:

$$\begin{aligned}\varepsilon_{i\lambda\mu\nu}\partial^\lambda F^{\mu\nu} &= \varepsilon_{i0jk}\partial^0 F^{jk} + \varepsilon_{ij0k}\partial^j F^{0k} + \varepsilon_{ijk0}\partial^j F^{k0} \\ &= (-\varepsilon^{ijk})\partial^0(-\varepsilon^{jk\ell}B^\ell) + \varepsilon^{ijk}\partial^j\left(-\frac{E^k}{c}\right) - \varepsilon^{ijk}\partial^j\left(\frac{E^k}{c}\right) \\ &= 2\delta^{i\ell}\partial^0 B^\ell - \frac{1}{c}\varepsilon^{ijk}\partial^j E^k - \frac{1}{c}\varepsilon^{ijk}\partial^j E^k \\ &= 2\left(\frac{1}{c}\frac{\partial}{\partial t}\right)B^i - \frac{2}{c}\varepsilon^{ijk}(-\nabla^j)E^k \\ &= \frac{2}{c}\left(\frac{\partial B^i}{\partial t} + \varepsilon^{ijk}\nabla^j E^k\right) = 0\end{aligned} \tag{D.16}$$

therefore,

$$\begin{aligned}&\frac{\partial \vec{B}}{\partial t} + \nabla \times \vec{E} = 0 \\ &\therefore \boxed{\nabla \times \vec{E} = -\frac{\partial \vec{B}}{\partial t}}\end{aligned} \tag{D.17}$$

we will make use of these homogeneous Maxwell's equations in deriving the new non-homogeneous Maxwell's equations. To derive the new non-homogeneous Maxwell's equations, consider the EL equation for the electromagnetic fields:

$$\frac{\partial \mathcal{L}}{\partial A_\lambda} = \partial_\sigma \frac{\partial \mathcal{L}}{\partial(\partial_\sigma A_\lambda)} \tag{D.18}$$

we will use the fact that

$$\frac{\partial(\partial_\mu A_\nu)}{\partial(\partial_\sigma A_\lambda)} = \delta^\sigma_\mu \delta^\lambda_\nu \tag{D.19}$$

it is useful to first calculate

$$\frac{\partial F_{\mu\nu}}{\partial(\partial_\sigma A_\lambda)} = \frac{\partial(\partial_\mu A_\nu - \partial_\nu A_\mu)}{\partial(\partial_\sigma A_\lambda)} = \delta^\sigma_\mu \delta^\lambda_\nu - \delta^\sigma_\nu \delta^\lambda_\mu \tag{D.20}$$

therefore:

$$\begin{aligned}
\frac{\partial \mathcal{L}}{\partial(\partial_\sigma A_\lambda)} &= \frac{\partial(-\frac{1}{4\mu_0} F_{\mu\nu}F^{\mu\nu} - \frac{g_{a\gamma\gamma}}{8\mu_0}\phi\,\varepsilon^{\mu\nu\alpha\beta}F_{\mu\nu}F_{\alpha\beta})}{\partial(\partial_\sigma A_\lambda)} \\
&= -\frac{1}{4\mu_0}\frac{\partial F_{\mu\nu}}{\partial(\partial_\sigma A_\lambda)}F^{\mu\nu} - \frac{1}{4\mu_0}F_{\mu\nu}g^{\mu\alpha}g^{\nu\beta}\frac{\partial F_{\alpha\beta}}{\partial(\partial_\sigma A_\lambda)} \\
&- \frac{g_{a\gamma\gamma}}{8\mu_0}\phi\,\varepsilon^{\mu\nu\alpha\beta}\frac{\partial F_{\mu\nu}}{\partial(\partial_\sigma A_\lambda)}F_{\alpha\beta} - \frac{g_{a\gamma\gamma}}{8\mu_0}\phi\,\varepsilon^{\mu\nu\alpha\beta}F_{\mu\nu}\frac{\partial F_{\alpha\beta}}{\partial(\partial_\sigma A_\lambda)} \\
&= -\frac{1}{4\mu_0}(\delta^\sigma_\mu\delta^\lambda_\nu - \delta^\sigma_\nu\delta^\lambda_\mu)F^{\mu\nu} - \frac{1}{4\mu_0}F_{\mu\nu}g^{\mu\alpha}g^{\nu\beta}(\delta^\sigma_\alpha\delta^\lambda_\beta - \delta^\sigma_\beta\delta^\lambda_\alpha) \\
&- \frac{g_{a\gamma\gamma}}{8\mu_0}\phi\,\varepsilon^{\mu\nu\alpha\beta}(\delta^\sigma_\mu\delta^\lambda_\nu - \delta^\sigma_\nu\delta^\lambda_\mu)F_{\alpha\beta} - \frac{g_{a\gamma\gamma}}{8\mu_0}\phi\,\varepsilon^{\mu\nu\alpha\beta}F_{\mu\nu}(\delta^\sigma_\alpha\delta^\lambda_\beta - \delta^\sigma_\beta\delta^\lambda_\alpha) \\
&= -\frac{1}{4\mu_0}(F^{\sigma\lambda} - F^{\lambda\sigma}) - \frac{1}{4\mu_0}(F^{\sigma\lambda} - F^{\lambda\sigma}) \\
&- \frac{g_{a\gamma\gamma}}{8\mu_0}\phi\,\varepsilon^{\sigma\lambda\alpha\beta}F_{\alpha\beta} + \frac{g_{a\gamma\gamma}}{8\mu_0}\phi\,\varepsilon^{\lambda\sigma\alpha\beta}F_{\alpha\beta} - \frac{g_{a\gamma\gamma}}{8\mu_0}\phi\,\varepsilon^{\mu\nu\sigma\lambda}F_{\mu\nu} + \frac{g_{a\gamma\gamma}}{8\mu_0}\phi\,\varepsilon^{\mu\nu\lambda\sigma}F_{\mu\nu} \\
&= -\frac{1}{\mu_0}F^{\sigma\lambda} - \frac{g_{a\gamma\gamma}}{2\mu_0}\phi\,\varepsilon^{\sigma\lambda\mu\nu}F_{\mu\nu}
\end{aligned} \tag{D.21}$$

where in the last equality we used the antisymmetry properties of $F^{\mu\nu}$ and $\varepsilon^{\mu\nu\rho\sigma}$ tensors for changing the order of their indices. Therefore

$$\partial_\sigma \frac{\partial \mathcal{L}}{\partial(\partial_\sigma A_\lambda)} = -\frac{1}{\mu_0}\partial_\sigma F^{\sigma\lambda} - \frac{g_{a\gamma\gamma}}{2\mu_0}(\partial_\sigma\phi)\varepsilon^{\sigma\lambda\mu\nu}F_{\mu\nu} - \frac{g_{a\gamma\gamma}}{2\mu_0}\phi\,\varepsilon^{\sigma\lambda\mu\nu}\partial_\sigma F_{\mu\nu} \tag{D.22}$$

on the other hand

$$\frac{\partial \mathcal{L}}{\partial A_\lambda} = \frac{\partial}{\partial A_\lambda}(-A_\mu j^\mu) = -\frac{\partial A_\mu}{\partial A_\lambda}j^\mu = -\delta^\lambda_\mu j^\mu = -j^\lambda \tag{D.23}$$

Therefore from the Euler-Lagrange equation (D.18):

$$\begin{aligned}\partial_\sigma F^{\sigma\lambda} + \frac{g_{a\gamma\gamma}}{2}(\partial_\sigma\phi)\varepsilon^{\sigma\lambda\mu\nu}F_{\mu\nu} + \frac{g_{a\gamma\gamma}}{2}\phi\,\varepsilon^{\sigma\lambda\mu\nu}\partial_\sigma F_{\mu\nu} &= \mu_0\, j^\lambda \\ \therefore \partial_\sigma F^{\sigma\lambda} + g_{a\gamma\gamma}(\partial_\sigma\phi)G^{\sigma\lambda} + g_{a\gamma\gamma}\phi\,\partial_\sigma G^{\sigma\lambda} &= \mu_0\, j^\lambda\end{aligned} \tag{D.24}$$

where $G^{\mu\nu} = \frac{1}{2}\varepsilon^{\mu\nu\rho\sigma}F_{\rho\sigma}$ is the dual tensor of $F^{\mu\nu}$. Let us see what this equation gives. For $\lambda = 0$:

$$\begin{aligned}\partial_j F^{j0} + g_{a\gamma\gamma}(\partial_j\phi)G^{j0} + g_{a\gamma\gamma}\phi\partial_j G^{j0} &= 0 \\ \partial_j\frac{E_j}{c} + g_{a\gamma\gamma}(\partial_j\phi)B_j + g_{a\gamma\gamma}\phi\partial_j B_j &= 0 \\ \frac{1}{c}\nabla\cdot\vec{E} + g_{a\gamma\gamma}(\nabla\phi)\cdot\vec{B} + g_{a\gamma\gamma}\phi\nabla\cdot\vec{B} &= 0\end{aligned} \tag{D.25}$$

we discarded vanishing terms and also assumed $\rho = 0$ as in our experimental setup so that $j^0 = c\rho = 0$. In the second line we used $F^{j0} = E_j/c$ and $G^{j0} = B_j$. Now since $\nabla\cdot\vec{B} = 0$:

$$\boxed{\nabla\cdot\vec{E} = -g_{a\gamma\gamma}c\,\nabla\phi\cdot\vec{B}} \tag{D.26}$$

Now taking $\lambda = k$ where $k = 1, 2, 3$ are the spatial coordinates:

$$\begin{aligned}&\partial_0 F^{0k} + \partial_j F^{jk} + g_{a\gamma\gamma}(\partial_0\phi)G^{0k} + g_{a\gamma\gamma}(\partial_j\phi)G^{jk} + g_{a\gamma\gamma}\phi\partial_0 G^{0k} \\ &+ g_{a\gamma\gamma}\phi\partial_j G^{jk} = \mu_0 j^k \\ \therefore &-\partial_0\frac{E_k}{c} - \partial_j\varepsilon_{jk\ell}B_\ell - g_{a\gamma\gamma}(\partial_0\phi)B_k + g_{a\gamma\gamma}(\partial_j\phi)\frac{\varepsilon_{jk\ell}E_\ell}{c} - g_{a\gamma\gamma}\phi\,\partial_0 B_k \\ &+ g_{a\gamma\gamma}\phi\partial_j\varepsilon_{jk\ell}\frac{E_\ell}{c} = \mu_0 J_k \\ \therefore &-\frac{1}{c}\partial_0 E_k + \varepsilon_{kj\ell}\partial_j B_\ell - g_{a\gamma\gamma}(\partial_0\phi)B_k - \frac{g_{a\gamma\gamma}}{c}\varepsilon_{kj\ell}(\partial_j\phi)E_\ell - g_{a\gamma\gamma}\phi\partial_0 B_k \\ &- \frac{g_{a\gamma\gamma}}{c}\phi\,\varepsilon_{kj\ell}\partial_j E_\ell = \mu_0 J_k\end{aligned} \tag{D.27}$$

therefore:

$$-\frac{1}{c^2}\frac{\partial \vec{E}}{\partial t} + \nabla \times \vec{B} - \frac{g_{a\gamma\gamma}}{c}\frac{\partial \phi}{\partial t}\vec{B} - \frac{g_{a\gamma\gamma}}{c}\nabla\phi \times \vec{E} - \frac{g_{a\gamma\gamma}}{c}\,\phi\frac{\partial \vec{B}}{\partial t} - \frac{g_{a\gamma\gamma}}{c}\phi\,\nabla \times \vec{E} = \mu_0 \vec{J} \tag{D.28}$$

now using Maxwell's equation $\nabla \times \vec{E} = -\partial \vec{B}/\partial t$ the last two terms on the LHS cancel out, and we get

$$\boxed{\nabla \times \vec{B} = \frac{1}{c^2}\frac{\partial \vec{E}}{\partial t} + \mu_0 \vec{J} + \frac{g_{a\gamma\gamma}}{c}\left(\frac{\partial \phi}{\partial t}\vec{B} + \nabla\phi \times \vec{E}\right)} \tag{D.29}$$

Appendix E

The effect of FWM phase on the experimental sensitivity

For the simplicity of the analysis, we solved Eq. (7.29) assuming the phase-matching case $\Delta k_{\text{FWM}} = 0$. Then, the sensitivity of the scheme relied solely on the sensitivity of the intensity change measurement. Now we consider the effect of the phase mismatch $\Delta k_{\text{FWM}} L \neq 0$ and solve Eq. (7.29) in the general case. To reduce clutter, we will denote Δk_{FWM} by Δk. Integration gives

$$\frac{1}{i\xi E_P}\int_{E_0(0)}^{E_0(L)} dE_0 = \int_0^L e^{i\Delta k} dz \tag{E.1}$$

integrating this,

$$\begin{aligned}
\frac{E_0(L)-E_0(0)}{i\xi E_P} &= \left.\frac{e^{i\Delta k\, z}}{i\Delta k}\right|_0^L \\
&= \frac{e^{i\Delta k\, L}-1}{i\Delta k} \\
&= \frac{\exp(i\Delta k\, L/2)(e^{i\Delta k\, L/2}-e^{-i\Delta k\, L/2})}{i\Delta k} \\
&= \frac{\exp(i\Delta k\, L/2)}{i\Delta k}\cdot 2i\,\sin(\Delta k\, L/2) \\
&= \frac{\sin(\Delta k\, L/2)}{\Delta k\, L/2}\,\exp(i\Delta k\, L/2)L
\end{aligned} \tag{E.2}$$

therefore,

$$E_0(L) = E_0(0)\left(1 + \frac{i\xi E_P L}{E_0(0)}\,\frac{\sin(\Delta k\, L/2)}{\Delta k\, L/2}\,\exp(i\Delta k\, L/2)\right) \tag{E.3}$$

Denote $\frac{\sin(\Delta k\, L/2)}{\Delta k\, L/2} \equiv \mathrm{sinc}(\Delta k\, L/2)$. The intensity ratio is

$$\begin{aligned}
\frac{I(L)}{I(0)} &= \left|\frac{E_0(L)}{E_0(0)}\right|^2 \\
&= \left|1 + \frac{i\xi(\Re(E_P) + i\Im(E_P))L}{E_0(0)}\,\mathrm{sinc}(\Delta k\, L/2)\right|^2 \\
&= \left[\left(1 - \frac{\xi L \Im(E_P)}{E_0(0)}\mathrm{sinc}(\Delta k\, L/2)\right)^2 + \left(\frac{\xi L \Re(E_P)}{E_0(0)}\mathrm{sinc}(\Delta k\, L/2)\right)^2\right]
\end{aligned} \tag{E.4}$$

and dropping terms of order ξ^2:

$$\frac{I(L)}{I(0)} \approx 1 - \frac{2\xi L \Im(E_P)}{E_0(0)}\,\mathrm{sinc}(\Delta k\, L/2) \tag{E.5}$$

Then

$$\frac{\Delta I}{I} = \frac{|I(L) - I(0)|}{I(0)} = \frac{2\xi L \Im(E_P)}{E_0(0)}\,\mathrm{sinc}(\Delta k\, L/2) \tag{E.6}$$

and relative to the "old" sensitivity in Eq. (7.44), following the same steps, we get

$$g^2_{a\gamma\gamma} = g^2_{a\gamma\gamma}(\mathrm{old}) \times \frac{1}{\mathrm{sinc}(\Delta k\, L/2)} \tag{E.7}$$

then using the fact that $\mathrm{sinc}^{-1/2}(x) = 1 + x^2/12 + \mathcal{O}(x^4)$:

$$g_{a\gamma\gamma} = g_{a\gamma\gamma}(\mathrm{old}) + \frac{1}{12}\left(\frac{\Delta k\, L}{2}\right)^2 g_{a\gamma\gamma}(\mathrm{old}) + \mathcal{O}(\Delta k\, L)^4 \tag{E.8}$$

we see that the correction to $g_{a\gamma\gamma}$ measurement sensitivity due to the phase mismatch is of order $(\Delta k\, L/2)^2/12$. To experimentally detect the change in phase (in addition to a possible change in intensity), we use a homodyne detector instead of a balanced detector, as shown in Figure E.1

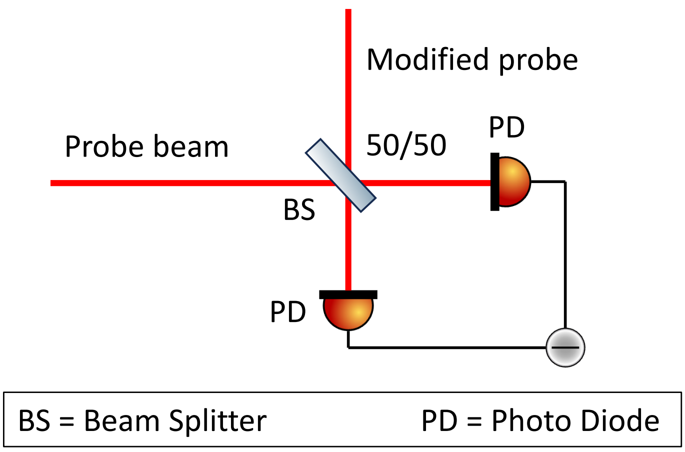

Figure E.1: To measure the changes in both intensity and phase of the probe laser, we use a homodyne detector. The probe beam acts as the local oscillator, while the "modified probe" is the part affected by the interaction with the axions.

Bibliography

[1] J. T. Karpel, D. C. Gold, and D. D. Yavuz, "Prospects for continuous-wave molecular modulation in raman-active microresonators", *Opt. Express* **27**, 34154–34168 (2019).

[2] N. Proite, B. Unks, J. Green, et al., "Refractive index enhancement with vanishing absorption in an atomic vapor", *Phys. Rev. Lett.* **101**, 147401 (2008).

[3] Z. Simmons, N. Proite, J. Miles, et al., "Refractive index enhancement with vanishing absorption in short, high-density vapor cells", *Physical Review A* **85**, 053810 (2012).

[4] C. Gerry, P. Knight, and P. L. Knight, *Introductory quantum optics* (Cambridge university press, 2005).

[5] U. L. Andersen, T. Gehring, C. Marquardt, et al., "30 years of squeezed light generation", *Phys. Scr.* **91**, 053001 (2016).

[6] L.-A. Wu, H. Kimble, J. Hall, et al., "Generation of squeezed states by parametric down conversion", *Phys. Rev. Lett.* **57**, 2520 (1986).

[7] H. Vahlbruch, M. Mehmet, K. Danzmann, et al., "Detection of 15 db squeezed states of light and their application for the absolute calibration of photoelectric quantum efficiency", *Phys. Rev. Lett.* **117**, 110801 (2016).

[8] R. Slusher, L. Hollberg, B. Yurke, et al., "Observation of squeezed states generated by four-wave mixing in an optical cavity", *Phys. Rev. Lett.* **55**, 2409 (1985).

[9] C. McCormick, V. Boyer, E. Arimondo, et al., "Strong relative intensity squeezing by four-wave mixing in rubidium vapor", *Opt. Lett.* **32**, 178–180 (2007).

[10] R. M. Shelby, M. D. Levenson, S. H. Perlmutter, et al., "Broad-band parametric deamplification of quantum noise in an optical fiber", *Phys. Rev. Lett.* **57**, 691 (1986).

[11] M. Fiorentino, J. E. Sharping, P. Kumar, et al., "Soliton squeezing in microstructure fiber", *Opt. Lett.* **27**, 649–651 (2002).

[12] S. Machida, Y. Yamamoto, and Y. Itaya, "Observation of amplitude squeezing in a constant-current–driven semiconductor laser", *Phys. Rev. Lett.* **58**, 1000 (1987).

[13] M. e. Tse, H. Yu, N. Kijbunchoo, et al., "Quantum-enhanced advanced ligo detectors in the era of gravitational-wave astronomy", *Phys. Rev. Lett.* **123**, 231107 (2019).

[14] D. S. Schlegel, F. Minganti, and V. Savona, "Quantum error correction using squeezed schrödinger cat states", *Phys. Rev. A* **106**, 022431 (2022).

[15] C. Xu, L. Zhang, S. Huang, et al., "Sensing and tracking enhanced by quantum squeezing", *Photonics Res.* **7**, A14–A26 (2019).

[16] M. A. Taylor, J. Janousek, V. Daria, et al., "Subdiffraction-limited quantum imaging within a living cell", *Phys. Rev. X* **4**, 011017 (2014).

[17] D. J. Griffiths, *Introduction to electrodynamics*, 2005.

[18] Z. J. Simmons, "Progress toward a negative refractive index in an atomic system: spectroscopy and simulations of a rare-earth doped crystal", PhD thesis (The University of Wisconsin-Madison, 2015).

[19] M. Fleischhauer, A. Imamoglu, and J. P. Marangos, "Electromagnetically induced transparency: optics in coherent media", *Rev. Mod. Phys.* **77**, 633 (2005).

[20] D. Yavuz, "Refractive index enhancement in a far-off resonant atomic system", *Phys. Rev. Lett.* **95**, 223601 (2005).

[21] J. Li, C. Zhu, and Y. Yang, "Squeezed light generated with hyperradiance without nonlinearity", *Opt. Lett.* **47**, 3439–3442 (2022).

[22] D. Yavuz and N. Proite, "Noise in refractive index enhancement", *Phy. Rev. A* **78**, 053811 (2008).

[23] S. Weinberg, "The cosmological constant problem", *Rev. Mod. Phys.* **61**, 1 (1989).

[24] B. Ryden, *Introduction to Cosmology* (Cambridge University Press, 2017).

[25] E. Di Valentino and A. Melchiorri, "Neutrino mass bounds in the era of tension cosmology", *Astrophys. J. Lett.* **931**, L18 (2022).

[26] M. Steidl, "Experiments for the absolute neutrino mass measurement", *arXiv preprint arXiv:0906.0454* (2009).

[27] G. G. Raffelt, "Dark matter: motivation, candidates and searches", *arXiv preprint hep-ph/9712538* (1997).

[28] T. Blaineau, M. Moniez, C. Afonso, et al., "New limits from microlensing on galactic black holes in the mass range $10M_\odot < M < 1000M_\odot$", *Astron. Astrophys.* **664**, A106 (2022).

[29] C. Flynn, A. Gould, and J. N. Bahcall, "Hubble deep field constraint on baryonic dark matter", *Astrophys. J.* **466**, L55 (1996).

[30] L. Bergström, "Dark matter candidates", *New J. Phys.* **11**, 105006 (2009).

[31] Y.-Z. Fan, T.-P. Tang, Y.-L. S. Tsai, et al., "Inert Higgs dark matter for CDF II W-boson mass and detection prospects", *Phys. Rev. Lett.* **129**, 091802 (2022).

[32] G. Rybka, "Axions and other similar particles",

[33] J. Pendlebury, S. Afach, N. J. Ayres, et al., "Revised experimental upper limit on the electric dipole moment of the neutron", *Phys. Rev. D* **92**, 092003 (2015).

[34] R. D. Peccei and H. R. Quinn, "Cp conservation in the presence of pseudoparticles", *Phys. Rev. Lett.* **38**, 1440 (1977).

[35] P. W. Graham, I. G. Irastorza, S. K. Lamoreaux, et al., "Experimental searches for the axion and axion-like particles", *Annu. Rev. Nucl. Sci* **65**, 485–514 (2015).

[36] G. Rybka, A. collaboration, et al., "Direct detection searches for axion dark matter", *Phys. Dark Universe.* **4**, 14–16 (2014).

[37] P. Sikivie, "Experimental tests of the "invisible" axion", *Phys. Rev. Lett.* **51**, 1415 (1983).

[38] D. Heuchel, A. Lindner, and I. Oceano, "The DESY axion search program", *arXiv preprint arXiv:2302.11934* (2023).

[39] S. J. Asztalos, R. Bradley, L. Duffy, et al., "An improved RF cavity search for halo axions", *Phys. Rev. D* **69**, 011101 (2004).

[40] C. Bartram, T. Braine, E. Burns, et al., "Search for invisible axion dark matter in the 3.3–4.2 μev mass range", *Phys. Rev. Lett.* **127**, 261803 (2021).

[41] J. Sloan, M. Hotz, C. Boutan, et al., "Limits on axion–photon coupling or on local axion density: dependence on models of the milky way's dark halo", *Phys. Dark Universe.* **14**, 95–102 (2016).

[42] C. Gao, W. Halperin, Y. Kahn, et al., "Axion wind detection with the homogeneous precession domain of superfluid helium-3", *Phys. Rev. Lett.* **129**, 211801 (2022).

[43] T. Wu, J. W. Blanchard, G. P. Centers, et al., "Search for axionlike dark matter with a liquid-state nuclear spin comagnetometer", *Phys. Rev. Lett.* **122**, 191302 (2019).

[44] A. Garcon, J. W. Blanchard, G. P. Centers, et al., "Constraints on bosonic dark matter from ultralow-field nuclear magnetic resonance", *Sci. Adv.* **5**, eaax4539 (2019).

[45] J. Berger, D. Brailsford, K. Choi, et al., "Snowmass 2021 white paper: cosmogenic dark matter and exotic particle searches in neutrino experiments", *arXiv preprint arXiv:2207.02882* (2022).

[46] Y. K. Semertzidis and S. Youn, "Axion dark matter: how to see it?", *Sci. Adv.* **8**, eabm9928 (2022).

[47] M. Kuster, H. Bräuninger, S. Cebrián, et al., "The x-ray telescope of cast", *New J. Phys.* **9**, 169 (2007).

[48] S. Andriamonje, S. Aune, D. Autiero, et al., "An improved limit on the axion–photon coupling from the cast experiment", *J. Cosmol. Astropart.* **2007**, 010 (2007).

[49] E. Arik, S. Aune, D. Autiero, et al., "Probing ev-scale axions with cast", *J. Cosmol. Astropart.* **2009**, 008 (2009).

[50] R. Ballou, G. Deferne, L. Duvillaret, et al., "Latest results of the osqar photon regeneration experiment for axion-like particle search", *arXiv preprint arXiv:1410.2566* (2014).

[51] K. Ehret, M. Frede, S. Ghazaryan, et al., "New ALPS results on hidden-sector lightweights", *Phys. Lett. B* **689**, 149–155 (2010).

[52] R. Ballou, G. Deferne, M. Finger Jr, et al., "New exclusion limits on scalar and pseudoscalar axionlike particles from light shining through a wall", *Phys. Rev. D* **92**, 092002 (2015).

[53] E. Armengaud, D. Attié, S. Basso, et al., "Physics potential of the international axion observatory (IAXO)", *J. Cosmol. Astropart.* **2019**, 047 (2019).

[54] H. Tam and Q. Yang, "Production and detection of axion-like particles by interferometry", *Phys. Lett. B* **716**, 435–440 (2012).

[55] J. Mendonça, J. Rodrigues, and H. Terças, "Axion production in unstable magnetized plasmas", *Phys. Rev. D* **101**, 051701 (2020).

[56] M. Gasperini, "Axion production by electromagnetic fields", *Phys. Rev. Lett.* **59**, 396 (1987).

[57] R. W. Boyd, *Nonlinear optics* (Academic press, 2020).

[58] D. J. Richardson, J. Nilsson, and W. A. Clarkson, "High power fiber lasers: current status and future perspectives", *JOSA B* **27**, B63–B92 (2010).

[59] I. Liberal and N. Engheta, "Near-zero refractive index photonics", *Nat. Photonics.* **11**, 149–158 (2017).

[60] N. Kinsey, C. DeVault, A. Boltasseva, et al., "Near-zero-index materials for photonics", *Nat. Rev. Mater.* **4**, 742–760 (2019).

[61] J. Jeong, Y. Kim, S. Bae, et al., "Simulation of classical axion electrodynamics using comsol multiphysics", *J. Korean Phys. Soc.*, 1–7 (2023).